Electrically-Assisted Friction Stir Welding of Aluminum Alloy to Advanced High Strength Steel

by

Xun Liu

A dissertation submitted in partial fulfillment
of the requirements for the degree of
Doctor of Philosophy
(Mechanical Engineering)
in the University of Michigan
2016

Doctoral Committee:

Professor Jun Ni, Chair
Professor Elijah Kannatey-Asibu Jr.
Professor Alan Taub
Professor Michael Thouless

ACKNOWLEDGEMENTS

I would like to express my foremost and most sincere gratitude to my advisor, Professor Jun Ni, for his invaluable guidance, support and encouragement throughout my graduate study. This work would never have been accomplished without him. I also deeply appreciate the precious time that Professor Elijah Kannatey-Asibu, Professor Michael Thouless and Professor Alan Taub have devoted serving on my dissertation committee.

Special thanks to Dr. Shuhuai Lan and Mr. Xianli Qiao for their advice and assistance on the difficulties I encountered during experiments. I would also like to thank Mr. Marv Cressey for his help and support at the machine shop at Autolab where I made all the parts for experimental setup. Many thanks to Dr. Zhili Feng for offering me the precious opportunity to work at the Oak Ridge National Lab and opening my eyes on current research in the field of welding.

Special thanks to Dr. Xiaoning Jin and Dr. Hao Yu for their warm help and care like big sister and brother when I first arrived in the United States. Many thanks to Mr. Charles Bodette, whose blue bus I have ridden almost each night during Fall and Winter semesters. I greatly appreciate the help from Professor Jingjing Li and Dr. Jinjin Ma for their advice on my life choices. I would also like to thank Weimin Wang, who gives me a lot of advice on physical exercise and helps me keep fit. I am grateful to Gaoqiang Chen and Weiyu Cao for their help on the FLUENT program. Thanks to my friends in S. M. Wu Manufacturing Research Center: Dr. Bruce Thai, Xi

Gu, Kai Chen, Yihao Zheng, Hao Lei, Huanyi Shui, Yangbing Lou, Xin Weng, Kevin Wilt and Baoyang Jiang.

Finally I would like to dedicate this work to my parents and especially my father. They are always there supporting me, giving me the confidence to face challenges as well as providing me advices for fighting through difficulties in life and works over the years.

TABLE OF CONTENTS

LIST OF TABLES

LIST OF FIGURES

ABSTRACT

Growing concerns about energy consumption increase the demand for lightweight vehicles. One of the most efficient solutions is to use multi-material structures. As a solid-state process, friction stir welding (FSW) is promising for joining dissimilar materials, such as aluminum alloy to steel. However, the processing window for achieving successful joints between these two materials is still narrow. Besides, a large axial welding force is required when steel is involved in the stirring nugget. In order to address these challenges, a material softening phenomenon, electro-plastic effect (EPE) is proposed to be incorporated into the process. With a high density electrical current applied during the traditional FSW, steel will be softened and reach a better compatibility with aluminum, which can enhance joint quality and reduce welding force.

In this research, first, the literature of EPE on various materials is systematically reviewed and a hypothesis is proposed for understanding the principles and mechanisms of the softening effect from electrical current. The effectiveness of EPE is then evaluated on one type of advanced high strength steel, TRIP 780/800 steel. High-density electrical pulses are applied during tensile tests. The effect of inevitable Joule heating is compared with EPE by applying pulses with higher current density but shorter duration, which generates about the same temperature increase. By measuring the volume fraction of the retained austenite after tensile tests, the applied current is shown to retard the martensitic transformation of TRIP steel.

Second, friction stir welding of Al 6061 to TRIP steel is comprehensively studied, which provides insights into this dissimilar material welding process and also experimental data for validation of the following developed thermo-mechanical models. Experiments are performed at various welding conditions, including different tool-rotation speeds, welding speeds and the relative tool position with respect to the two materials. The effects of process parameters on the joint microstructure evolution are analyzed based on the mechanical welding force and the temperature measured during the welding process. Intermetallic compound (IMC) layer of FeAl or Fe_3Al with thickness of less than 1 μm is formed at the Al–Fe interface in the advancing side. Three failure modes are identified during tensile tests. The maximum joint strength can reach 85% of the base aluminum alloy.

Third, in addition to the experimental study, analytical and numerical models are developed for friction stir welding of dissimilar materials. The transient plunge stage and the stable welding stage are studied separately. For the plunge stage, a field variable α is introduced to identify regions of steel and aluminum, and to define the generalized material properties. Conservation equations are developed at the interface between the two materials to account for the discontinuities. Numerical implementations are performed in the FEA software ABAQUS/Explicit. The stable welding stage is modeled based on Eulerian formulation with multiple phase flow theories. Velocity, pressure and temperature fields are shared among the two materials and material properties are averaged based on their volume fractions. The corresponding numerical analysis is performed in the CFD software FLUENT from ANSYS.

Finally, a hybrid electrically assisted FSW process is studied by applying high-density electrical currents to the FSW process. The corresponding experimental system is designed and developed. The plunge stage of FSW is studied on aluminum alloy Al 6061 and TRIP 780 steel

respectively. An effective reduction of the axial welding force can be obtained with good repeatability. The associated Joule heating is considered from an additional preheating test, which indicates that besides thermal softening, approximately 2/3 of the force reduction comes from direct electrical softening. During the hybrid FSW process for joining Al 6061 to TRIP steel, the axial welding force can also be consistently reduced under various welding conditions, which is a synergic result of both electro-plastic effect and Joule heating. Regarding the joint microstructure, the electrical current can enhance the formation of thin IMC layer and micro-interlock structures at the Al-Fe interface.

CHAPTER 1

INTRODUCTION

1.1 Background and motivation

Growing concerns about energy saving and environmental preservation increase the demand for lightweight vehicles. Considerable volumes of advanced high-strength steel (AHSS) sheets have been used for automotive parts, which meet the objective of both weight reduction and crashworthiness enhancement. AHSS, including Dual Phase (DP) steel, Transformation Induced Plasticity (TRIP) steel, Complex Phase (CP) steel and Martensitic steel (MART), has prominent mechanical properties of high strength and work hardening rate, which are obtained through their multiple phase microstructure [1]. However, further weight reductions of 30% or more are not achievable with exclusive dependence on the use of thinner steel sheets. Multi-material vehicle structures are an effective alternative [2], which necessitates the development of a reliable, efficient and economical technique for joining dissimilar materials. One of the typical desirable pairs is aluminum alloy and advanced high strength steel, which are highly difficult to weld together due to their great differences in physical and mechanical properties [3]. Moreover, the large amount of brittle intermetallic compounds (IMC) formed during traditional fusion welding

process will severely deteriorate the joint quality and initiate a fast rupture under applied stress [4-8].

Friction stir welding (FSW), which was first developed by The Welding Institute (TWI) in 1991 [9], shows its superiority as a solid-state process compared with traditional fusion welding. FSW consists of plunge, dwell and welding stages [10]. Plunge stage is the initiating phase of the whole process where the rotating FSW tool is gradually submerged into the workpiece until reaching the target depth. During the following dwell stage, the tool is then held rotating at this position to soften and preheat the workpiece. The final welding stage is where the tool translates along the weldline and finishes the whole joint. Not only can FSW significantly avoid solidification related problems, such as oxidization, shrinkage, porosity, and hydrogen solubility [11], but also its associated lower temperature can effectively inhibit intermetallic compound (IMC) layer formation, which makes it a promising solution for dissimilar material joining. However, since the materials are subjected to severe plastic deformations under a high strain rate, large welding force in both axial and welding directions is consequently involved, especially during plunge stage. This leads to significant tool wear issues and raises the demand of refractory tool materials for welding high melting temperature materials [12-14]. Furthermore, a high stiffness machine equipped with strong clamping fixtures is generally required.

Several studies have been carried out for FSW of aluminum alloys to mild steels [15-23] and demonstrated FSW as a promising solution for achieving reliable joints between these two materials. However, the processing window for achieving successful dissimilar material joints was still small. Besides, these works primarily focused on joint property evaluation and microstructure analysis, particularly at the Al-Fe interface. Few analytical or numerical models were developed

for the dissimilar material FSW process, which took into consideration the two materials in the weld nugget.

Electro-Plastic Effect (EPE) is the material softening phenomenon induced by high density electrical current during plastic deformation. It was reported that beyond the inevitable electrical resistance heating, moving electrons themselves could dynamically reduce the material deformation resistance without substantial temperature increase [24]. The electrical current was provided either continuously [25-30] or in the form of high-density pulses [31-35]. Previous literatures indicated that the electrical current could facilitate dislocation motion [36] and influence dynamic recrystallization [37], phase transformation [25, 38-40] as well as the kinetics of intermetallic compound formation and growth [41]. It can be observed that all of these phenomena are involved in the dissimilar FSW process. Moreover, the interfacial layer is crucial for the quality of dissimilar material joints. It is therefore expected that the application of electrical current can help improve traditional FSW process in the aspects of both reducing welding force and enhancing joint quality.

In this study, first the effectiveness of EPE will be verified on one type of advanced high strength steel, TRIP 780/800 steel. A comprehensive study on traditional FSW of dissimilar Al 6061 to TRIP steel will be then performed through both experimental and model analysis. Finally, the high density electrical current will be incorporated into FSW process for the potential benefits of welding force reduction and joint quality enhancement.

1.2 Research objectives

This research aims to provide a fundamental understanding of FSW for dissimilar aluminum alloy to TRIP steel and improve the process through electro-plastic effect. The specific objectives are summarized as the following:

(1) Understanding softening mechanisms of electro-plastic effect (EPE): Literature on EPE will be systematically reviewed. An electrically assisted tensile testbed will be developed for the measurement of mechanical behavior of TRIP steel under different pulse conditions. Stress strain relationship under the effect of electrical current will be modeled. Microstructure analysis, including both optical microscopy and X-Ray Diffraction (XRD), will be carried out for further insight of the electro-plastic effect on TRIP steel.

(2) Experimental study of friction stir welding of dissimilar Al 6061 to TRIP steel: Friction stir welding experimental system will be developed based on a CNC machine, which can measure welding force and temperature during the process. Various welding conditions will be investigated, including different tool rotating speeds, weld speeds and relative tool position with respect to the two materials. Macrostructure and microstructure analysis will be performed on the cross sections of weld specimens and particularly at the Al-Fe joint interface. Joint quality will be evaluated with mechanical tensile tests. Relationships between process parameters, joint microstructure and joint strength will be established.

(3) Theoretical and numerical modelling of the dissimilar material FSW process: The transient plunge stage and steady state welding stage will be modeled separately. Based on multiple phase flow theories, analytical formulations will be developed considering two material properties in the weld nugget, which will be further implemented into corresponding Finite Element Analysis software for solutions. The models will be validated through comparison with the experimental results regarding welding force, temperature and material distribution, which helps provide a further understanding of the process and future optimization of process parameters.

(4) Investigation of the electrically assisted FSW process: An electrically assisted FSW system will be designed and implemented, which can maintain a high electrical current density in the weld nugget surrounding the moving FSW tool. The optimal configuration of electrodes will be determined based on numerically analyzed electrical current distribution. Effects of electrical current will be investigated first on the plunge stage for the two materials, Al 6061 and TRIP steel, separately. The influence of Joule heating will be assessed based on preheating tests. Finally, the electrical current will be applied for the entire dissimilar material FSW process. Welding force and temperature will be compared between traditional and the electrically assisted conditions. Microstructure analysis on the Al-Fe joint interface will also be performed to evaluate the electrical effects on joint quality.

If reliable joints of dissimilar materials can be obtained through this hybrid electrically assisted FSW process, future improvements of automobile structures with optimal material combinations will be possible. Prospective benefits will cover broad fields of aerospace, automobile, marine engineering and so on.

1.3 Thesis outline

The rest of this dissertation is organized as follows.

In Chapter 2, the literature of electro-plastic effect is systematically reviewed and a hypothesis is proposed for understanding the underlying mechanisms of this phenomenon. Its effectiveness is then verified on one type of advanced high strength steel, TRIP steel, by applying pulses with different current densities and durations. Microstructure analysis is performed to understand involved phase transformation process. This chapter is based on paper “Experimental

Study of Electro-Plastic Effect on Advanced High Strength Steels", by X. Liu, S. Lan and J. Ni, published in *Materials Science and Engineering: A*.

In Chapter 3, friction stir welding of aluminum alloy to advance high strength steel is experimentally studied. Effects of various welding parameters, including tool rotating speed, welding speed and tool position on welding force and temperature are investigated, which are further related to the microstructure evolution and joint quality. This chapter is based on paper "Analysis of Process Parameters Effects on Friction Stir Welding of Dissimilar Aluminum Alloy to Advanced High Strength Steel", by X. Liu, S. Lan and J. Ni, published in *Materials & Design*; paper "Experimental Investigation on Joining Dissimilar Aluminum Alloy 6061 to TRIP 780/800 Steel through Friction Stir Welding", by X. Liu, S. Lan and J. Ni, published in *ASME Journal of Engineering Materials and Technology*.

In Chapter 4, theoretical and numerical models of the dissimilar material friction stir welding process are developed based on multiple phase flow theories. Plunge and welding stages are considered separately. This chapter is based on paper "Thermal Mechanical Modelling of the Plunge Stage during Friction Stir Welding of Dissimilar Al 6061 to TRIP 780 Steel" by X. Liu, S. Lan and J. Ni, published in *ASME Journal of Manufacturing Science and Engineering*; paper "Thermomechanical Modeling on Friction Stir Welding of Aluminum Alloy 6061 to TRIP Steel" by X. Liu, G. Chen, Z. Feng and J. Ni, submitted to *International Journal of Machine Tools and Manufacture*.

In Chapter 5, the electrically assisted friction stir welding process is studied. The experimental system is designed and developed. Welding force, temperature and joint microstructure are compared between traditional friction stir welding process and electrically assisted conditions. This chapter is based on paper "Electrically assisted friction stir welding for

joining Al 6061 to TRIP 780 steel" by X. Liu, S. Lan and J. Ni, published in *Journal of Materials Processing Technology.*

In Chapter 6, the contributions of this dissertation are summarized and possible future works are proposed.

CHAPTER 2

ELECTRO-PLASTIC EFFECT ON TRIP 780 ADVANCED HIGH STRENGTH STEEL

2.1 Literature review

Electro-Plastic Effect (EPE) is a material softening phenomenon induced by high density electrical current during plastic deformation. It was first discovered by Troitskii and Likhtman [42] in 1963 when they used 1MeV electrons to irradiate the Zn crystals and reported a reduced flow stress, which was beyond the resistance heating effect. Earlier studies of this phenomenon were conducted mainly by the Troitskii research group and Conrad research group. In their works, various types of pure metal were treated with excessively high density current pulses (in the order of 10^3 A/mm^2) of ultra-short pulse duration (in the order of 10^{-4} s [31, 32]). Plastic flow stress dropped immediately as the pulse was applied but returned quickly to the original stress stain profile after stopping the current. Metals investigated included Nb, Al, Cu, Fe, Pb, Sn, Ti and so on [33-36]. Higher current density reduced deformation resistance to a larger extent. Recent studies from Roth research group and Tang research group concentrated more on metal alloys, including Mg alloys [25], Ti alloys [26], Al alloys [43], Cu alloys [28, 29] and steels [44]. Besides, the

electrical power source was switched to longer pulses or continuous form but with small current magnitude. Similar to the results under high density current pulses, work softening phenomenon occurred for these alloys when current density reached a threshold value. Furthermore, an appropriate series of pulses helped improve ductility. Xu et al. [37] showed the elongation of AZ31 Mg alloy at a high strain rate was increased through electrical pulsing treatment and attributed the cause to be the electrically assisted dynamic recrystallization. Salandro et al. [45] showed a similar result on the improvement of ductility for Al alloy 5052 and 5083 and one typical stress strain curve is shown in Figure 2-1.

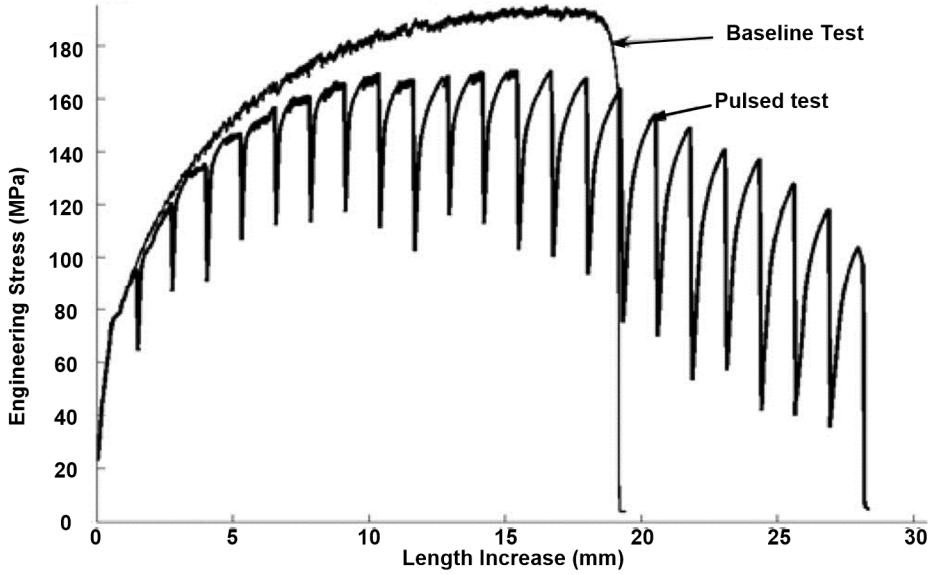

Figure 2-1 Stress strain curve for Al5052 with electrical pulsing treatment (Copied from Salandro et al., 2010, Journal of Manufacturing Science and Engineering, Vol. 132, pp. 051016. [45])

Several theories have been proposed to interpret the underlying mechanism of this Electro-Plastic Effect. Regarding pure metals, since their plastic deformation is basically involved with movement, entanglement and multiplication of dislocations, the effectiveness of EPE was due to the contribution of electron facilitated dislocation motion [32, 46]. According to this theory, momentum of the moving electrons can be transferred to dislocations, which accelerated their movement and modified their arrangement. Explanation of EPE on alloys was more sophisticated.

Kuang et al. [47] compared electro-plastic rolling with warm rolling for AZ31 Mg alloy and showed the electrical current results in a more frequent twinning behavior in certain directions. Apart from effects on dislocations, electrically induced recrystallization and phase transformation [41] both contributed to the reduction of deformation resistance. Conrad et al. [48] showed the electrical current could reduce the temperature and increase the rate of recovery and recrystallization for Cu and Al. Xu et al. [49] did electro-plastic rolling of AZ31 Mg alloy and also observed dynamic recrystallization at a relatively low temperature. Similar phenomenon was again reported for pure α-Ti [50] and aluminum alloy Al 7475 [51].

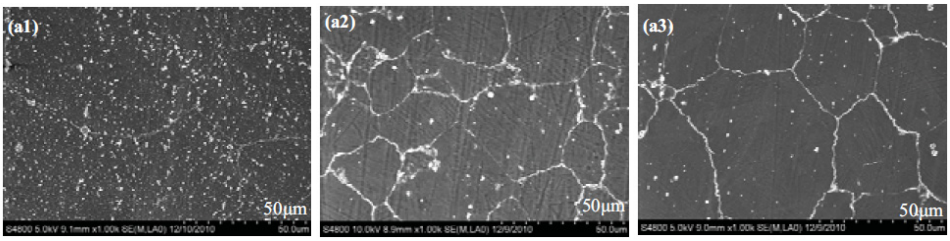

Figure 2-2 Dissolution of *β* precipitate in AZ91 Mg alloy under electrical pulse treatment with different frequencies: (a1)Non-EPT; (a2) 204 Hz-EPT; (a3) 309 Hz-EPT (Copied from Zhang et al., 2012, Journal of Surface Engineered Materials and Advanced Technology, Vol. 2, pp. 16-21. [25])

Zhang et al. [25, 40] reported that with electrical pulse treatment, the dissolution of *β* precipitate in AZ91 Mg alloy was achieved at a lower temperature and much faster rate, as shown in Figure 2-2. It was interpreted that the electrical current provided an additional Gibbs free energy term, which resulted the reversed thermodynamic phenomenon. A similar reverse phase transformation was also observed in a Zn-Al alloy by Zhu et al. [38]. In order to model and predict the electro-plastic effect, Bunget et al. [52-54] introduced a characteristic parameter called Electroplastic Effect Coefficient (EEC) from the aspect of energy. The EEC was defined as the ratio of the amount of the applied electrical power towards plastic deformation over that towards resistive heating, which quantified the efficiency of electrically assisted manufacturing processes.

2.2 Further discussion on electro-plastic effect

The electro-plastic effect is still a controversial topic in research communities, which is primarily due to the resistance heating that inevitably occurs with the passage of current. In this study, a hypothesis for mechanisms of electro-plastic effect on metals is tentatively proposed as the followings:

The high density electrical current can heat up local strengthening sites due to their high electrical resistance, which promotes dislocations to bypass these obstacles without temperature increase of the bulk material.

Plastic deformation for metals is based on the movement of dislocations. Strengthening is essentially to add obstacles to materials to inhibit this motion. There are primarily four types of strengthening mechanisms:

(1) Work hardening: Interference between dislocations make themselves to be obstacles for the motion of each other. During plastic deformation, multiplication of dislocations will aggravate this effect and generate dense tangles, subboundaries and cell boundaries, which further strengthen the material.

(2) Boundary hardening: Typical boundaries include grain boundaries and phase boundaries. Grain boundary separates grains with different crystallographic orientations, which therefore is a highly disordered region and impenetrable to dislocations. Similarly, phase boundaries separate different phases and the local discontinuities will also impede dislocation motion.

(3) Solution hardening: For either substitutional or interstitial solute atoms, they will generally distort the solvent lattice and result in a local stress field. This will interact with the stress field associated with dislocations and therefore restrict their movement.

(4) Precipitation hardening: Precipitates are basically second phase particles in the size of nanometer scales. Coherent precipitates strengthen the material in a similar way to that as solution hardening. As the precipitate size increases, mismatch coherency strain energy increases and leads to more strengthening effects. Incoherent precipitates have a mismatch interface with the base material. Dislocations need to either cut through or bow around them during plastic deformation.

All the above strengthening mechanisms are from disturbances in crystal structure. At these sites, the probability for moving electrons to collide with the lattice atoms is much higher than that to linearly pass through and conduct electrical current. Collision will transfer the kinetic energy of electrons into vibrational energy of atoms. These are manifested as larger local resistance and therefore higher temperature increase. As the plastic deformation occurs, the highly vibrated atoms directly assist dislocation to bypass these local strengthening obstacles. On the other hand, the bulk material region still remains at relatively low temperature due to their lower electrical resistance. For short pulses, the temperature difference between local strengthening sites and bulk material can be more significant since less amount of time is allowed for heat conduction to homogenize temperature field.

There are several evidences from literature that help support this hypothesis. Electro-plastic effect was hardly observable in the elastic range [55]. Since elastic deformation is related to stretching or compressing atomic bonds, local temperature increase at material strengthening sites can only expand limited number of atoms, which contributes to negligible amount of elastic strain and therefore little softening effect.

Regarding work hardening, study of EPE on pure titanium showed that the effect was more significant at later stage of plastic deformation [31]. Yao et al. [56] studied electrically assisted

wire-drawing for austenite stainless steel. Similarly, the decrement of drawing force was closely related to the accumulated drawing strain. Salandro et al. [57] compared the effect of electrical pulses on Al 5083 in the cold worked H32 condition and annealed condition. Reduction of flow stress was higher in the former one. Similar experiments were also performed on Al 2024 alloys with different heat treatments [58]. The T351 condition, which include solution plus cold work, showed higher stress drop than the T4 condition, which is only solution treatment with natural aging. A larger plastic strain or cold work condition is related to higher dislocation density in materials, these observed phenomena therefore indicate EPE is more effective with more dislocations.

Regarding boundary hardening, Siopis and Kinsey [59] studied EPE on pure copper and showed that finer grain size distribution required smaller threshold current density to initiate EPE. In addition, under the same current density, finer grains corresponded to higher reduction of flow stress. Fan et al. [60] did experiments on the 70/30 brass and reported similar results. More importantly, they directly observed melting of local grain boundaries for tensile specimens subjected to high electrical current. However, they did show that a higher temperature increase was also associated with refined grain distribution.

Regarding solution hardening, the drop of flow stress from EPE increases with greater amount of alloying. Based on Kiryanchev et al. [61], adding Cd element into Zn crystal structure increased the softening effect by tens of percent in the plastic range. For titanium, an increasing concentration of interstitial impurities similarly resulted in a larger flow stress drop with application of same amount of electrical current [34]. Dzialo et al. [29] also showed the phenomenon by increasing Zn content in Cu matrix.

Regarding precipitation hardening, Andrawes et al. [27] applied a continuous direct current on aluminum alloy Al 6061 with different aging conditions. The reduction of flow stress in the peak aged T6511condition was larger than the overaged conditions. Since precipitates coarsening occurs and the number of precipitates is reduced in the overaged condition, the EPE is more effective with finer distribution of precipitates.

In this chapter, Electro-Plastic Effect on one type of Advanced High Strength Steels (AHSS), TRIP 780/800 steels is investigated. Uniaxial tensile tests are carried out under different current densities and pulse durations. Stress strain relationship, ductility and microstructure are analyzed to identify the underlying mechanisms. X-Ray Diffraction method is employed to quantify the volume fraction of retained austenite near the fracture region and therefore determine the extent of phase transformation. Optical microscopic analysis is also performed for qualitative observation of phase and grain size distribution.

2.3 Experimental study of electro-plastic effect on TRIP steel

2.3.1 Electrically assisted tensile test setup

Uniaxial tensile tests were performed on a MTS 810 material testing system at a nominal strain rate of 5×10^{-3}/s. The electrical pulses were provided by Lincoln Electric Power Wave 455 source and the magnitude of the current was adjusted for different current densities. The current densities referred to here represent the initial current density prior to deformation. The cross-sectional area decreases as the uniaxial straining continues and therefore the actual current density increases during the process. The maximum difference between nominal and true current density was only about 8% before necking. The nominal current density was therefore employed for analyzing experimental results.

A detailed view of the experimental arrangement was shown in Figure 2-3. The electricity entered the lower copper electrodes, passed through the specimen and exited at the top copper electrodes. The copper electrodes and tensile specimen were electrically insulated from the grips of the tensile machine by mica sheets. The grips were hydraulically tightened to ensure close contact between the specimen and copper electrodes. Slots were milled onto the mica sheets to avoid potential sliding between the tensile specimen and mica sheets. In order to minimize temperature increase from Joule heating, forced air cooling was implemented during entire tests.

The tested material of TRIP 780/800 was provided by the United States Steel Corporation. Dog bone tensile specimens were prepared by waterjet machining. Surface temperature in the middle of the tensile specimen was measured by a type-K thermal couple, as shown in Figure 2-4. Test conditions and corresponding highest measured temperature are listed in Table 2-1.

Table 2-1 Process conditions for the electrically assisted tensile test

Experimental Conditions	**1**	**2**	**3**	**4**	**5**	**6**	**7**	**8**
Current density (A/mm^2)	0	7.4	11.4	15.3	15.3	22.2	25.7	29.7
Pulse duration (s)	0	4	4	4	1	1	1	1
Pulse period (s)	0	10	10	10	10	10	10	10
Highest temperature (°C)	24	28	36	61	30	41	56	61

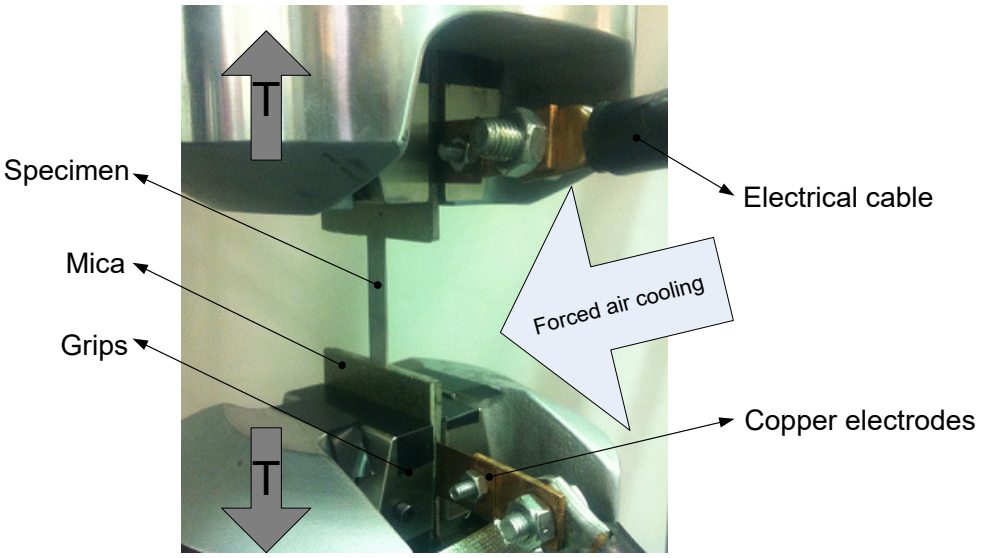

Figure 2-3 Experimental setup for the electrically assisted tensile test

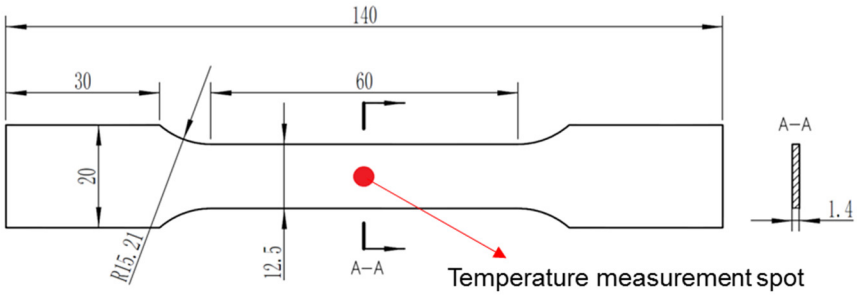

Figure 2-4 Dimensions of the tensile test specimen (unit: mm)

Joule heat from electrical current is generated inside the tensile specimen. Although forced air cooling can suppress temperature increase on the surface, the internal region of the specimen might still remain at a higher temperature. In order to verify the efficacy of forced air cooling, a multiphysical finite element model considering both resistance heating and heat transfer was developed in COMSOL software. The necessary material parameters are listed in Table 2-2. Since forced air cooling essentially changes the heat transfer conditions on surface boundaries, different heat transfer coefficients were substituted into the model until the calculated temperature matches the measured result. The heat transfer coefficient was then determined to be 50 W/(m^2 K). Figure 2-5 shows the temperature distribution on the cross sectional area denoted as A-A in Figure 2-4. The current density in (a) is 15.3A/mm^2 with the pulse duration of 4 seconds. The temperature difference is less than 0.5 ºC inside the workpiece. The current density in (b) is 29.7 A/mm^2 with the pulse duration of 1 second. Similarly, the temperature difference is less than 0.4 ºC. Accordingly, the temperature can be considered homogeneously distributed over the tensile specimen under forced air cooling.

Metallurgical samples were sectioned near the fracture surface using a slow speed diamond wafer blade with coolant applied in the meantime. The samples were mechanically ground with 320, 600 and 800 grit papers and subsequently polished with 3μm, 1μm diamond suspensions and

finally 0.03μm colloidal silica suspension. Very low force was applied during cutting, grinding and mechanical polishing to minimize additional stress induced transformation of retained austenite. The surfaces were then cleaned with soap solution, water and ethanol and dried immediately under forced air. XRD measurements were performed using the Rigaku Miniflex X-ray diffractometer with Cu-Kα radiation. The range of diffraction was selected from 40º to 85º with a scanning speed of 0.1º/step and a 10 seconds dwell time. The diffraction patterns were analyzed using the whole pattern fitting program of the MDI JADE software.

Table 2-2 Material properties for TRIP 780/800 (25 ºC)

Property	Name	Value	Unit
Heat capacity at constant temperature	C_p	500	J/(kg K)
Thermal conductivity	k	16.2	W/(m K)
Electrical conductivity	σ	$5.36x10^6$	S/m
Density	ρ	8027	Kg/m^3

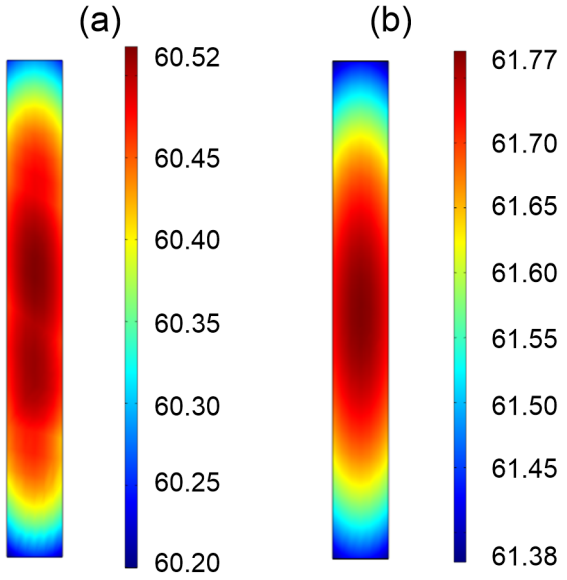

Figure 2-5 Temperature distribution on the specimen cross section based on FEA calculation (a) 15.3 A/mm² and 4s; (b) 29.7 A/mm² and 1s.

2.3.2 Mechanical behavior of TRIP steel under various pulse conditions

Figure 2-6 (a) shows the material tensile behavior under a current density of 15.3 A/mm² with pulse length of 4 seconds. A total of 4 pulses were applied during the deformation at true

strains of 0.049, 0.095, 0.140 and 0.182 respectively and the pulse location and length is marked in the figure. The applied pulses produced stress drops of approximately 70MPa, 95MPa, 115MPa and 90MPa respectively. The softening phenomenon is more effective at a larger strain except the final pulse. During the last pulse, necking occurred and small cracks were generated along the edge of the specimen, which could change the current distribution over the cross sectional area and result in an opposite trend. Similar to EPE results from literature, the flow stress dropped immediately when the current was applied and then returned back after the current was stopped. Work hardening resumed until the next pulse was applied and the plastical flow stress dropped again. Apart from the reduction of flow stress, the ultimate strain also increased under this pulse condition. In this work, the nominal stress/strain values are transformed into true stress/strain values using the following set of equations without separately considering the condition after necking:

$$\sigma_T = \sigma_n \left(1 + \varepsilon_n\right) \tag{2-1}$$

$$\varepsilon_T = \ln\left(1 + \varepsilon_n\right) \tag{2-2}$$

Figure 2-6 (b) shows the true stress-strain curves corresponding to 4 pulses applied at the same strains as in Figure 2-6 (a) but with higher current density of 29.7 A/mm^2 for 1 second. The reduction of flow stress was approximately 120MPa, 205MPa, 285MPa and 265MPa at each pulse, which is twice as large as those under the current density of 15.3 A/mm^2. Similarly, the stress drop was larger at higher strain except the last pulse due to necking. However, the improved ductility was not obvious in this case.

Temperature increase from electrical Joule heating will affect the measured stress strain curve from both aspects of thermal expansion and thermal softening. From the temperature measurement result, the highest temperatures on the workpiece under these two electrical

conditions were around the same value of 61 ºC. Assuming the stress drop in the condition of 15.3A/mm^2 results purely from thermal effects, the additional stress drop in the condition of 29.7 A/mm^2 should therefore come from direct electrical softening, which demonstrates the existence of electro-plastic effect on this TRIP steel.

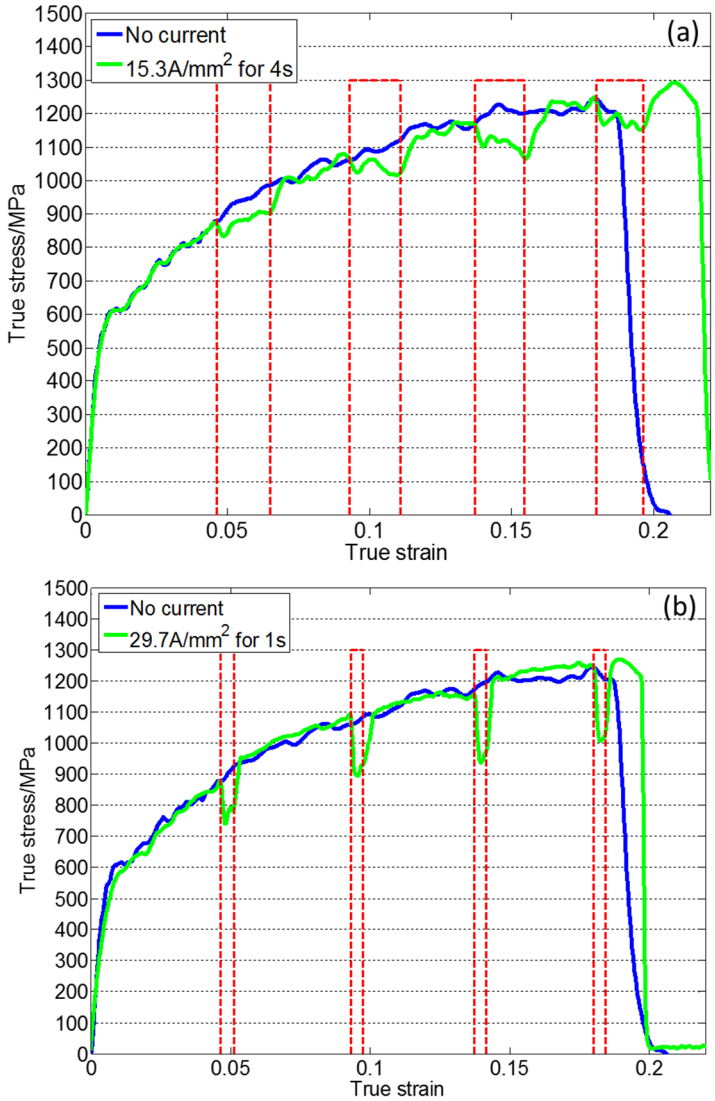

Figure 2-6 True stress and true strain curves under different test conditions: (a) 15.3 A/mm^2 with 4s (b) 29.7 A/mm^2 with 1s

To further consider the thermal effects, the stress drop associated with thermal expansion is calculated for each test condition based on the following equation:

$$\Delta\sigma_{th} = E \cdot \alpha \cdot \Delta T \tag{2-3}$$

where α is the thermal expansion coefficient and is set as 10 x 10^{-6} /ºC based on literature [62-64]. In each test condition, the total stress drop from electrical current, the stress drop from thermal expansion and the difference between these two are listed in Table 2-3. The stress drop is overall much more significant in the shorter pulse conditions.

Table 2-3 Stress reduction under each test condition

Experimental Conditions	**1**	**2**	**3**	**4**	**5**	**6**	**7**	**8**
Current density (A/mm^2)	0	7.4	11.4	15.3	15.3	22.2	25.7	29.7
Pulse duration (s)	0	4	4	4	1	1	1	1
Highest temperature (ºC)	24	28	36	61	30	41	56	61
Total Stress reduction from electrical current $\Delta\sigma$ (MPa)	N/A	10	31	93	40	102	178	218
Stress reduction due to thermal expansion $\Delta\sigma_{th}$ (MPa)	N/A	8	24	74	12	34	64	74
$\Delta\sigma - \Delta\sigma_{th}$ (MPa)	N/A	2	6	19	28	68	114	144

Since the highest temperature under all experimental conditions in this study is much smaller compared to the material melting point, the empirical power law constitutive model is adopted to describe the variation of flow stress:

$$\sigma = K\varepsilon^n \tag{2-4}$$

where σ is the true stress, K is the strength coefficient, ε is the true plastic strain and n is the strain hardening exponent which correlates with the strain hardening rate. Materials with a higher n value can gain more strength under the same strain. Coefficients of *K* and *n* were obtained by fitting curves to the experimental data points where electrical pulses were applied. The fitted curves are interpreted as the true stress obtained under the same pulse condition at different strains. Results are shown in Figure 2-7 and the fitted coefficients are shown in Figure 2-8, where the vertically aligned two points represent the conditions of same current density of 15.3 A/mm^2 but with

different pulse durations. Both the strength coefficient K and the strain hardening exponent n decrease as current density increases and the trend is more obvious at higher current density. In Figure 2-7, the curve under the current density of 7.4 A/mm^2 basically coincides with the original stress strain curve while a distinct stress drop occurs when the current density reaches 11.4 A/mm^2. This implies that the threshold current density to induce EPE for this TRIP steel is in between these two values. Another phenomenon is that under the same current density of 15.3 A/mm^2, different pulse durations result in almost overlapped stress-strain curves despite that the temperature is about 30 ºC higher under longer pulses.

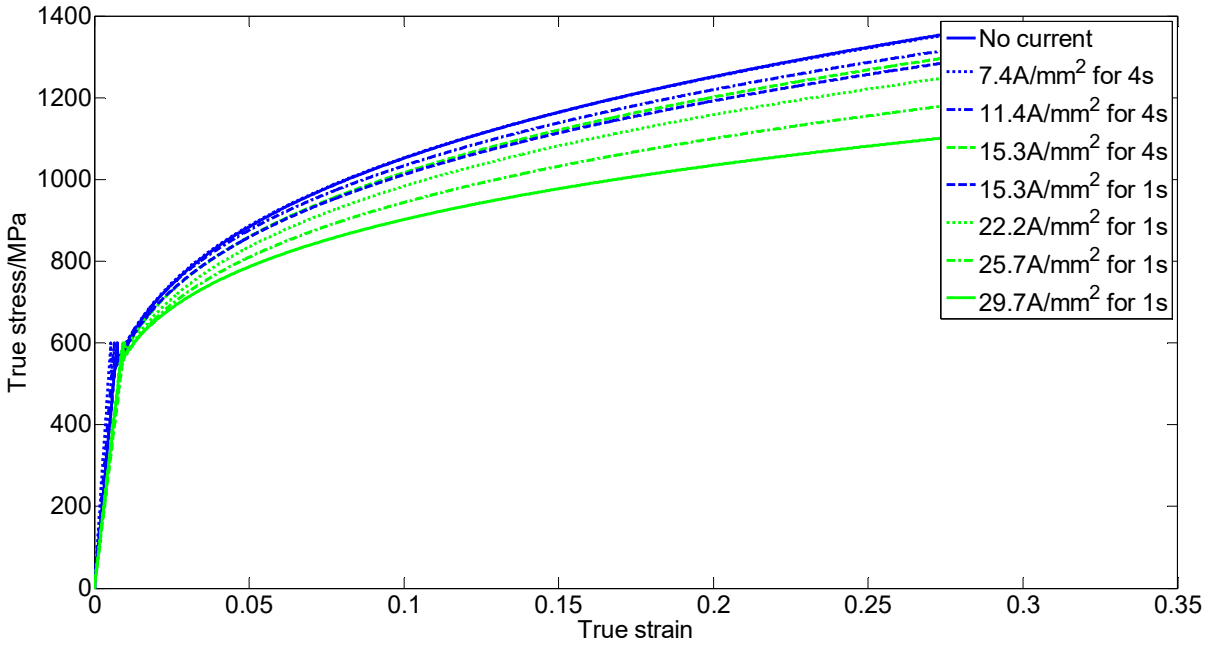

Figure 2-7 Power law constitutive model fitted from experimental results

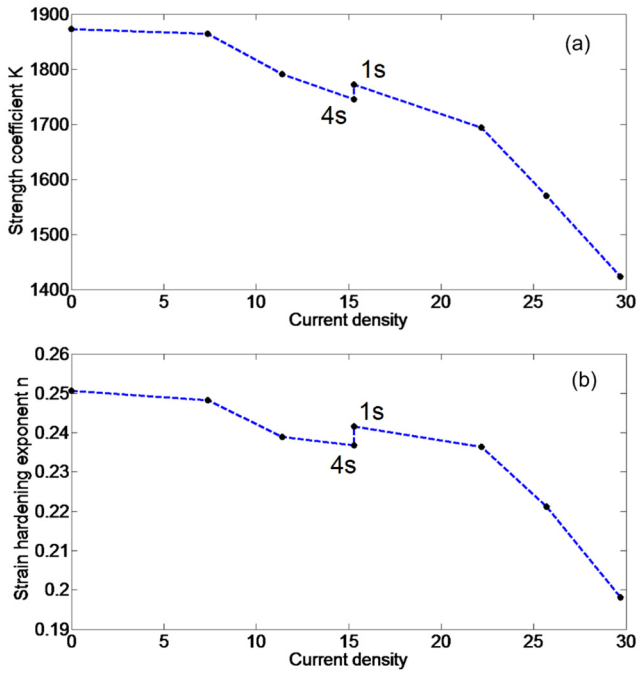

Figure 2-8 (a) Strength coefficient K as a function of current density; (b) Strain hardening exponent n as a function of current density

2.3.3 Microstructure analysis

The excellent mechanical properties of both enhanced strength and formability for TRIP steel arise from its multiple phase microstructure. TRIP steel typically consists of a ferritic matrix with the dispersion of bainite, retained austenite and possible small amount of martensite. Appropriate heat treatment including intercritical annealing and subsequent austempering enables retention of metastable austenite at room temperature [65]. During plastic deformation, strain induced phase transformation from retained austenite into martensite occurs [66], which enables a large work hardening rate and relatively higher ductility. Since the martensitic transformation is closely related to the mechanical behavior of TRIP steel, X-ray Diffraction (XRD) analysis is applied to quantitatively determine the volume fraction of retained austenite. The measured diffraction patterns of tensile specimens from different test conditions are shown in Figure 2-9. The peaks associated with austenite, especially the A-220 peak are distinguished when no

deformation occurs. Near the fractured surface from non-electrically assisted tensile condition, the A-220 peak is hardly visible. On the other hand, with the application of electrical current this austenite peak can be regained and higher current density can preserve the peak to a greater extent.

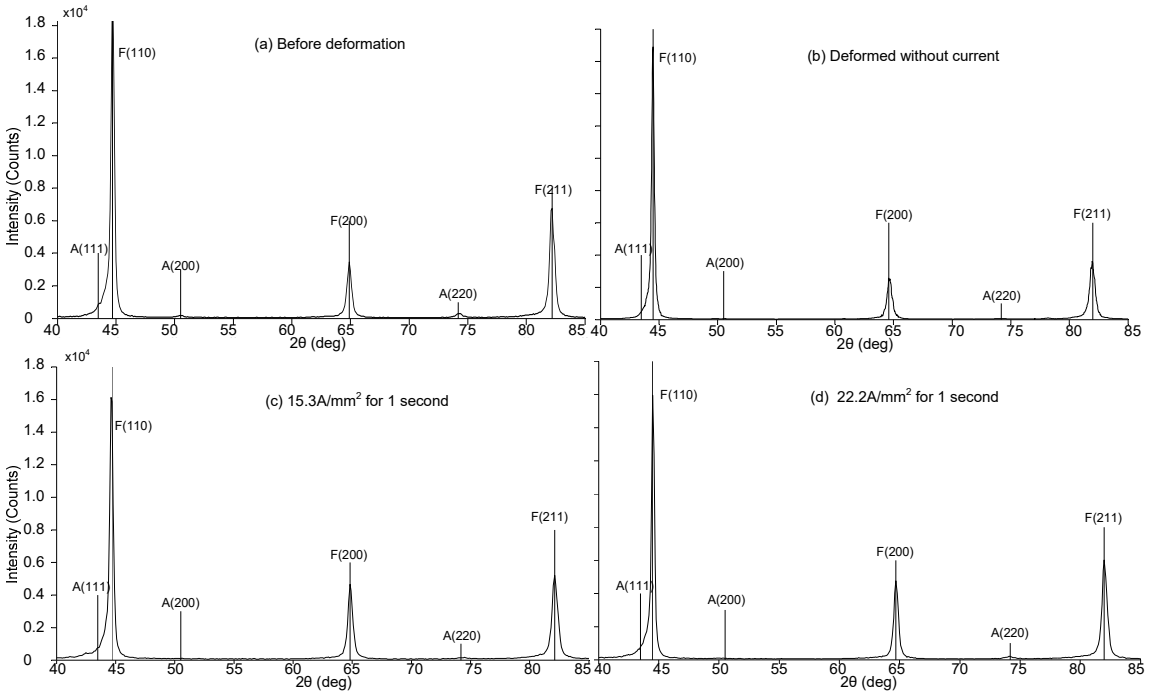

Figure 2-9 XRD diffraction patterns of the fractured specimen : (a) Original material; (b) Fractured region without current; (c) Fractured region with 15.3A/mm^2 for 1 second; (d) Fractured region with 22.2A/mm^2 for 1 second

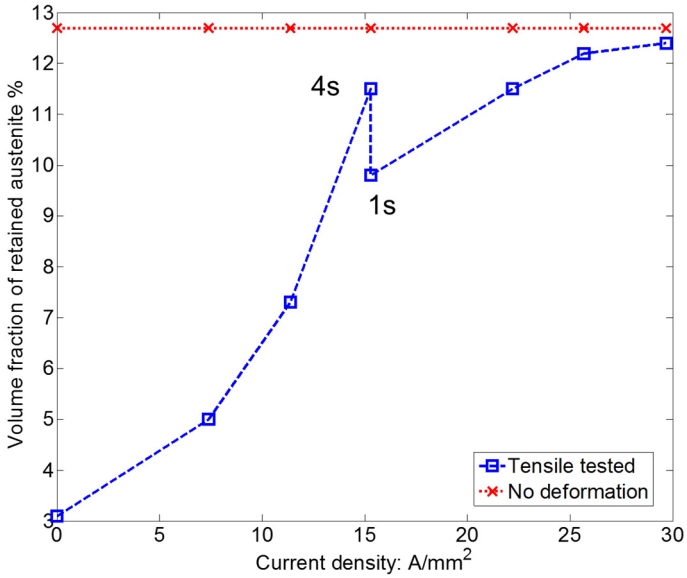

Figure 2-10 Volume fraction of retained austenite under different test conditions

In X-ray diffraction patterns, volume fractions of different phases are proportional to the integrated intensity of corresponding peaks. The volume fractions of retained austenite under different tensile test conditions are accordingly calculated and compared in Figure 2-10. In order to separate the effect of Joule heating on phase transformation, another series of specimens are treated with same pulse conditions without plastic deformation. The results on the volume fraction of retained austenite are also shown in Figure 2-10. Purely static resistance heating with the maximum temperature of 61 ºC has negligible effect on the kinetics of martensitic transformation. However, when the electrical pulses are applied simultaneously during plastic deformation, the volume fraction of retained austenite can be increased. Moreover, greater amount of austenite can be retained under a higher current density. The vertical line at the current density of 15.3 A/mm^2 showed that longer pulse duration retarded the martensitic transformation to a larger extent. With further increasing the current density, the extent of retarded transformation becomes saturated since the quantity of the retained austenite in fractured specimens approaches that of the original material. In other words, a high enough current density is possible to fully restrain martensitic transformation during plastic deformation of TRIP steel.

The suppressed martensitic transformation under electrical current can be considered from thermodynamic principles. Figure 2-11 [67] is a schematic illustration of the Gibbs free energies of austenite and martensite near the equilibrium temperature T_0 , where the Gibbs free energies for these two phases are equal. M_s is the martensite transformation start temperature, which corresponds to the minimum free energy driving force $\Delta G^{\gamma\rightarrow\alpha'}_{M_s}$. In the temperature range above M_s and below T_0 , martensite cannot form spontaneously due to insufficient driving force [68]. However, if an external mechanical force supplies additional energy *U'*, which satisfies

$$\Delta G_{T_1}^{\gamma\to\alpha'} + U' = \Delta G_{M_s}^{\gamma\to\alpha'} \tag{2-5}$$

martensitic transformation is then possible. As the temperature increases from M_s, higher mechanical force is required as a consequence of the reduced thermomechanical driving force. When the temperature reaches M_s^σ, the required mechanical force exceeds the yield strength of austenite matrix and plastic deformation occurs. Accordingly, the temperature region of $M_s \le T \le M_s^\sigma$ is called stress-assisted transformation regime while the region of $M_s^\sigma < T \le T_0$ is generally referred to as strain-assisted transformation regime [69]. During electrically assisted tensile tests, the reduced plastic flow stress accordingly reduced the external work provided by mechanical force, which helps justify the retarded martensitic transformation. In particular, under the same current density of 15.3 A/mm^2, longer pulses preserved larger amount of austenite since a longer strain range is associated with reduced flow stress, which results in less amount of input mechanical energy.

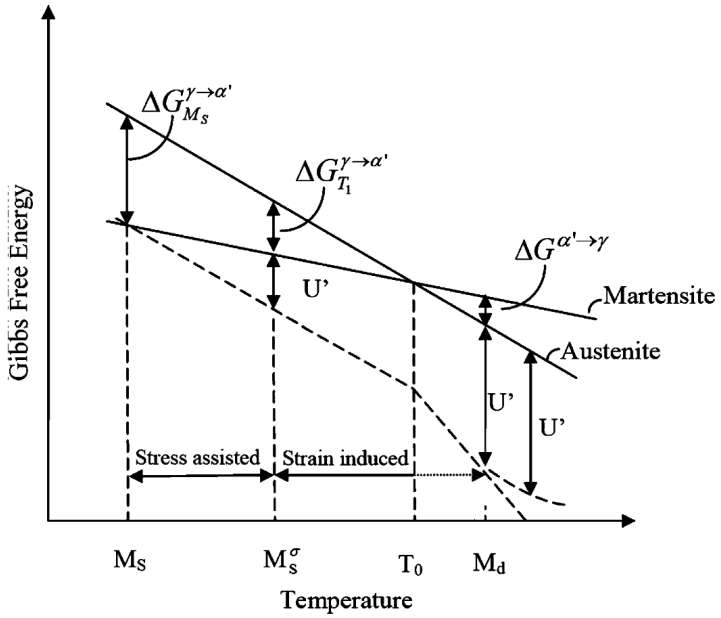

Figure 2-11 Gibbs free energy of martensite and austenite as a function of temperature (Copied from Curtze et al., 2009, Materials Science and Engineering: A, Vol. 507(1), pp. 124-131. [70])

2.4 Summaries and conclusions

In this chapter, first a hypothesis on the softening mechanisms of electro-plastic effect is proposed based on reported material behaviors from various literature. The high density electrical current can heat up local strengthening sites due to their intrinsic higher electrical resistance, which promotes dislocations to bypass these obstacles without temperature increase of the bulk material.

Second, electro-plastic effect has been experimentally investigated on one group of Advanced High Strength Steels (AHSS), TRIP steel. The applied current densities range from 7.4A/mm^2 to 29.7A/mm^2 with the pulse duration of 1 or 4 seconds. Increasing the current density from 15.3A/mm^2 to 29.7A/mm^2 and shortening the pulse length from 4s to 1s can generate a larger stress drop under approximately same temperature increase. This helps demonstrate the effectiveness of EPE on TRIP steel. Further microstructure analysis showed the electrical pulses can retard the martensitic phase transformation process involved in plastic deformation of TRIP steel.

CHAPTER 3

FRICTION STIR WELDING OF DISSIMILAR ALUMINUM ALLOY 6061 TO TRIP 780 ADVANCED HIGH STRENGTH STEEL

3.1 Literature review

Several studies were carried out on friction stir welding of aluminum alloy to steel sheets. Uzun et al. [15] reported the joint strength between Al 6013-T4 and 304 stainless steel with the thickness of 4mm reached approximately 70% of the base aluminum alloy. Ghosh et al. [16] did FSW of pure Al to 304 stainless steel and the maximum joint strength was 82% of Al. The presence of Fe_3Al was observed. Equiaxed and finer grains in the stirring zone indicated the involved dynamic recrystallization process. Tanaka et al. [18] welded Al 7075-T6 to mild steel with the thickness of 3 mm. Tool rotational speed varied from 400 to 1200 rpm under the welding speed of 100 mm/min. The highest tensile strength they achieved was 333 MPa, which was about 60% of the base aluminum alloy. Moreover, they reported an exponentially increasing relationship between the interface strength and the reducing thickness of intermetallic compound (IMC) layer, which had the composition of $FeAl_3$. Lee et al. [19] did experiments on FSW of Al 6056-T4 to 304

stainless steel with the thickness of 4 mm under the rotational speed of 800 rpm and welding speed of 80 mm/min. The thin intermetallic compound (IMC) layer of 250 nm thickness was analyzed through transmission electron microscopy (TEM) and identified to be $FeAl_4$. Chen and Kovacevic [21] joined Al 6061 to AISI 1018 steel with the thickness of 6mm. Local melting of aluminum occurred, and shearing off of steel platelets encompassed by IMC layers of Fe_4Al_{13} and Fe_2Al_5 was observed in the weld nugget. The local partially melted aluminum was also reported by Jiang et al. [22] when they studied the same pair of dissimilar materials with the same thickness. Intermetallic compounds were found not only in the segregated steel clusters inside the nugget but also along the interface between base steel and the nugget. Their compositions were identified to be Fe_2Al_5 and Fe_4Al_{13}. The extent of IMC reaction varied with location, and more steel was consumed at a distance closer to aluminum alloy.

Movahedi et al. [7] did friction stir lap joining between Al 5083 and St -12 mild steel. They reported that the joint quality would not be degraded by an intermetallic compound layer with a thickness of less than 2 μm. Similar conclusions were again suggested by Lee et al. [71]. The 2 μm IMC layers with the composition of Fe_3Al or Fe_4Al_{13} was reported to contribute to the joint strength. Yilmaz et al. [72] concluded that an IMC layer was necessary for the Al-Fe interface strength, but cracks were easily initiated and propagated if the IMC layer reached a certain thickness. This statement was further verified by Bozzi et al. [73] when they studied friction stir spot welding of Al 6016 to IF-steel and reported that fractures were likely to be generated through the hard IMC tangles when the thickness of IMC layer was greater than 8 μm. In their studies, $FeAl_2$, Fe_2Al_5 and $FeAl_3$ were observed at different positions using TEM analysis. Chen et al. [23] did a parametric study of FSW on Al 6061-T651 to SS400 steel with the thickness of 6mm. They indicated that rotational and traverse speed were relatively significant FSW process parameters compared with

the tool tilt angle or pin diameter. Furthermore, lower rotational speed and transverse speed increased joint toughness. The maximum tensile strength they reached is 76% of the base Al alloy. Kimapong and Watanabe [74] did FSW lap joint on Al 5083 to SS400 mild steel and reported a maximum shear strength of about 77% of the Al base material. FeAl, $FeAl_3$ and Fe_2Al_5 were found at interfaces obtained from welding conditions of different tool tilt angles. Chen et al. [75] suggested that the Zn coating on steel could improve the weldability of Al and steel through promoting the formation of Al-Zn low melting point eutectic structure. They also reported in another study [76] on FSW lap joining that the thickness of IMC layer increased from 7.7 μm to 58.1 μm with decreasing welding speed, which substantially affected the joint strength. The composition was identified to be mainly Fe_2Al_5 and Fe_4Al_{13}. Watanabe et al. [77] did FSW of Al 5083 to A36 mild carbon steel with the thickness of 2mm. The maximum tensile strength was about 86% compared with the base Al alloy, which was achieved by shifting the tool into aluminum side and leaving 10% of the pin cross sectional area in the steel region. The fracture path of the tested tensile specimens was along the interface between Al matrix and Fe fragments. IMCs with the composition of FeAl and $FeAl_3$ were reported at the upper region of the weld interface.

All the aforementioned studies selected either mild steel or austenite stainless steel, both of which had a relatively low yield strength. Few open literatures discussed FSW of aluminum alloy to advanced high strength steels (AHSS), which is more desirable in lightweight vehicle structures. In this chapter, the feasibility of using FSW to join Al 6061 to TRIP 780 / 800 steel is investigated and effects of different process parameters are analyzed. Welding force and temperature are measured during the process. Macrostructure and microstructure analysis is performed on joint cross sections, which are further related to the measured welding force and temperature under

different welding conditions. Finally, the joint tensile strength is evaluated and failure modes are analyzed based on different joint macrostrucutures.

3.2 Study of FSW of Al 6061 to TRIP 780/800 steel

3.2.1 Experimental configuration

Figure 3-1 (a) is a schematic illustration of the experimental setup and Figure 3-1 (b) shows a more detailed cross-sectional view perpendicular to the weld line. Chemical compositions and mechanical properties of the aluminum alloy Al6061-T6511 are listed in Table 3-1, where UTS stands for ultimate tensile strength and YS is the yield strength.

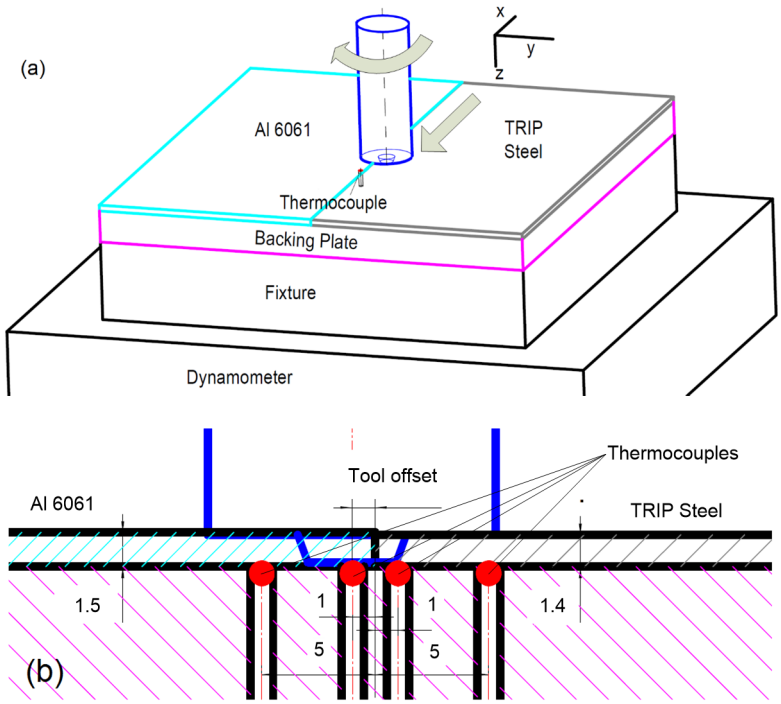

Figure 3-1 Schematic illustration of the FSW experimental configuration: (a) Overview; (b) Cross-sectional view perpendicular to the weld line (Unit: mm)

Table 3-1 Chemical composition and mechanical properties of the Al6061-T6511 alloy

Chemical composition (wt%)							**Mechanical properties (MPa)**	
Si	Mg	Fe	Cr	Cu	Zn	Ti	YS	UTS
0.60	1.00	0.35	0.42	0.27	0.12	0.08	245	283

The FSW tool used in this study comprises a conically tapered non-threaded pin. Detailed dimensions of the tool are shown in Figure 3-2. During all the experiments, the FSW tool is shifted towards aluminum side to reduce the large amount of heat generated from plastic deformation of steel, which is likely to melt aluminum and create various weld defects [15]. On the other hand, if the tool is shifted to aluminum to a much larger distance, effective bonding between the two materials can hardly be achieved due to insufficient steel in the weld nugget. The parameter of tool offset is therefore introduced and defined as the distance between the tool axis and the faying surface of the two materials. Larger tool offset means that the tool is more into aluminum and the joint strength can be expected to be improved by optimizing the value of tool offset.

Since certain fraction of the FSW tool remains immersed in steel region to actually stir both materials together, the FSW tool will be subjected to severe frictional conditions and needs to be made of refractory materials such as tungsten carbide [78], tungsten-rhenium [79], Si_3N_4 [80] and polycrystalline cubic boron nitride (PCBN) [81]. In this study, tungsten carbide with 10% cobalt was used for its combined properties of high hardness, relatively good fracture toughness and much lower cost compared with PCBN.

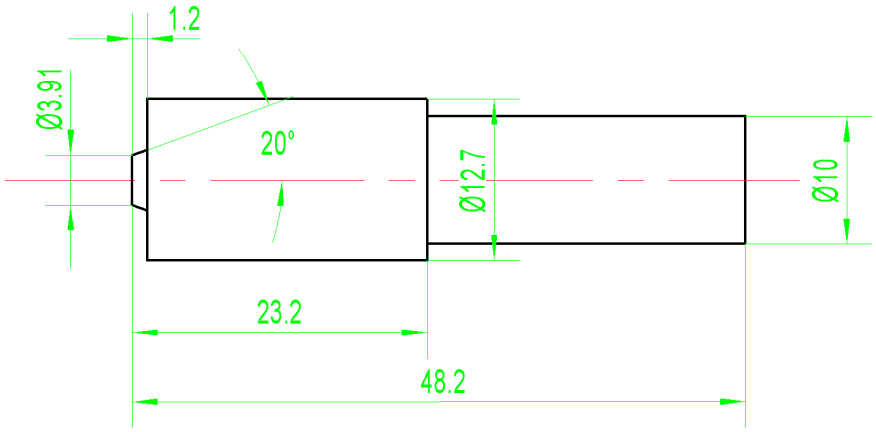

Figure 3-2 Detailed dimensions of the FSW tool (Unit: mm)

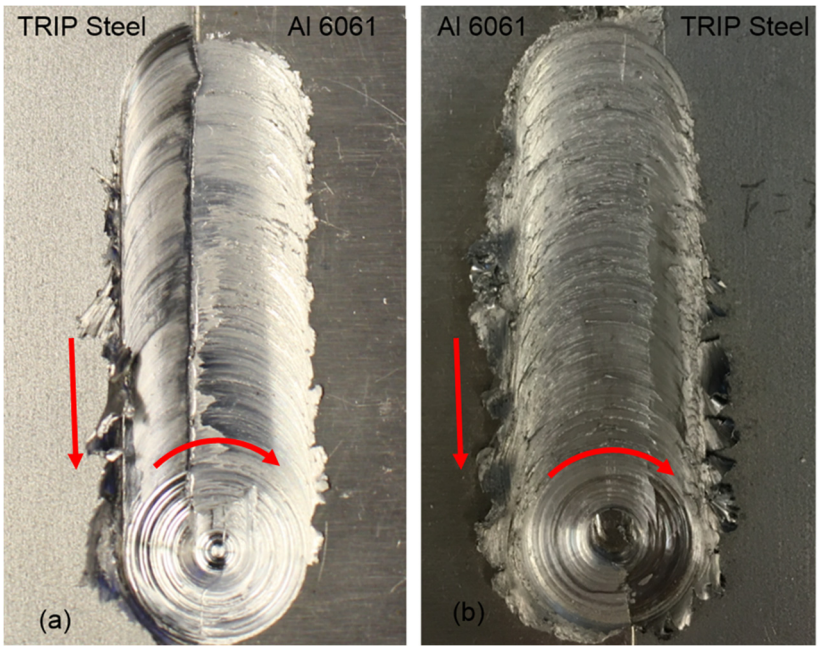

Figure 3-3 Weld top surface with steel placed at (a) Retreating side; (b) Advancing side

Below the workpiece is a replaceable backing plate made of mild steel, where four holes with diameter of 1mm were drilled for mounting thermocouples. Type K thermocouples are located symmetrically to the weld line and can measure the temperature of the workpiece back surface at distances of 1 mm and 5 mm away from the abutting edge. The workpiece and replaceable backing plate were assembled onto a specially designed fixture, which was further mounted onto a dynamometer, Kistler 9255B. The dynamometer can measure the mechanical welding force in both the axial direction, F_z and the direction along joint line, F_x. All FSW experiments were performed on a high stiffness M.S. Machining Center with displacement control.

Since the processing condition is unsymmetrical with regard to weldline during FSW, effects of relative positions of the two materials were investigated. In Figure 3-3 (a), steel is placed in the retreating side, where the tool rotating speed is opposite to the welding direction. On top of the weld surface, a clear interface between the two materials can be observed, which is associated with surface cracks. On the other hand, when steel is placed in the advancing side where tool rotating

speed is the same as welding speed, a well stirred weld surface can be obtained, as shown in Figure 3-3 (b). This can be explained from the movement of material in the wake of the tool. Due to the tool rotating motion, steel and aluminum moves in the same direction but at different rates. At approximately same temperature rise, the intrinsic softer properties of aluminum yields a much better plastic flow behavior compared with that of steel. With steel placed in the retreating side, as the tool passes by, steel tends to be pushed towards aluminum. However, an effective bonding can hardly be achieved due to the poor flowability of steel. When steel is placed in the advancing side, aluminum can then be effectively pressed against steel to obtain reliable joints. Therefore, steel was placed in the advancing side in all following experiments.

Three levels of rotational speeds were initially attempted. Acceptable joints could hardly be obtained under the lowest level of 600rpm regardless of choices of other parameters. A visible groove adjacent to the joint line existed on aluminum top surface, as shown in Figure 3-4, which suggests material leakage from weld nugget. This defect is likely to be caused by insufficient heat generation rate associated with the low rotational speed.

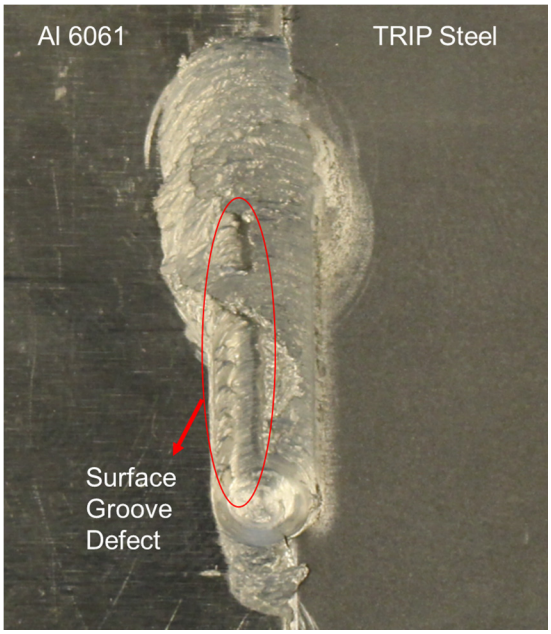

Figure 3-4 Weld samples obtained from rotating speed of 600 rpm

In the following studies, only the two higher levels of rotational speed, 1200rpm and 1800rpm were investigated under three levels of welding speed and two levels of tool offset. The welding conditions are listed in Table 3-2, where *R*, *v* and Offset are abbreviations for rotational speed, welding speed and tool offset respectively. Each condition was repeated three times for welding force and temperature measurement and two times for tensile tests. In plunge stage, the plunging speed was 10 mm/min. Based on the workpiece thickness and FSW tool pin length, the total plunge depth was selected as 1.3mm, where the starting position is defined as the pin end surface touches workpiece top surface.

Dimensions of the dogbone tensile specimens were designed according to the ASTM: E8 standard and the welded area was located near the center, as shown in Figure 3-5. The specimens were obtained by milling process, as shown in Figure 3-6. Tensile tests were performed on a MTS Insight 10 tensile machine at a strain rate of 10^{-3}/s. Microstructural analysis on joint cross sections was performed with optical microscopy (OM) and Scanning Electron Microscopy (SEM). X-Ray diffraction (XRD) analysis and Energy Dispersive Spectrometry (EDS) techniques were also applied for the determination of the Al-Fe interfacial layer composition.

Table 3-2 Process parameters studied in FSW of Al 6061 to TRIP steel

FSW condition	Rotational speed (R): rpm	Welding speed (v): mm/min	Tool offset (Offset) : mm
1	1200	30	1.03
2	1200	60	1.03
3	1200	90	1.03
4	1200	30	1.63
5	1200	60	1.63
6	1200	90	1.63
7	1800	60	1.03
8	1800	90	1.03
9	1800	120	1.03
10	1800	60	1.63
11	1800	90	1.63
12	1800	120	1.63

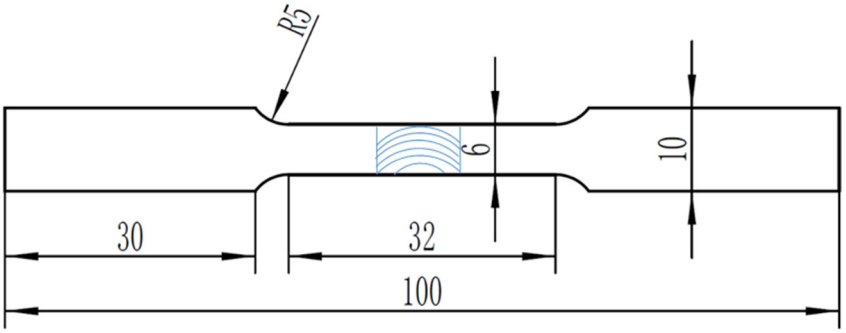

Figure 3-5 Tensile specimens with the weld in the center (Unit: mm)

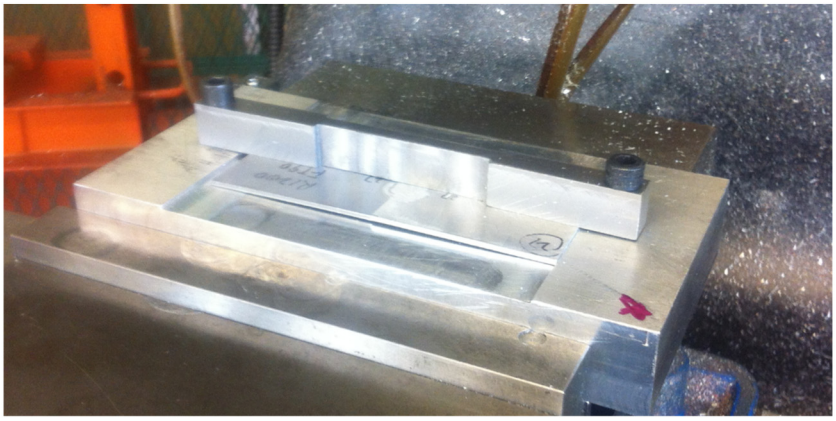

Figure 3-6 Milling process to obtain tensile specimen from the weld

3.2.2 Force and temperature measurement

3.2.2.1 Mechanical welding force

Typical curves of the axial and traverse forces experienced by FSW tool during the whole process are shown in Figure 3-7. During the plunge stage where the rotating tool pin was gradually inserted into workpiece, the axial force F_z increased rapidly in the beginning until it arrived at an intermediate plateau, which continued for a short period, and then increased again until it reached the peak value when the tool shoulder started abrading against the workpiece top surface. In the subsequent dwell stage where the tool was held rotating in position, axial force F_z decreased a little and translational force F_x remained negligible. Finally during the welding stage where the tool translated along the weld line, F_z further decreased and gradually arrived at a stable value. F_x

increased instantaneously due to the translational motion of the tool and after certain period of fluctuations also reached a stable value.

Compared with the works of Trimble et al. [82], Soundararajan et al. [83] and Park [84] on FSW of aluminum alloys, there are three distinct features of the force curves for FSW of aluminum alloy to steel. First, during the plunge stage of same aluminum alloy, the axial force curve increased in the beginning and then decreased before it increased again to the final peak. This temporary force decrease was generally considered from the aspect that as the tool pin gradually moved into the workpiece, the heat generated by plastic deformation and friction would reach an overshoot level where material was greatly softened. As a consequence, the required force for pushing the pin further in was reduced. On the other hand, as the tool is plunged into aluminum alloy and steel, the volume of the pin immersed in the steel side continuously grows larger due to its cone geometry. The surplus heat from friction and plastic deformation is then consumed to deform the extra steel. Accordingly, during dissimilar plunge stage, the axial force curve increases in the beginning and reaches a short intermediate plateau. This plateau was quickly broken when the tool shoulder started contacting top surface of the workpiece.

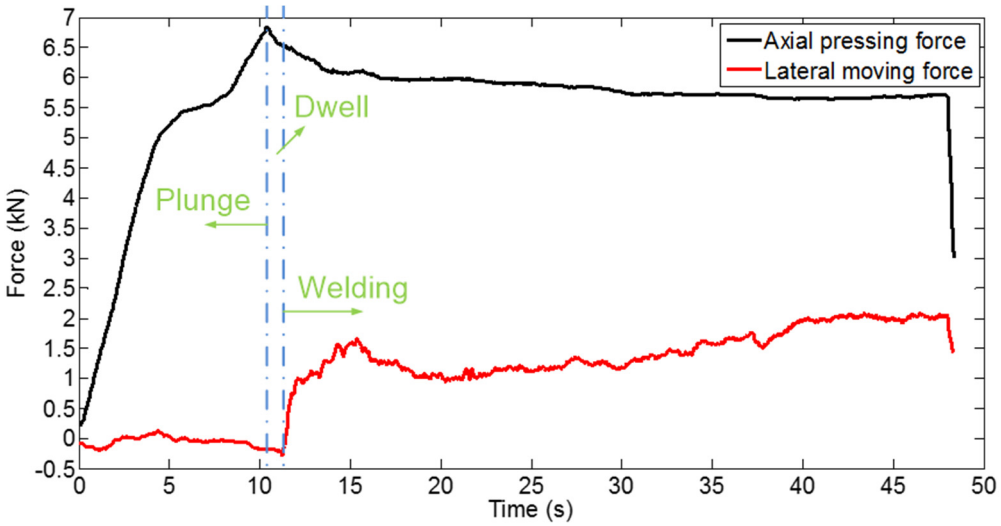

Figure 3-7 Typical axial and traverse forces on the FSW tool during the whole process

Second, when joining similar aluminum alloys, axial force F_z can be reduced by 35%~60% [82, 84] during welding stage whereas no more than 20% reduction is observed when joining Al to TRIP steel. Third, the translational moving force F_x, which is the force required for translating FSW tool along weld line, is negligible when welding aluminum. In contrast, F_x is much larger when welding aluminum to TRIP steel. The second and third differences can both be interpreted based on the fact that TRIP steel possesses much stronger mechanical properties, which make it more difficult to be confined within the weld and stirred along the joint line.

The mechanical welding force exerted onto the FSW tool depends on different process conditions for displacement controlled FSW process. In order to evaluate their effects, three characteristic values were selected for quantitative comparison of the force curves. The first one is the peak axial force F_z during plunge stage. The second and third values are the stable axial force F_z and translational moving force F_x during welding stage. Figure 3-8 compares the effects of tool rotational speed and tool offset on the peak axial force during plunge stage. Higher rotational speed and tool offset can effectively reduce axial force for initiating the process. Raising the rotational speed can increase the material shear strain rate and the relative velocity between the pin surface and material, which therefore promotes both plastic and frictional heat generation rate. Smaller volume of the pin in the stronger steel side can also reduce the required axial force to plunge the tool into the workpiece.

Figure 3-9 compares the stable axial force F_z during welding stage under different values of welding speed, rotational speed and tool offset. Overall F_z increases slightly with the traverse welding speed whereas the relationship is weak in the range of the studied welding speeds. On the other hand, larger rotational speed and tool offset can effectively reduce axial force, which suggests

that the required pressure for confining the material within the weld as the tool translates can be reduced in these conditions.

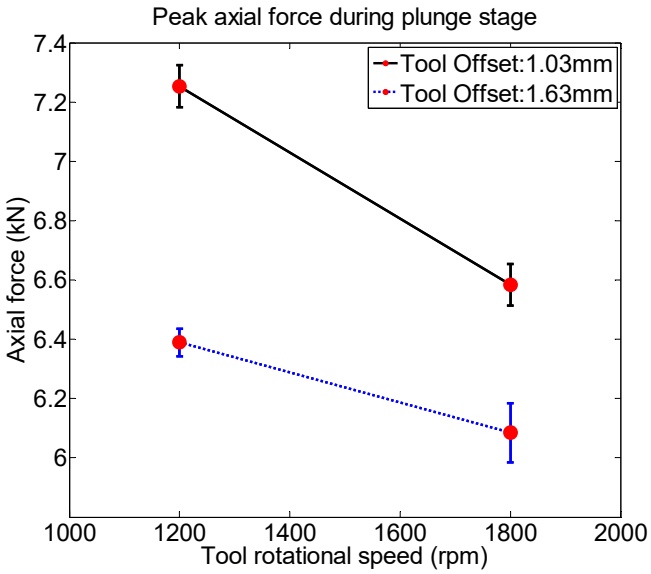

Figure 3-8 Effects of rotational speed and tool offset on the peak force F_z during plunge stage

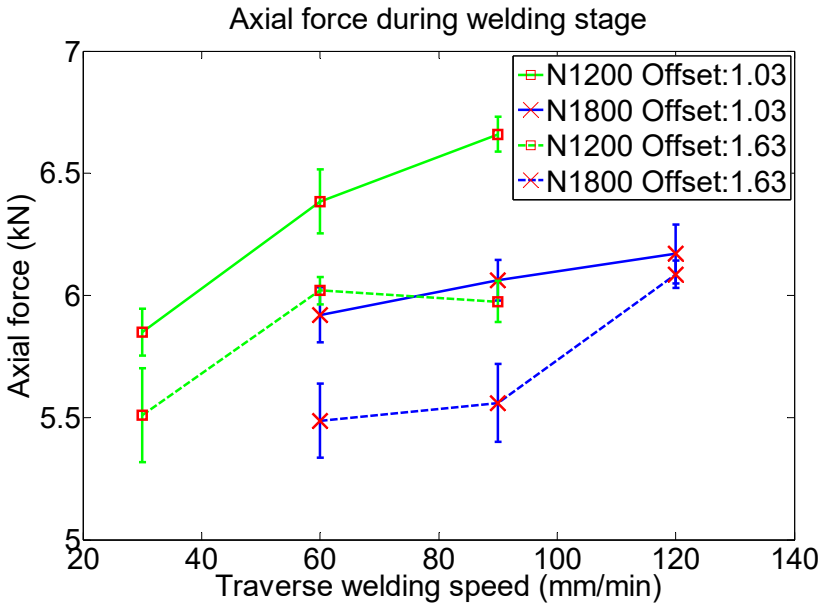

Figure 3-9 Effects of process parameters on the axial force F_z during welding stage

Translational moving force F_x during steady-state welding stage under different sets of process parameters is compared in Figure 3-10. In the studied range of the welding speed, its

effects on F_x is small. Higher rotational speed can reduce F_x but the influence is not as significant as that for F_z. Increase tool offset can also efficiently reduce F_x. However, if the tool offset increases too much, the joint quality may deteriorate due to insufficient amount of steel in the weld nugget.

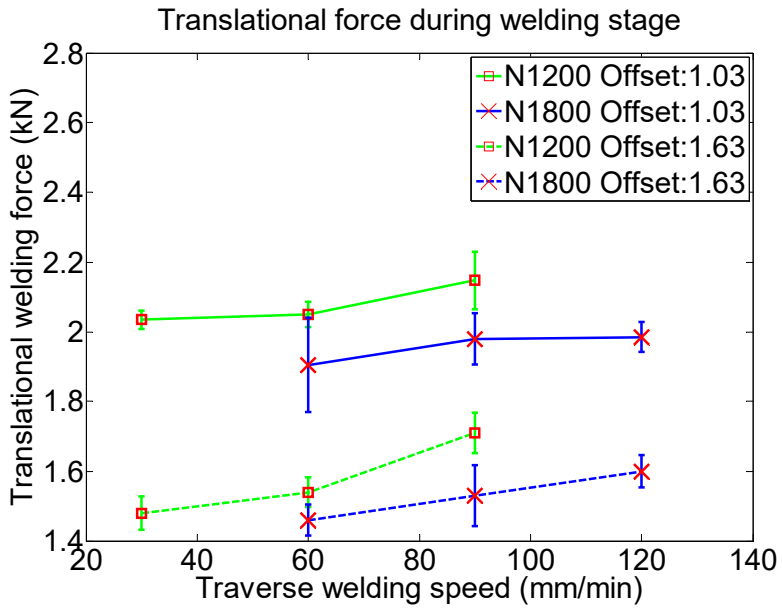

Figure 3-10 Effects of process parameters on lateral moving force F_x during welding stage

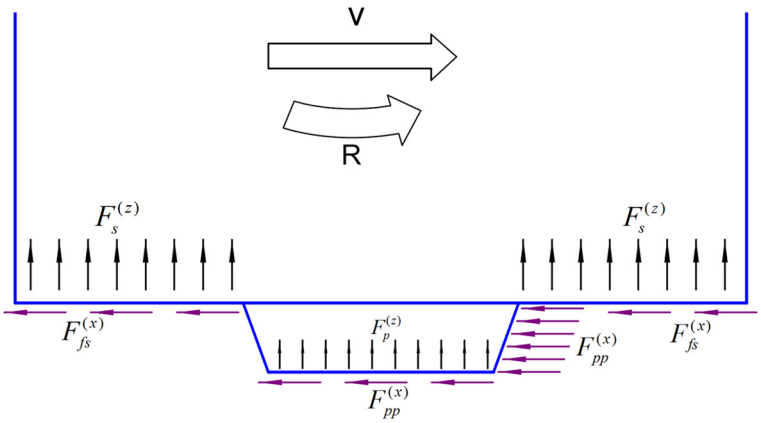

Figure 3-11 Schematic illustration of the force distribution on FSW tool (Side view parallel to the weld line)

A schematic illustration of the force distribution on FSW tool during the process is shown in Figure 3-11. Axial force comes from two parts: the surface of the pin and the shoulder. Each of

them consists of force components from aluminum and steel regions. The total area of shoulder surface is denoted as A_s, the end surface area of pin as A_{pz} and the periphery surface area of pin as A_{px}. Area fractions of aluminum on shoulder surface, pin end surface and pin periphery surface are denoted as f_s, f_{pz}, and f_{px} respectively. The following equations can then be established:

$$F_z = F_s^{(z)} + F_p^{(z)} = \iint_{f_s A_s} \sigma_{Al} dA + \iint_{(1-f_s)A_s} \sigma_{Fe} dA + \iint_{f_{pz} A_{pz}} \sigma_{Al} dA + \iint_{(1-f_{pz})A_{pz}} \sigma_{Fe} dA \tag{3-1}$$

$$\begin{aligned} F_x &= F_{fs}^{(x)} + F_{pp}^{(x)} = \mu_{Al} F_{Al}^{(z)} + \mu_{Fe} F_{Fe}^{(z)} + \iint_{f_{px} A_{px}} \sigma_{Al} dA + \iint_{(1-f_{px})A_{px}} \sigma_{Fe} dA \\ &= \iint_{f_s A_s} \mu_{Al} \sigma_{Al} dA + \iint_{(1-f_s)A_s} \mu_{Fe} \sigma_{Fe} dA + \iint_{f_{px} A_{px}} \sigma_{Al} dA + \iint_{(1-f_{px})A_{px}} \sigma_{Fe} dA \end{aligned} \tag{3-2}$$

where $F_{fs}^{(x)}$ represents the frictional force on the shoulder and $F_{pp}^{(x)}$ is the deformation resistance of plasticized material exerted on the pin. μ is the frictional coefficient and σ is the flow stress, which is a function of temperature, strain and strain rate. It can be shown in the following session that higher rotational speed can elevate the temperature in the nugget, which therefore reduces the stress terms in equation (3-1) and accordingly the axial force. Values of f_s, f_{pz}, f_{px} are determined by the parameter of tool offset. Larger tool offset means higher values for these three variables, which implies aluminum deformation stress occupies a greater portion of the total F_x and F_z and therefore the forces can be reduced.

The welding speed v in the following shows an insignificant effect on the maximum temperature during the process. The influence of welding speed on strain rate can be compared with that of rotational speed by calculating the ratio between the average material moving speed induced by tool rotation and that induced by translation:

$$\frac{v_{rotation}}{v_{translation}} = \frac{\int_0^{r_s} r \cdot 2\pi R \cdot 2\pi r dr \Big/ \pi r_s^2}{v} = \frac{2}{3} \pi r_s \frac{2\pi R}{v} \tag{3-3}$$

where r_s is the tool shoulder radius, R is the rotational speed and v is the welding speed. After substituting the lowest rotational speed of 1200 rpm, the highest welding speed of 120mm/min and the shoulder radius of 6.35mm into this equation, the ratio is 900. This indicates that the strain rate of the material is primarily determined by the rotational speed. Welding speed in the studied range affects stress distribution to a smaller extent, and the axial and translational moving force is accordingly slightly affected.

3.2.2.2 Temperature measurement

Figure 3-12 compares the temperature distribution under different welding speeds with the rotational speed of 1800 rpm and the tool offset of 1.63 mm. The Y axis represents the peak temperature recorded at this position during the entire welding process. As described in the experimental configuration, the four temperature measuring points are symmetric to the abutting edge. Since FSW tool is shifted more into Al side during all experiments, the thermocouples are asymmetric with regard to the tool, which helps explain the result that the temperature at 1 mm position in Al side is slightly higher than that in steel side. The welding speed in the studied range has an insignificant effect on the temperature distribution in Al side. Similar results were also reported by Barnes et al. [79]. Smaller welding speed can slightly increase the temperature in steel side, which can be considered from the aspect of thermal history. Figure 3-13 shows the effect of welding speed on thermal history at 1mm position in Al side under the same condition as in Figure 3-12. Smaller welding speed can directly extend the high temperature period and reduce heating and cooling rate. Heat generated in Al side can accordingly have a longer time to be conducted into steel and raise the temperature. Similar results regarding the effect of welding speed on

temperature distribution are shown in Figure 3-14, where a smaller rotational speed of 1200 rpm is applied.

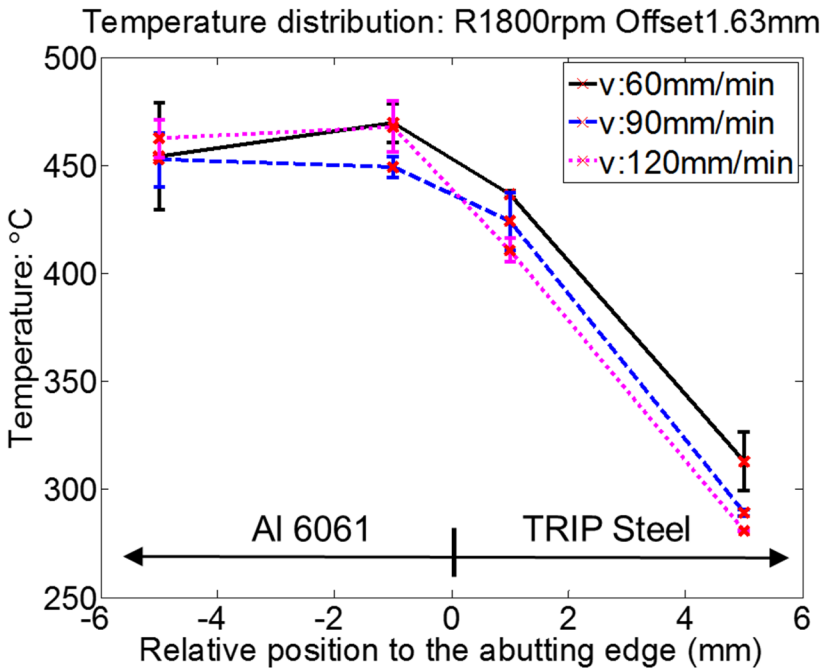

Figure 3-12 Temperature distribution under different welding speeds (1800 rpm; tool offset 1.63mm)

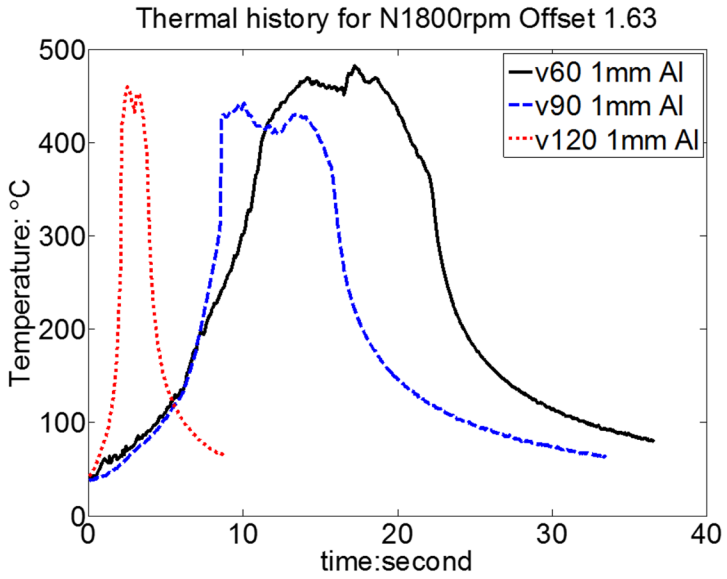

Figure 3-13 Thermal history at 1mm position in Al side under different welding speeds (1800 rpm; tool offset 1.63mm)

Figure 3-15 shows the effects of different rotational speeds on the temperature distribution. Temperature in both aluminum and steel sides is higher under a larger rotational speed. This conclusion is consistent regardless of welding speeds.

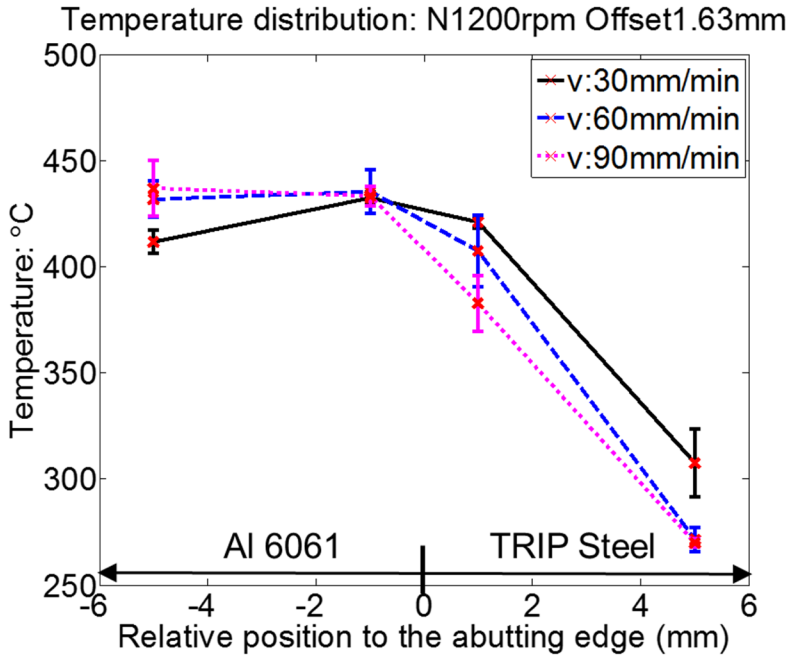

Figure 3-14 Temperature distribution under different welding speeds with rotational speed of 1200 rpm and tool offset of 1.63mm

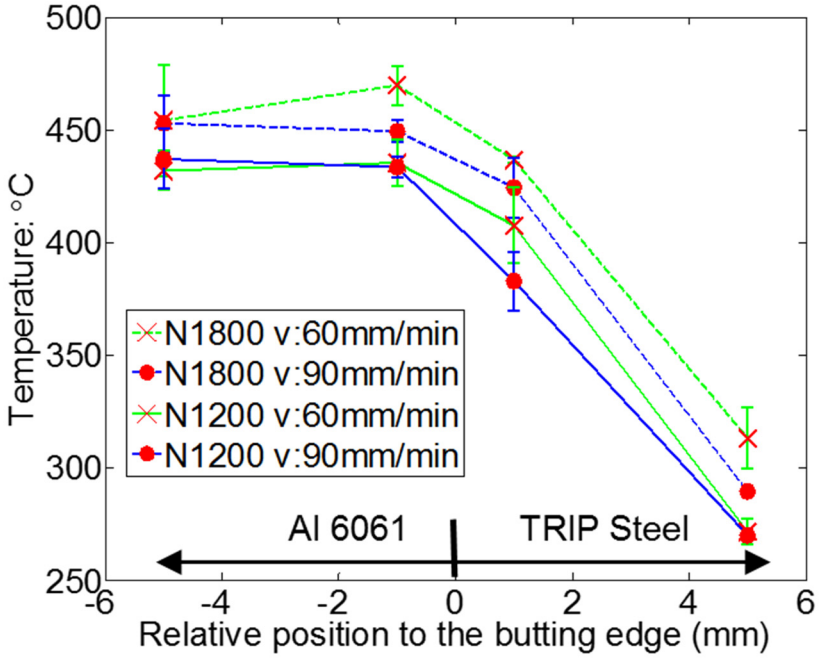

Figure 3-15 Temperature distribution under different rotational speeds (Tool offset: 1.63mm)

3.2.3 Joint quality evaluation

3.2.3.1 Macroscopic analysis on joint cross section

A typical optical macro-image of the weld cross section perpendicular to the abutting edge is shown in Figure 3-16, which reveals a good quality joint containing neither visible pores nor cracks. Three features can be extracted for characterizing advancing side, retreating side and weld nugget respectively. In the advancing steel side, a tilted interface between aluminum and steel can be observed and the inclination angle, which is defined as the angle between the vertical direction and the direction of this interface, is larger than the original cone angle of the tool pin. This could be explained from the aspect of heat distribution. Large amount frictional heat will be generated at the interface of tool shoulder and workpiece top surface. Top region of the weld therefore receives greater amount of both conduction heat and plastic deformation heat associated with the larger pin radius. The elevated temperature can therefore reduce the steel deformation resistance to a larger extent and promote the penetration of stirred over aluminum into steel side.

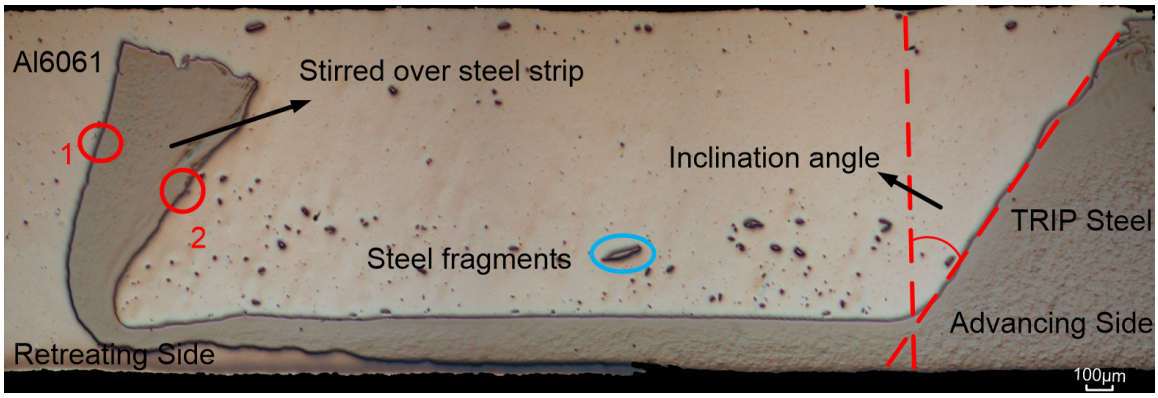

Figure 3-16 Macrostructure of the cross section perpendicular to the weld line (1800 rpm, 60mm/min, tool offset of 1.63mm)

The effect of different welding speeds on the inclination angle of this interface is shown in Figure 3-17. In the condition of the lowest welding speed of 30mm/min in (a), the Al-Fe interface still preserves a linear morphology. As the welding speed increases to 60mm/min in (b), the

interface started to show certain degree of curvature and a higher inclination angle can be observed in the upper region. The highest welding speed of 90mm/min in (c) leads to a distinct curved shape and the interface is even more flat in the top region. Based on the results of previous session, the length of thermal cycle is directly reduced under a larger welding speed. This results in less amount of frictional heat being conducted downward and accordingly a more nonuniform temperature distribution in the weld nugget, as also reported by Leitao et al [85]. The difference of steel flow stress between top and bottom region will be larger and lead to a more curved interface geometry.

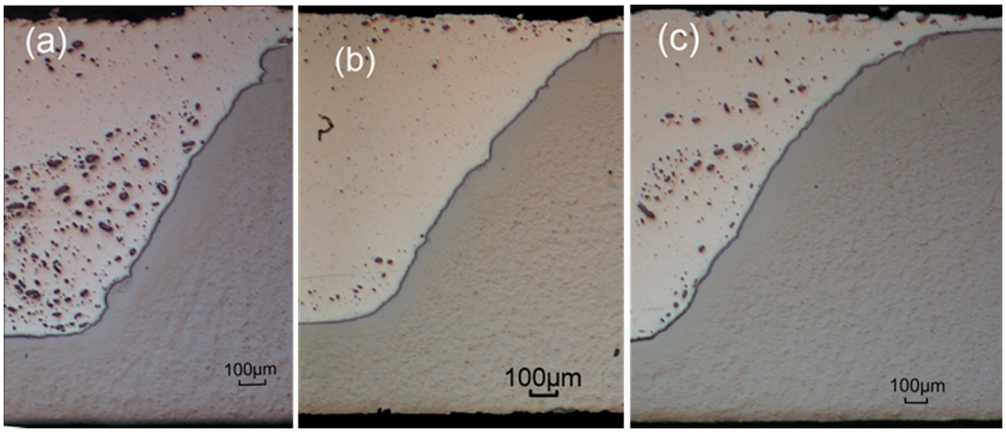

Figure 3-17 Effect of welding speed on the inclination angle of Al-Fe interface in the advancing side (1200 rpm; tool offset 1.63mm): (a) 30; (b) 60; (c) 90 mm/min

In order to evaluate the effects of other process parameters on the inclination angle, including rotational speed and tool offset, this Al-Fe interface in the advancing side was linearly fitted and the average angle was calculated for each welding condition. Figure 3-18 shows that larger welding speed can consistently increase the inclination angle regardless of the values of the other process parameters. Higher rotational speed generally results in a smaller angle, which suggests that the nonuniform temperature distribution due to larger welding speed can be ameliorated. On the other hand, the influence of the tool offset depends on other process parameters. Overall, smaller tool offset increases the inclination angle of the interface. This could be attributed to the involvement

of larger fraction of steel and its lower thermal conductivity, which increases the temperature gradient.

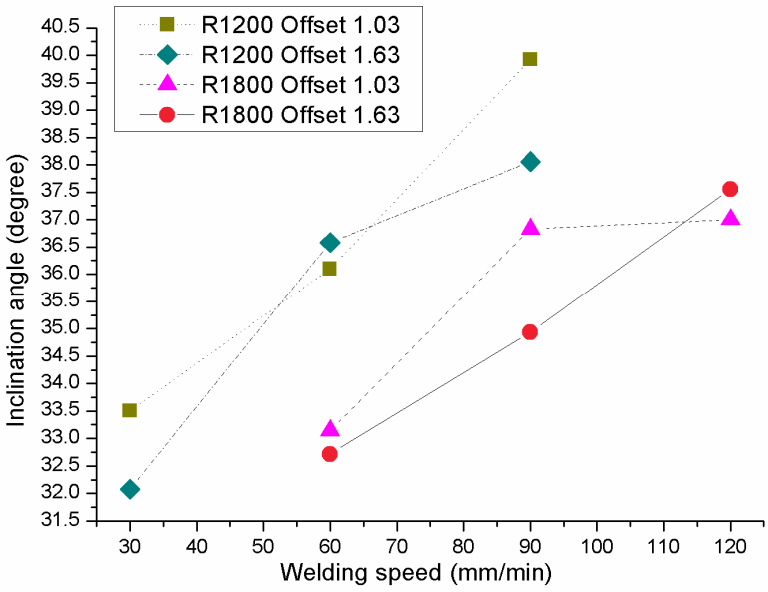

Figure 3-18 Effects of welding parameters on the inclination angle of Al-Fe interface in steel side

The second feature of the macrostructure for joint cross section is the occurrence of a continuous steel strip embedded in the aluminum matrix in the retreating side, as shown in Figure 3-16. This illustrates the pattern of material flow during this FSW process: A continuous steel strip is peeled off from the base TRIP steel side and extruded into the aluminum matrix. In the advancing side, the materials from aluminum region has been stirred over and pushed against steel. Vertical force exerted by the pin of FSW tool tends to press this part of aluminum and steel downward, which is restricted by the backing plate when they reached the bottom of the nugget. Since total length of the pin is less than the thickness of the workpiece, the materials at the bottom of advancing side therefore can be squeezed and move horizontally into aluminum side through the "strait" formed by the end surface of the pin and the backing plate. The softer properties of aluminum matrix make it easier for the TRIP steel to penetrate. TRIP steel will tend to follow the flow of aluminum in the retreating side once being transported through the "strait". According to

Guerra et al. [86] and Colligan [87], the materials tend to be carried away and deposited in the wake of the pin as the tool continuously moves forward.

In addition, the geometry of the steel strip suggests an upward motion, which can be explained as the followings: As shown in the curved Al-Fe interface in the advancing side, the top region of the weld has a higher temperature and smaller flow stress than the bottom. Relatively larger amount of materials is able to move backward and the materials in the bottom will then try to occupy this available space from the tool pressure. Accordingly, materials tend to flow upward. Similar results regarding the upward motion were reported by Reynolds [88] and Coelho et al. [89]. This steel strip was initially expected to be beneficial and serve as a strengthening rib for the softer aluminum matrix. However, its contribution to joint quality closely depends on its interface with the surrounding aluminum matrix, which will be discussed in details with tensile test results.

The third feature for the macrostructure of the joint cross section is related to the nugget region. From Figure 3-16, particles with various sizes and morphologies are scattered around in the weld nugget. A series of SEM images were then taken at different positions for further examinations. Figure 3-19 shows that these particles are steel fragments embedded in the aluminum matrix. More importantly, all of them are encompassed with an intermetallic layer, which implies reactions instead of simply mixing between these sheared off steel platelets and aluminum matrix. Furthermore, particles of intermetallic compounds (IMC) in addition to steel fragments are also visible. They generally have much smaller sizes, which are around 2–5 μm for the largest dimension. These IMC particles are possibly generated from reactions between originally sheared off steel particles and aluminum matrix. These steel particles are completely consumed due to their small sizes. During tensile tests, fracture occurs at other regions instead of the weld nugget, which indicates these particles are acceptable for static strength. However, they

are potentially harmful for other applications and especially can serve as the initiation sites for fatigue cracks.

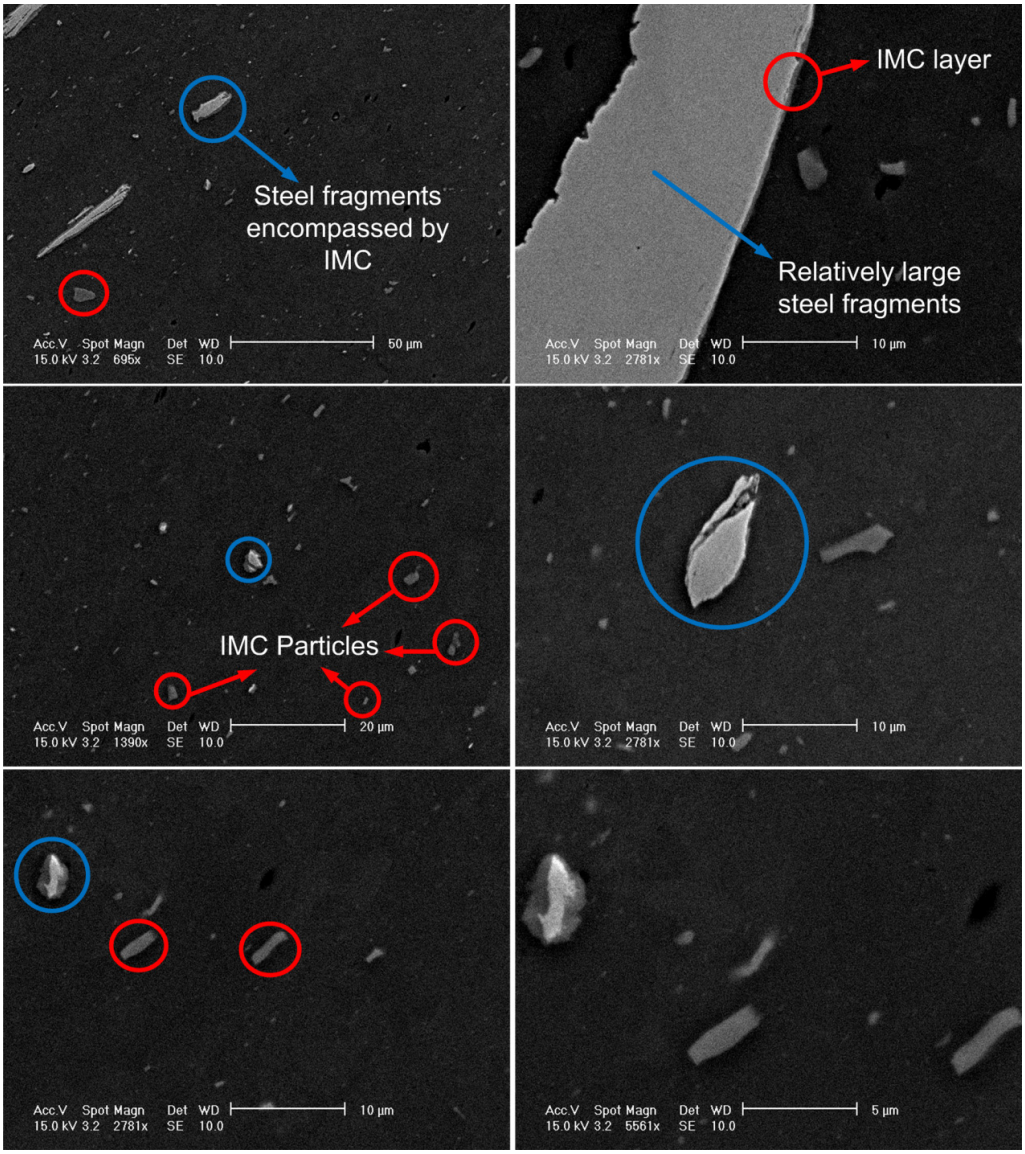

Figure 3-19 Particles in the weld nugget: IMC particles and steel fragments encompassed by IMC layer

A commonly observed weld discontinuity for FSW of similar aluminum alloys is the "wormhole" defect, which is a void that exists at the root of advancing side [90]. On the contrary, during FSW of dissimilar steel and aluminum in this study, the advancing side always exhibits a continuous interface without porosity or cracks. However, discontinuities can occur in the

retreating side as shown in Figure 3-20, which is always associated with the stirred over steel strip. Since the motion for this portion of steel is upward, the compressing interaction between aluminum matrix and the steel strip is relatively weak. Besides, the coefficient of thermal expansion for aluminum is much higher than that of steel, aluminum tends to shrink more during cooling, which promotes the formation of defects even if the weld is continuous at high temperature.

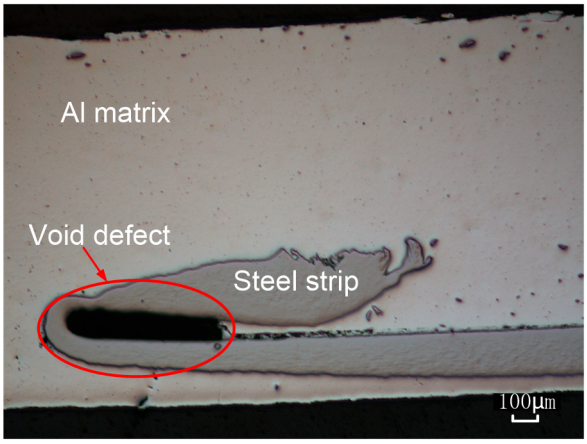

Figure 3-20 Void defect in retreating side (1800rpm, 120mm/min and tool offset of 1.63mm)

3.2.3.2 Al-Fe interface

In order to examine the metallurgical bonding conditions in the advancing side, scanning electron microscopy (SEM) was employed for higher magnified views. Figure 3-21 shows SEM images of the Al–Fe interface under different welding speeds, where the rotational speed is kept at 1200 rpm and tool offset is kept at 1.03 mm. A distinct interfacial layer with a different color from either steel or aluminum can be observed, which indicates a newly formed phase of intermetallic compounds (IMC). The intermetallic layer has a relatively smooth boundary in the dark aluminum side compared with the wavy morphology of the boundary in the bright steel side. Despite these coarse boundaries, the overall thickness of this interface layer becomes smaller as the welding speed increases. The relationship between interlayer thickness and welding speed is

consistent regardless of variations of other parameters, as shown in Figure 3-22 where a higher rotational speed of 1800 rpm and larger tool offset of 1.63 mm are applied.

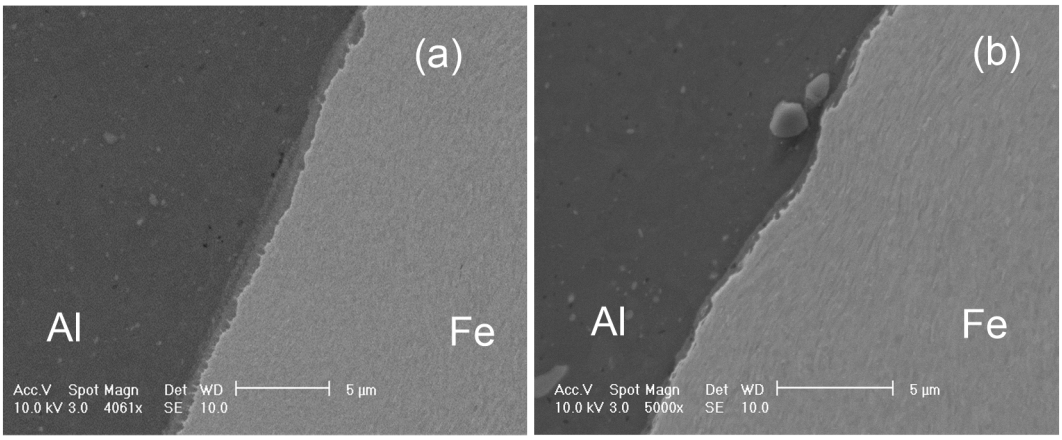

Figure 3-21 Al-Fe interface in the advancing side (1200 rpm: tool offset 1.03mm) under different welding speeds: (a) 30mm/min; (b) 60mm/min

Growing kinetics of this interlayer was further quantitatively studied by measuring its thickness under different sets of process parameters. Considering the unsmooth morphology near steel side, measurements are taken at three different subareas of each interface and in each subarea three peaks and valleys of the wavy boundary are selected. Average values of thickness t is plotted with respect to welding speeds v in logarithm scale as shown in Figure 3-23. A linear dependence of $ln(t)$ on $ln(v)$ can be observed. By further calculating the fitted slope, relationships between layer thickness t and welding velocity v under different rotational speeds and tool offsets are summarized in Table 3-3. The thickness is either proportional to the reciprocal of velocity or the square root of the reciprocal of velocity. Since the duration of welding stage for the same welding length is inversely proportional to v, this inverse relationship or inverse parabolic relationship between the thickness and the welding speed can be approximately interpreted as linear or parabolic relationship between the thickness and time. According to Bouche et al. [91], the growth of the intermediate phases follows linear kinetics if it is governed by chemical reactions. If the rate

determining step is interdiffusion, the growth rate follows parabolic relationship. Based on Table 3-3, in the condition of 1200 rpm rotational speed and 1.03 mm tool offset, the linear relationship between the thickness and the reciprocal of velocity indicates a reaction controlled interphase growth. On the other hand, the rate determining step in other three process conditions is more likely to be diffusion. Furthermore, the wavy morphology occurs at the steel-intermetallic boundary instead of the aluminum-intermetallic boundary, which indicates the diffusion of iron atoms is a slower step compared with the diffusion of aluminum atoms.

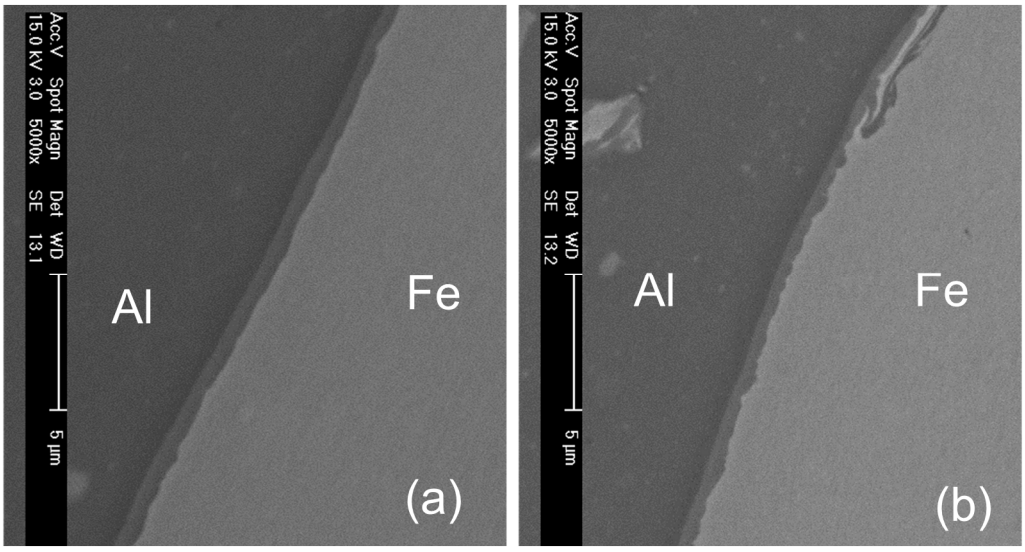

Figure 3-22 Al-Fe interface in the advancing side (1800 rpm, tool offset 1.63mm) under different welding speeds: (a) 60mm/min; (b) 90mm/min

Table 3-3 Dependence of the interlayer thickness *t* (μm) on the welding speed *v (mm/min)*

	Tool offset: 1.03mm	**Tool offset: 1.63mm**
Rotational speed: 1200 rpm	$t \propto \frac{1}{v}$	$t \propto \frac{1}{\sqrt{v}}$
Rotational speed: 1800 rpm	$t \propto \frac{1}{\sqrt{v}}$	$t \propto \frac{1}{\sqrt{v}}$

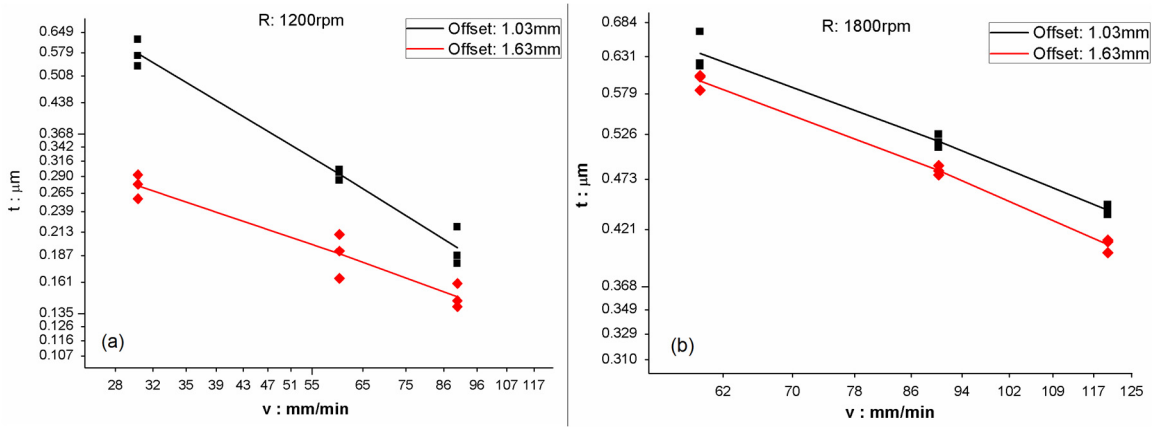

Figure 3-23 Relationships between the interlayer thickness *t* and welding speed *v* under different tool offsets and rotational speeds: (a) 1200 rpm; (b) 1800 rpm

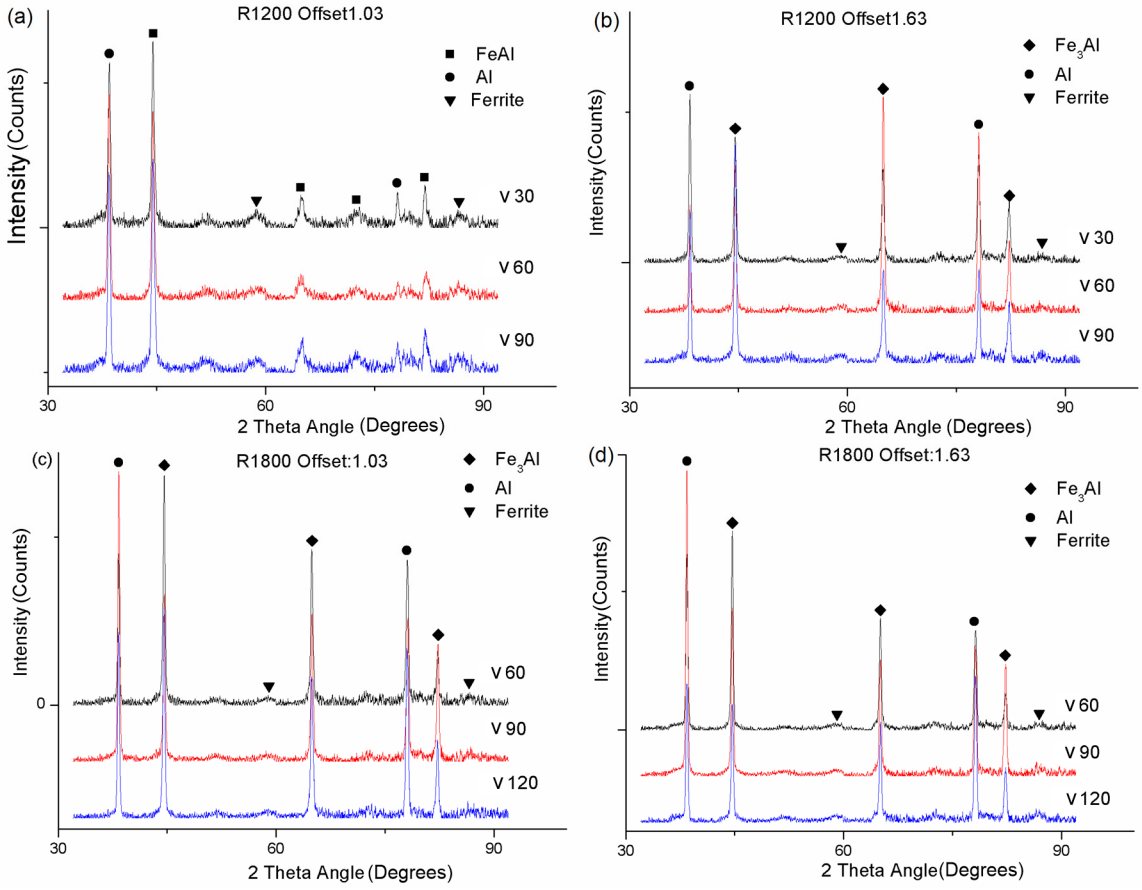

Figure 3-24 XRD patterns of the intermetallic layer in the advancing side under different process conditions

The composition of the IMC layer is identified with X-Ray diffraction (XRD) analysis and the results are shown in Figure 3-24. The most likely existed phases are determined based on the

figure of merit (FOM) values calculated from the XRD analysis software JADE. The welding speed *v* has no influence on the type of IMC that is going to form. Furthermore, only under the condition where rotational speed is 1200 rpm and tool offset is 1.03 mm can the FeAl phase be generated. Fe_3Al is formed under all other conditions, which are in agreement with the results of above kinetic analysis.

3.2.3.3 Relationship between process parameters and the Al-Fe interface

The formation and growth of intermetallic compound at the interface of dissimilar materials basically contain three stages [92]. The first stage involves the formation of solid solution through atomic diffusion at the interface. IMC will start to nucleate in the second stage when it is thermodynamically more favorable at corresponding temperature and pressure combinations. In the third stage, solute atoms will continue to diffuse into the stabilized IMC nucleus for it to grow gradually. Several studies were conducted regarding the interlayer formation and growth between molten Al and solid Fe [91, 93-96]. According to their studies, Fe_2Al_5 and $FeAl_3$ are more likely to be formed in the temperature range of 700 ºC to 900 ºC. On the other hand, IMC with lower aluminum composition, basically FeAl and Fe_3Al, can only be formed at a higher temperature of over 1000 ºC. The Al-Fe phase diagram under atmospheric pressure is shown in Figure 3-25 [97]. The formation of Fe_3Al occurs at the temperature of about 550 ºC through a peritectoid reaction while FeAl is formed through a peritectic reaction under a much higher temperature of around 1245 ºC. Based on the temperature measurement results in the previous session, the highest temperature at the back surface of the workpiece is around 500 ºC, which indicates a potentially high temperature gradient within the workpiece. Besides temperature, the effects of high pressure raised by the mechanical welding force during FSW also need to be taken into consideration for

the formation of FeAl and Fe_3Al intermetallics. It was reported in [98] that an increase in pressure could promote the formation of interface layer at lower temperature under constant diffusion time. Furthermore, during FSW, materials near the pin are subject to severe plastic deformation at a high strain rate. It is suggested that short-circuiting along static and moving dislocations, grain boundaries and cracks generated during deformation can enhance diffusion [99] and facilitate IMC nucleation by providing heterogeneous nucleation sites.

Above discussions show that the formation and growth of IMC layers depend closely on temperature, mechanical welding force and material deformation status, all of which are determined by process parameters. According to the previous temperature and welding force measurement results, higher rotational speed can effectively increase the temperature in the weld, reduce welding force in both vertical and lateral directions. In addition, it also increases the material strain rate, which should be positively correlated with the velocity of the corresponding points on the tool. Therefore higher rotational speed can enhance the diffusion process and promote the formation of greater amount of IMC.

Welding speed in the studied range has an inappreciable effect on either temperature distribution or mechanical welding force along both tool axial direction and weld direction. As a result, it could hardly affect diffusion or IMC reaction process and consequently the composition of the IMC layer. However, the extended high temperature period associated with lower welding speed allows for longer diffusion time, which results in the formation of thicker IMC layers. Smaller tool offset means larger fraction of steel is involved in the stirring process and react with aluminum, which will increase the interlayer thickness. It has been shown that under the lower rotational speed of 1200 rpm and smaller tool offset of 1.03 mm, FeAl is formed at the interface, which is different from the Fe_3Al obtained under all other conditions. The smaller tool offset is

shown to increase welding force along both axial and welding directions and can therefore elevate the pressure in weld nugget, which contributes to IMC reaction. However, the relatively low temperature resulting from the lower rotational speed retards further diffusion of iron atoms into the initially formed IMC layer with the composition of FeAl. As a result, FeAl can hardly be transformed into Fe_3Al and leaves as the interlayer composition under the lower rotational speed of 1200 rpm and smaller tool offset of 1.03 mm. For other conditions, temperature is higher and allows for the formation of Fe_3Al.

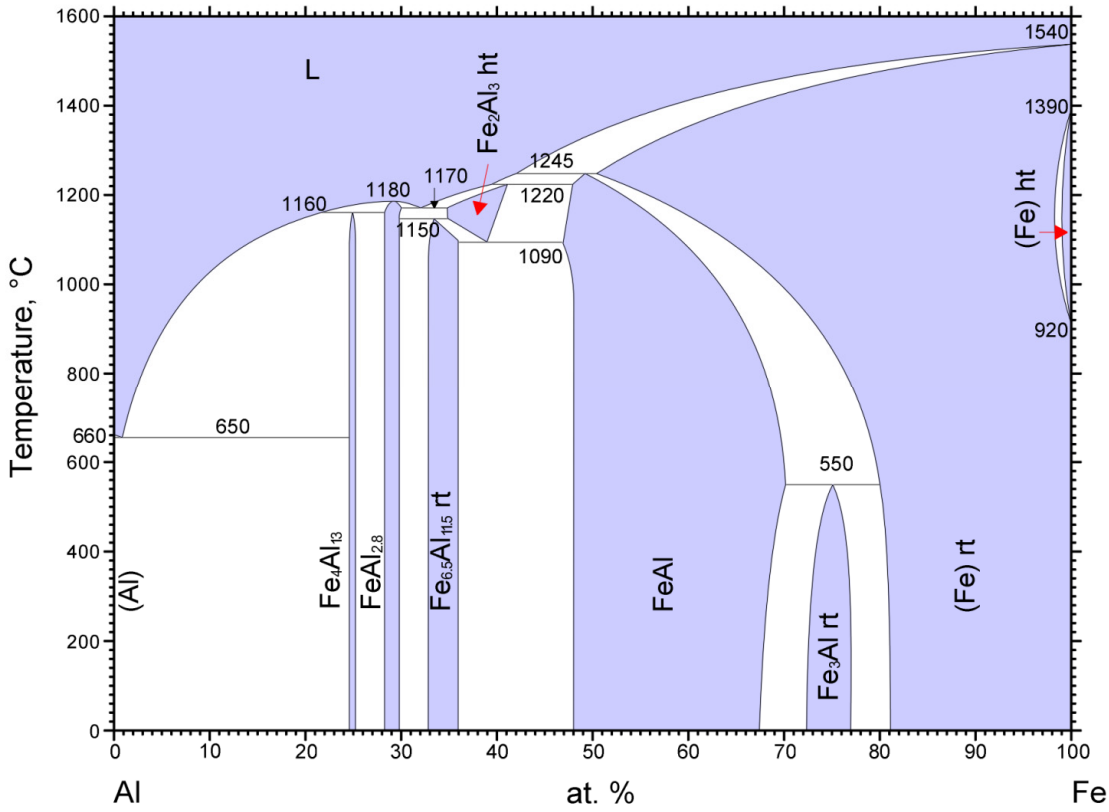

Figure 3-25 Al-Fe phase diagram under atmospheric pressure (ASM Alloy Phase Diagram Database, ASM International 2006, Diagram No. 904096)

3.2.3.4 Tensile strength and failure modes

Three types of failure modes occurred during tensile tests, as shown in Figure 3-26. The first two are related to the embedded steel strip. In Figure 3-26 (a), the steel strip penetrates the top

surface of the aluminum alloy in the retreating side. In this condition, the fracture path follows the inside boundary, marked as position 2 in Figure 3-16. This greatly deteriorates the joint quality and results in the lowest strength among the three failure modes, which is around 57% of the base aluminum alloy.

The most frequently encountered failure mode is shown in Figure 3-26 (b), where the steel strip is submerged beneath the workpiece top surface and the crack is initiated and propagated along the outside boundary, which is marked as position 1 in Figure 3-16. The corresponding tensile strength is around 79% of the base aluminum alloy.

Figure 3-26 (c) corresponds to the most satisfying failure mode where the fracture occurred in the heat affected zone of aluminum and the necking phenomenon can be observed. This condition results in the highest joint strength of 240MPa, which is about 85% of the base Al alloy. The Al 6061 sheets used in this study have been subjected to the T6 heat treatment, which is a peak aging process. A distribution of fine precipitates is achieved in the aluminum matrix from this process, which results in the highest strength with regard to the aging time. The loss of strength at the heat affected zone after welding is therefore caused by over-aging and coarsening of these precipitates.

During all the tensile tests, the fracture path is generally away from the original faying surfaces of the two materials. Furthermore, no cracks are generated in the weld nugget or the Al-Fe interface in the advancing side, which indicates a relatively stronger strength in these two regions compared with the regions near the extruded steel strip.

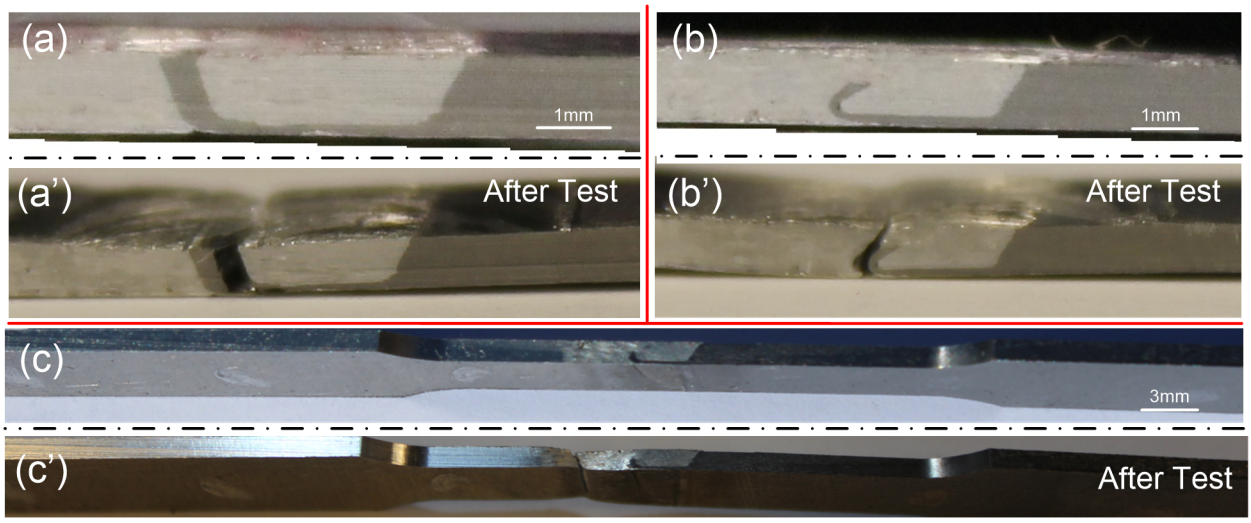

Figure 3-26 Three failure modes: (a) Cracks at the inside boundary of steel strip; (b) Cracks at the outside boundary steel strip; (c) Failure in the aluminum heat affected zone

In order to understand the underlying mechanisms of these observed failure modes, a series of SEM images were taken at various locations along the Al-Fe interface. Figure 3-27 shows the cross-section of the joints that fractured at the outside boundary of steel strip during tensile tests. The IMC layer exists at the Al-Fe interface in the advancing side as well as along the inside boundary of steel strip. Moreover, the thickness of this intermetallic (IMC) layer is less than 1μm. On the other hand, no intermetallic layer can be distinguished on the outside boundary of the steel strip, which means there is either no intermetallic or the thickness of this layer is in a much smaller nanometer scale.

The fracture of the tensile specimens along the outside boundary of the steel strip can therefore be attributed to two reasons: (1) The hook geometry of the stirred over steel strip generates a locally high stress state, which exceeds the aluminum/steel bonding strength and initiates the crack; (2) The bonding strength between aluminum and steel with no intermetallic or intermetallic layer with thickness in nanometer scale is relatively weak compared with that from intermetallic layer with submicron thickness. This is especially true if the stress from the applied

tensile load is uniformly distributed along the Al-Fe interface in the advancing side, outside boundary and inside boundary of the steel strip. The contribution of intermetallic compound to joint quality is closely related to its thickness and composition. A slight increase of the thickness of the IMC layer is likely to rapidly deteriorate the joint quality due to its brittle mechanical properties. Besides, the aluminum riched intermetallic compounds, such as Fe_2Al_5 and $FeAl_3$ are more brittle than iron riched ones, such as Fe_3Al and FeAl. Even under the same small thickness, the former one can be detrimental to joint strength.

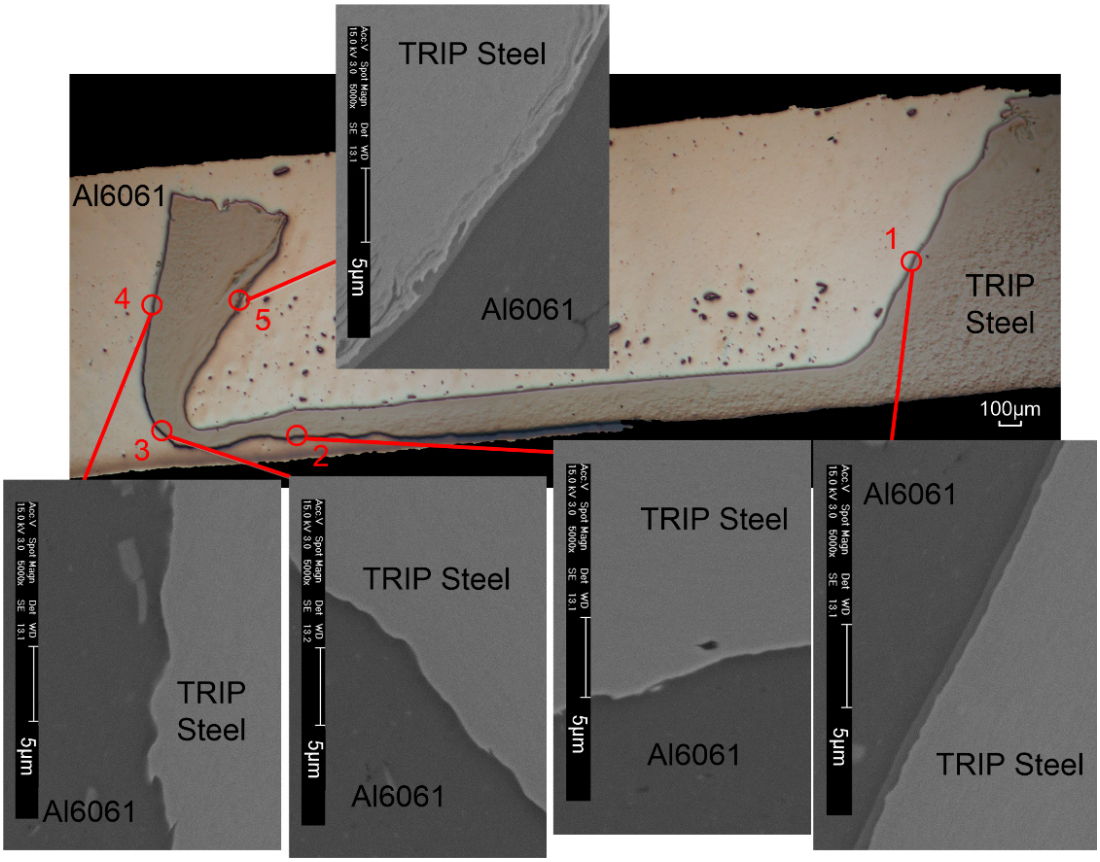

Figure 3-27 Al-Fe interface of the joint section with fracture path along the outside boundary of steel strip

For comparison, the cross section of the necking specimen is also analyzed using SEM and the results are shown in Figure 3-28. In this case, sheared off steel fragments are distributed with much smaller sizes and could hardly be recognized with the lower magnification optical

microscope. The presence of intermetallic layer can be observed along the Al-Fe interface not only in the advancing side but also at the stirred over steel strip. The vortex structure at the tip of the steel strip can be regarded as micro-interlocks between steel and aluminum, which is likely to enhance the interfacial strength. Elemental mapping through Energy Dispersive Spectrometry (EDS) analysis has also been conducted for the Al-Fe interface both at the tip of steel strip and in the advancing side. The results are shown in Figure 3-29 and Figure 3-30 respectively. These concentration profiles again revealed the interdiffusion of aluminum and iron atoms across the interface.

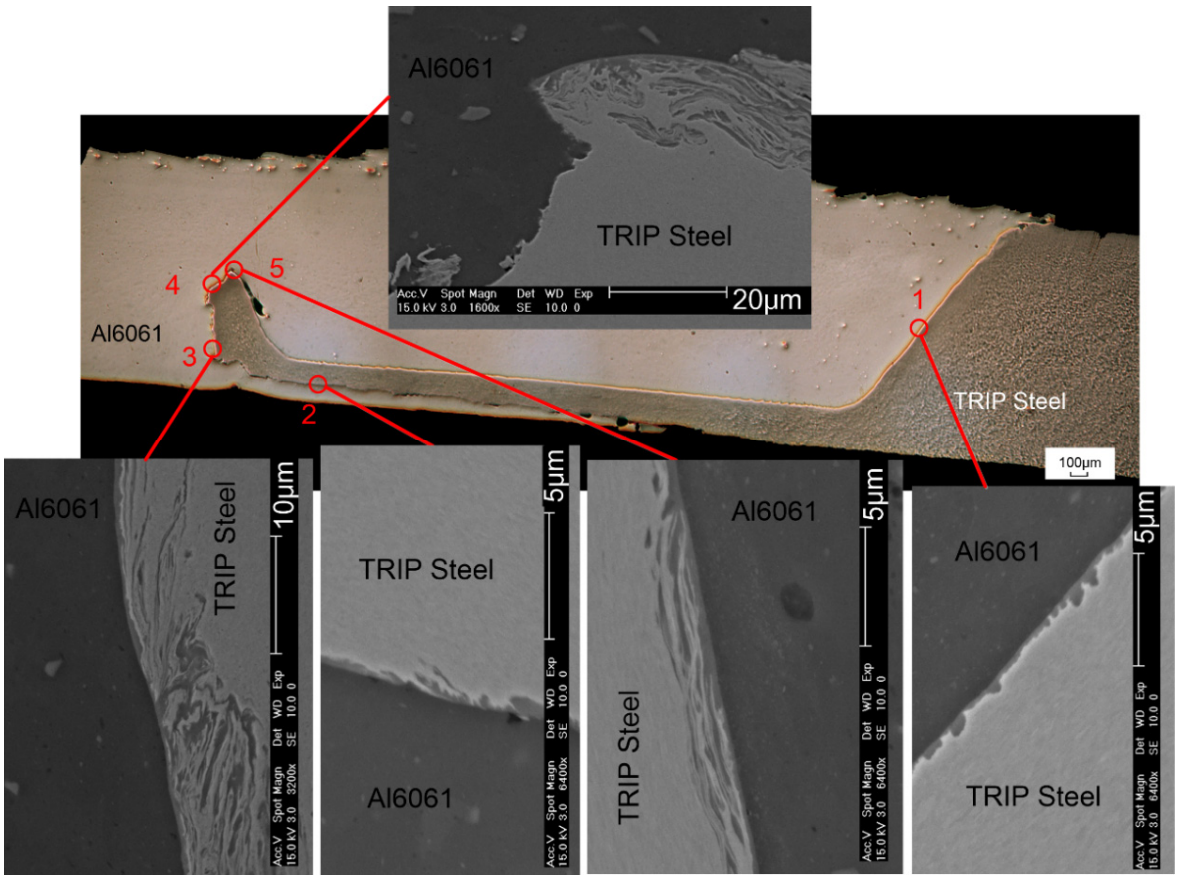

Figure 3-28 Al-Fe interface of the joint section for the necking specimen

Based on the EDS spectrum analysis, atomic percent of aluminum and iron are calculated at the Al-Fe interface and the results are listed in Table 3-4. The atomic ratio between aluminum and

iron is much higher at the tip of the steel strip than that in the advancing side. By comparing the measured atomic ratio at the Al-Fe interface with the atomic ratio of possible Al-Fe intermetallic compounds in the phase diagram, Al_2Fe or $Al_{13}Fe_4$ are likely to exist at the tip of steel strip while Fe_3Al is the more likely intermetallic phase at the advancing side, which is also consistent with the previous results from XRD analysis.

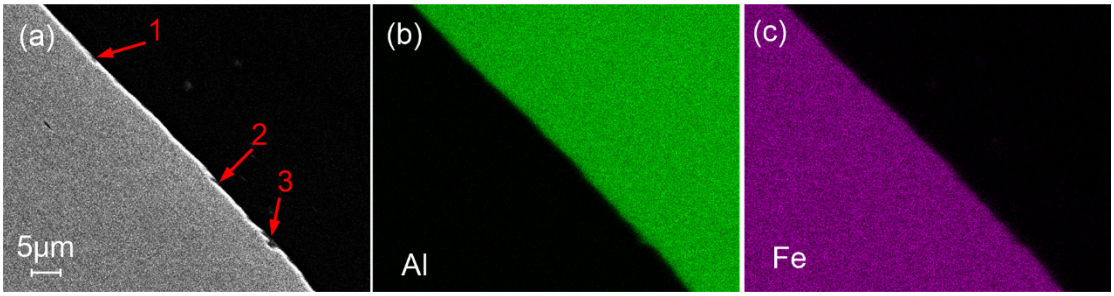

Figure 3-29 Elemental mapping of in the advancing side (Position 1 in Figure 3-28)

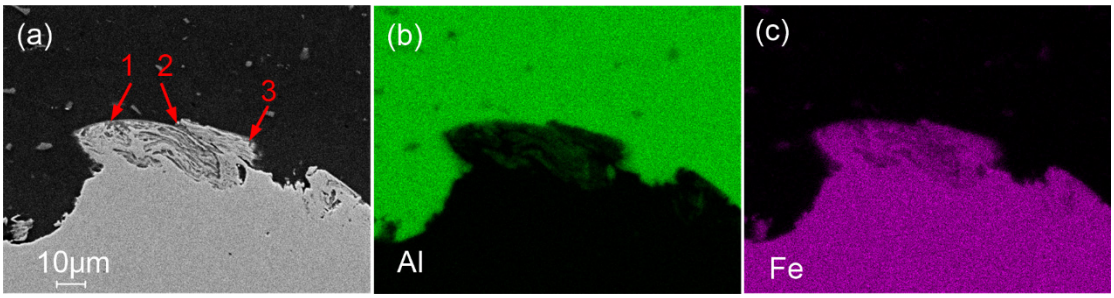

Figure 3-30 Elemental mapping at the tip of the steel strip (position 4 in Figure 3-28)

Table 3-4 Elemental distribution at different locations along Al-Fe interface (at. %)

Position	Tip of steel strip (Position 4 in Figure 3-28)		Advancing side (Position 1 in Figure 3-28)	
	Al	Fe	Al	Fe
1	60.07%	35.41%	24.41%	75.59%
2	76.83%	20.08%	24.70%	73.25%
3	67.66%	30.31%	25.63%	72.12%

A small crack at the inside boundary of steel strip can be noticed in Figure 3-28, which could probably either be induced during the tensile loading or formed during the welding process. In both scenarios, this small crack shows to sustain the tensile loading stress before the actual crack initiated at the heat affected zone of aluminum.

3.3 Summaries and conclusions

In this Chapter, friction stir welding of Al 6061 alloy to TRIP 780 / 800 steel has been experimentally studied under various process conditions. Joint strength and microstructure have been related to the measured mechanical welding force and temperature distribution. Higher rotating speed and larger tool offset can elevate the overall temperature in the weld and reduce the required axial and lateral welding force, which accordingly influence the composition of the formed IMC layer in the advancing side. Under a low rotational speed and small tool offset, FeAl is formed instead of Fe_3Al, which is formed under all other conditions. Welding speed in the studied range has an insignificant effect on mechanical welding force, temperature distribution or material strain rate and is not a sensitive factor for the IMC layer composition. However, higher welding speed can reduce the thermal cycle length and the interlayer thickness. A stirred over steel strip embedded in the aluminum can be observed on the weld cross section. Three failures modes were identified. Except necking and fracture in aluminum side, the other two are related to the outside and inside boundaries of this stirred over steel strip. The Al-Fe adhering interface on the outside boundary of the stirred over steel strip was shown to be the most vulnerable location of the weld.

CHAPTER 4

THERMO-MECHANICAL MODELING ON FRICTION STIR WELDING OF DISSIMILAR MATERIALS

4.1 Literature review

In order to further understand the mechanisms and process physics involved in friction stir welding of Al 6061 to TRIP steel, both analytical and numerical models need to be developed. Current FSW models focus primarily on joining same materials and can generally be categorized into three types: thermal models, thermal-mechanical models based on solid mechanics or fluid mechanics. In thermal modeling works, the heat input was approximated through various methods and applied at the tool workpiece interface for the prediction of the temperature profile [100-104]. Khandkar et al. [105] assumed a uniform shear stress distribution and calculated the heat generation based on the measured torque and machine power. Inverse analysis is another method to determine the heat input and other thermal parameters, including heat transfer coefficient at the workpiece bottom surface [103, 106, 107] and heat partition between tool and workpiece [102]. The calculated temperature distribution can then be applied for residual stress prediction [108] and additional decoupled thermal-mechanical analysis [103, 109].

To further understand the process, including material flow, stress and strain distribution, fully coupled thermal-mechanical models need to be developed. Challenges exist primarily in three aspects: First, the substantial degree of material deformation during plunge stage of FSW can easily cause element distortion and subsequent program divergence. Second, constitutive models for the material mechanical behavior under combined conditions of high temperature, large strain and high strain rate are generally inaccurate [110]. Third, the thermal and mechanical conditions at the tool-workpiece interface and the workpiece-backing plate interface are difficult to define [111, 112].

One group of the coupled thermal-mechanical models is based on solid mechanics theories under Lagrangian formulation, which enables the simulation of the entire FSW process, including plunge, dwell and welding stages. Trimble et al. [82] presented a 3D model based on the finite element package DEFORM to predict axial, translational welding forces and torque during FSW of Al 2024 plates. Johnson-Cook constitutive law was applied and the two aluminum sheets were treated as a whole block. Yu et al. [113] applied the Johnson-Cook material failure model into ABAQUS/Explicit to dynamically remove the over distorted elements. Mandal et al. [114] adopted a pure Lagrangian approach to maintain the mesh integrity and solve for the force and temperature during plunge stage of Al 2024 alloy with ABAQUS/Explicit. Schmidt et al. [115] used the Arbitrary Lagrangian Eulerian (ALE) remeshing technique in ABAQUS and predicted void formation in the weld. Hossfeld et al. [116] used the Couple Eulerian Lagrangian (CEL) method in ABAQUS and modeled the workpiece with Eulerian formulation. Johnson-Cook constitutive law was also used and the model was validated with measured force and torque from experiments. The shape of the plasticized zone and the presence of void correlated well with the experiments. Guerdoux et al. [117] implemented adaptive remeshing in the Forge3 FE software and used

Hansel–Spittel equation as the constitutive model. The condition at tool and workpiece boundary was simulated with the Norton's friction law instead of the classical Coulomb's friction law. Their calculated welding force and torque compared well with experimental results. The surface flash and void formation were also predicted.

The other branch of the coupled thermal-mechanical modeling of FSW is based on Eulerian formulation. Materials are treated as non-Newtonian fluids with high viscosities and flow through the fixed mesh. The fluid model can not consider elastic response of the material and is mainly applicable for steady state welding stage. However, the problem of excessive element distortion can be avoided. Ulysse [118] developed a thermal governing equation and applied a visco-plastic constitutive model to determine the equivalent viscosity. Axial and translational welding forces were then calculated under different welding conditions. Colegrove et al. [119] modeled material flow field and the heat generation associated with a threaded FSW tool in FLUENT. The over predicted temperature was believed to be caused by the non-slip assumption at the tool-workpiece interface as well as inaccurate material model near the solidus temperature. Nandan and Debroy [120-124] derived a series of mechanical and thermal governing equations. The variable of slipping coefficient was additionally introduced to describe slipping condition at the tool-workpiece interface. The value of this parameter was expressed with an empirical exponential relationship based on the distance to the tool center, which further determined the friction coefficient. Heat generation was given by the sum of frictional heat due to slipping and viscous heat due to sticking. A good agreement of the temperature profile was achieved and the material flow field, including strain, strain rate and velocity distribution was analyzed. Liechty and Webb [112] further studied the slipping phenomenon and applied a shear boundary condition at the tool/workpiece interface in FLUENT. The flow field and temperature matched well with

experiment and the maximum material velocity was estimated to be only 9% of the tool rotating speed. Chen et al.[125, 126] also applied a dynamic shear stress boundary at the tool contact area, which revealed an asymmetrical material flow pattern and also significant difference between tool and material velocity. Wang et al. [127] modified the material constitutive model by forcing flow stress to be zero near solidus temperature. They also assumed a constant ratio between the fully sticking area and the entire tool shoulder surface. If the material was outside the prescribed radius, fully slipping condition was assigned. A more reasonable estimate of heat generation was reported based on this approach.

In all the above mentioned analysis, FSW process was studied for joining same material. Limited amount of open literature discussed the modeling of FSW for dissimilar materials. Fratini et al. [128] developed a single block model with DEFORM-3D for joining aluminum alloys AA7175-T73511 to AA2024-T4. Their simulation started with one material and an instantaneous phase transformation was triggered right before the tool plunged into the material. This transformation was then frozen for the rest of computation process and the two materials were therefore treated as two phases of one single material. Material flow and residual stress of the weld were then computed based on this model. Al-Badour et al. [129] employed the CEL algorithm of ABAQUS to simulate FSW of dissimilar Al6061-T6 and Al5083-O aluminum alloys. Control volume approach was applied for analyzing the workpiece region while the tool was modeled as a rigid Lagrangian body. Tool and workpiece interaction was described with Coulomb's friction model and the frictional coefficient was set at 0.8. The model was validated by comparing predicted temperature and material distribution with experimental findings. A featured pin profile was shown to enhance material mixing and reduce volumetric defects based on the analysis from model. Li et al. [130] described the concept of Functionally Graded Material (FGM) and

introduced the parameter of distribution coefficient to model the material field in the weld nugget. The rule of mixture was then adopted for averaging material properties. Simulation of the steady state welding process was conducted in ABAQUS with user defined subroutine DFLUX for modeling the moving heat source. The model was validated through the comparison of residual stress. Idagawa et al. [131] developed a computational fluid dynamics model based on COMSOL for simulating the temperature distribution and thermal history during stable welding stage of Al 6061 and AISI SAE 1020 steel. Their heat generation model was based on studies from Nandan and Debroy [120-124]. However, no material distribution was given.

Few of these literatures discussed the underlying physical principles of FSW of dissimilar materials. Considering the different nature of plunge and welding stages, they will be modeled separately in this chapter. Analytical formulations for each stage are developed first, which are then implemented into corresponding numerical analysis software. Axial welding force, temperature and material distribution are compared with experimental results for model validation.

4.2 Plunge stage study

4.2.1 Analytical formulations

Figure 4-1 shows a schematic illustration of the plunge stage during friction stir welding process. A field variable α is proposed for the identification of the two materials at different regions. The value of α can be assigned to workpiece as a predefined field before the calculation. In this study, α is set to 1 for aluminum and 0 for steel zone. Based on this, one set of governing equations can be applied to both the Al 6061 and TRIP steel bulk regions. As for the interface, local instant formulations of binary phase flow based on the works of Ishii [132, 133] are adopted for developing conservation equations. The whole model is finally completed with thermal and mechanical boundary conditions as well as the workpiece initial states. A general flow chart of the

formulation and computation of the model is shown in Figure 4-2. The feature of steel fragments embedded in the weld nugget is not considered in modeling plunge stage.

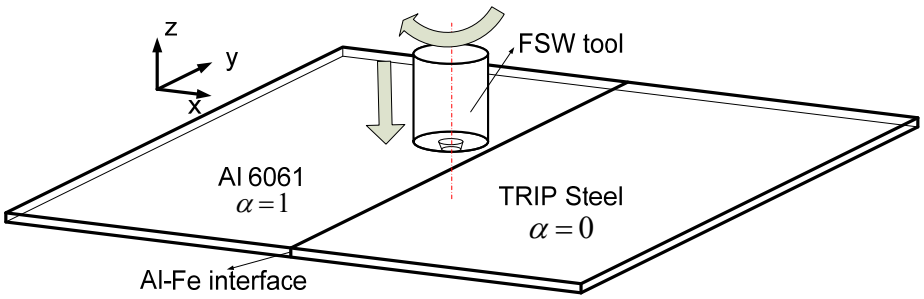

Figure 4-1 Schematic illustration of the material field assignment for plunge stage modeling

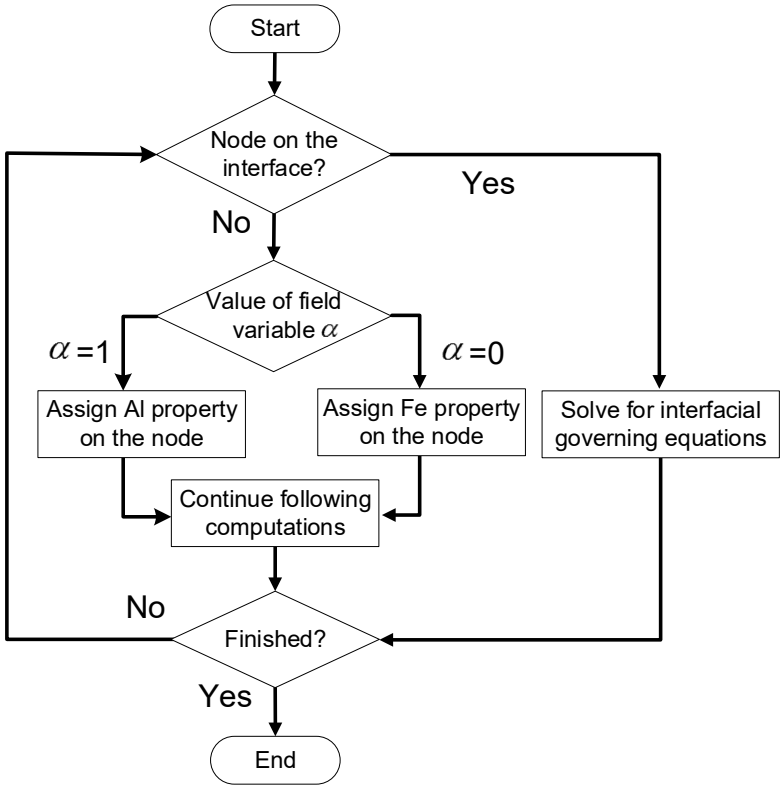

Figure 4-2 General modelling flow chart for plunge stage of FSW of dissimilar materials

4.2.1.1 Governing equations for the bulk material region

The governing equations for bulk material regions are developed based on the works of Ulysse [118] and Debroy et al. [121]. However, there are two major differences between their formulations and the model developed here. Firstly, the models of both Ulysse and Debroy focused on the steady state welding stage, which means all the variables remain constant with regard to time. On the other hand, the transient nature of plunge stage requires the preservation of time dependent terms in the mathematical equations. Accordingly, the conservation equations of mass, momentum and energy are given by:

Mass:
$$\frac{\partial \rho}{\partial t} + \nabla \cdot (\rho \underset{\sim}{v}) = 0 \tag{4-1}$$

Momentum:
$$\frac{\partial \rho \underset{\sim}{v}}{\partial t} + \nabla \cdot \left(\rho \underset{\sim}{v} \underset{\sim}{v} \right) = -\nabla p + \nabla \cdot \underset{\sim}{\Gamma} \tag{4-2}$$

Energy:
$$\frac{\partial \rho c T}{\partial t} + \nabla \cdot \left(\rho c T \underset{\sim}{v} \right) = -\nabla \cdot \underset{\sim}{q} + \nabla \cdot (\underset{\sim}{\sigma} \cdot \underset{\sim}{v}) + \dot{q}_b \tag{4-3}$$

In the mass and momentum equations, ρ is the material density, $\underset{\sim}{v}$ is the velocity field, T is the temperature field, p is the hydrostatic pressure and $\underset{\sim}{\Gamma}$ is the deviatoric stress tensor. The relationship between the hydrostatic pressure, deviatoric stress tensor and the total stress tensor $\underset{\sim}{\sigma}$ is given by:

$$\underset{\sim}{\Gamma} = \underset{\sim}{\sigma} + p\underset{\sim}{I} \tag{4-4}$$

$$p = -\frac{1}{3}\sigma_{ii} \tag{4-5}$$

In this study, the Von-Mises equivalent strain rate is employed and the strain rate tensor is determined from the velocity field:

$$\dot{\varepsilon}_e = \sqrt{\frac{2}{3}\dot{\varepsilon}_{ij}\dot{\varepsilon}_{ij}} \tag{4-6}$$

$$\dot{\varepsilon}_{ij} = \frac{1}{2}\left(\frac{\partial v_i}{\partial x_j} + \frac{\partial v_j}{\partial x_i}\right) \tag{4-7}$$

Regarding material constitutive law, the Johnson-Cook model is applied, which is widely used in modeling FSW [110]. The equivalent stress is determined from equivalent strain, strain rate and temperature by:

$$\sigma_e = [A + B(\varepsilon_e)^n][1 + C\ln(\frac{\dot{\varepsilon}_e}{\dot{\varepsilon}_0})][1 - (\frac{T - T_0}{T_{melt} - T_0})]^m \tag{4-8}$$

where A, B, C, n, m are material parameters and the values can be found from literature.

In the energy conservation equation, $\underset{\sim}{q}$ is the heat flux and can be determined from the temperature gradient according to the Fourier equation:

$$\underset{\sim}{q} = -k(\mathrm{T})\nabla T \tag{4-9}$$

where k is the material thermal conductivity and its value depends on the temperature.

Since there is no external heat input such as resistance or laser heating, the body source term of $\dot{q}_b$ in the energy equation is set to be zero:

$$\dot{q}_b = 0 \tag{4-10}$$

The second difference between the formulations of Ulysse [118], Debroy et al. [121] and the model developed in this study is related to the involved two materials in the weld nugget. In order to account for that, the field variable α is introduced. Generalized material properties are then defined and listed in Table 4-1. With this method, one set of governing equations and constitutive material models is applicable for both materials despite their different physical and mechanical properties. It should be noted that the purpose of field variable α is to mathematically identify the

two materials at different regions, which is different from the purpose of volume fraction. α can only take values of 0 or 1 and the generalized material properties correspond to either steel or aluminum. No averaging is considered in the formulations for plunge stage.

Table 4-1 Generalized material properties defined with field variable α

Material properties	**Expressions**
Density ρ	$\rho = \alpha\rho_{Al} + (1-\alpha)\rho_{Fe}$
Specific heat c	$c = \alpha c_{Al} + (1-\alpha)c_{Fe}$
Thermal conductivity k	$k = \alpha k_{Al} + (1-\alpha)k_{Fe}$
Johnson-Cook constitutive law	$\sigma_e = \alpha[A_{Al} + B_{Al}(\varepsilon_e)^{n_{Al}}][1 + C_{Al}\ln(\frac{\dot{\varepsilon}_e}{\dot{\varepsilon}_0})][1 - (\frac{T - T_0}{T_{meltAl} - T_0})^{m_{Al}}] + (1-\alpha)[A_{Fe} + B_{Fe}(\varepsilon_e)^{n_{Fe}}][1 + C_{Fe}\ln(\frac{\dot{\varepsilon}_e}{\dot{\varepsilon}_0})][1 - (\frac{T - T_0}{T_{meltFe} - T_0})^{m_{Fe}}]$

4.2.1.2 Governing equations for the Al-Fe interface

The conservation equations developed above can hardly be applied to the dissimilar material interface due to the spatial discontinuities. Binary phase flow theories based on the works of Ishii [132, 133] are therefore considered in this study. The interfacial conservation equation for a general quantity ψ is developed first in the integral form and the corresponding control volume V_i is shown in Figure 4-3.

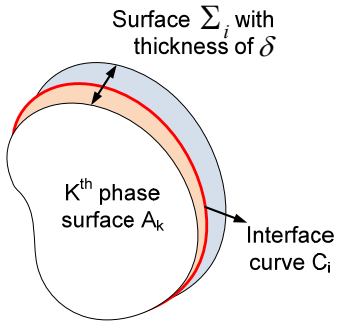

Figure 4-3 Control volume of the Al-Fe interface for conservation equation derivations

The control volume V_i consists of two surfaces A_k in each phase and they are connected by a wall surface Σ_i, which is perpendicular to A_k and has a thickness of δ. In the following derivations, subscript i represents quantities related to interface and subscript k corresponds to quantities in each phase. The intersection between the wall surface Σ_i and the interface of the two materials form a closed curve C_i. $\underset{\sim}{n}_k$ is the outward unit normal vector of surface A_k and $\underset{\sim}{n}$ corresponds to surface Σ_i. The conservation equation for a general quantity ψ can therefore be derived for this control volume:

$$\begin{aligned}\frac{d}{dt}\int_{V_i}\rho\psi dV = &-\sum_{k=1}^{2}\int_{A_k}\underset{\sim}{n}_k\cdot[(\underset{\sim}{v}_k-\underset{\sim}{v}_i)\rho_k\psi_k+\underset{\sim}{j}_k]dA\\ &-\int_{C_i}\int_{-\delta_2}^{\delta_1}\underset{\sim}{n}\cdot[(\underset{\sim}{v}-\underset{\sim}{v}_i)\rho\psi+\underset{\sim}{j}]d\delta dC+\int_{V_i}\rho\phi dV\end{aligned} \tag{4-11}$$

where the left hand side represents the accumulation of the quantity ψ in the control volume. The first term on the right hand side of the equation represents the fluxes of ψ from the surface of each phase. The second term corresponds to the flux from the wall surfaces and the last term describes generation of ψ from the body source. Since the interface of the two phases is not necessarily stationary during the process, moving velocity of the interface has been included in the above equation (4-11) and is denoted as $\underset{\sim}{v}_i$. The flux due to convection is then determined by the relative

velocity of each phase with regard to the interface. In order to transform the conservation equation from the integral form into the differential form, its variables are first integrated and averaged in the thickness direction, which can reduce the volume integration into the surface integration, as shown in the following:

$$\frac{d}{dt}\int_{A_i}\rho_a\psi_s dA = -\sum_{k=1}^{2}\int_{A_k}\underset{\sim}{n}_k\cdot[(\underset{\sim}{v}_k-\underset{\sim}{v}_i)\rho_k\psi_k+\underset{\sim}{j}_k]dA-\int_{C_i}\underset{\sim}{n}\cdot\underset{\sim}{j}_a dC+\int_{A_i}\rho_a\phi_s dV \tag{4-12}$$

where $\rho_a\psi_s$ is the average value of $\rho\psi$ in the thickness direction, as expressed by:

$$\rho_a\psi_s=\int_{-\delta_2}^{\delta_1}\rho\psi d\delta \tag{4-13}$$

Next, the surface transport theorem [134] is applied on the left side term of the equation to move the differential operator into the integrand, as shown in the following:

$$\frac{d}{dt}\int_{A_i}\rho_a\psi_s dA=\int_{A_i}\{\frac{d_s}{dt}(\rho_a\psi_s)+\rho_a\psi_s\nabla_s\cdot\underset{\sim}{v}_i\}dA \tag{4-14}$$

where $\frac{d_s}{dt}$ is the convective derivative with the surface velocity $\underset{\sim}{v}_i$, ∇_s is the surface divergence operator. The term on the left hand side is then in consistent form with almost every term on the right. Furthermore, the line integration term on the right hand side can also be changed into the area integration with the application of surface Green's theorem and associated coordinate transformations [135], as shown in the following:

$$\int_{C_i}\underset{\sim}{n}\cdot\underset{\sim}{j}_a dC=\int_{A_i}\mathrm{A}^{\alpha\beta}\,g_{\ln}(\mathrm{t}^n_\alpha\,\underset{\sim}{j}_a^{l\bullet})_{,\beta}dA \tag{4-15}$$

where $\mathrm{A}^{\alpha\beta}, g_{\ln}$ and t^n_α are relevant metric tensors due to coordinate transformation from Cartesian into a general coordinate system and then into the coordinate system of curved surface for the interface. $(...)_{,\beta}$ is the corresponding differentiation operation in the curved surface coordinate system [136].

After this transformation, every term in equation (4-12) is in surface integral form. The differential form of the governing equation can therefore finally be obtained by removing the integration operator:

$$\frac{d_s}{dt}(\rho_a\psi_s)+\rho_a\psi_s\nabla_s\cdot\underset{\sim}{v}_i=-\sum_{k=1}^{2}\int_{A_k}\underset{\sim}{n}_k\cdot[(\underset{\sim}{v}_k-\underset{\sim}{v}_i)\rho_k\psi_k+\underset{\sim}{j}_k]dA \\ -\mathrm{A}^{\alpha\beta}\,g_{\ln}(\mathrm{t}^n_\alpha\,\underset{\sim}{j}^{l\bullet}_a)_{,\beta}+\rho_a\phi_s \tag{4-16}$$

Based on this general expression, the corresponding conservation equations can be derived by replacing ψ with mass, momentum and energy. Considering the experimental results in chapter 2 that the Al-Fe interface at weld cross section is a relative simple geometry, the metric tensors for coordinate transformation can be set to identity. Since the thickness of the interface is relatively small and generally in the order of microns [137], its associated mass and momentum are assumed to be negligible. Besides, heat generation due to the formation of intermetallics is also not considered for its relatively small magnitude compared with the major thermal effect related to material plastic deformation and friction. Eventually, the three conservation equations can be derived as:

Mass:
$$\sum_{k=1}^{2}\dot{m}_k=\sum_{k=1}^{2}\rho_k\underset{\sim}{n}_k\cdot(\underset{\sim}{v}_k-\underset{\sim}{v}_i)=0 \tag{4-17}$$

Momentum:
$$\sum_{k=1}^{2}\{\rho_k\underset{\sim}{n}_k\cdot(\underset{\sim}{v}_k-\underset{\sim}{v}_i)\underset{\sim}{v}_k-\underset{\sim}{n}_k\cdot\underset{\sim}{\sigma}_k\}+\nabla\gamma=0 \tag{4-18}$$

Energy:
$$\sum_{k=1}^{2}\{\rho_k\underset{\sim}{n}_k\cdot(\underset{\sim}{v}_k-\underset{\sim}{v}_i)c_{vk}T_k+\underset{\sim}{n}_k\cdot(-\underset{\sim}{\sigma}_k\cdot\underset{\sim}{v}_k+\underset{\sim}{q}_k)\} \\ +\nabla\cdot(\gamma\underset{\sim}{v}_i)=\frac{d_s e_a}{dt}+e_a\nabla_s\cdot\underset{\sim}{v}_i \tag{4-19}$$

In the momentum equation, $\underset{\sim}{\sigma}_k$ is the stress tensor in each phase at the interface boundary. γ is the interfacial tension between the two materials, which is a function of temperature.

According to Girifalco and Good [138], the interfacial tension between two materials can be approximated by the surface tension of each material based on the following equation:

$$\gamma_{12}(\mathrm{T}) = \gamma_1(\mathrm{T}) + \gamma_2(\mathrm{T}) - 2\Phi\sqrt{\gamma_1(\mathrm{T})\gamma_2(\mathrm{T})} \tag{4-20}$$

where Φ is a parameter depending on different binary systems and varies around the regular value of 1 [138]. The surface tension for aluminum and steel at different temperatures can be found from literature and listed in Table 4-2.

Table 4-2 Surface tension for aluminum and steel at different temperatures

Surface tension (Unit: N/m)	Value	References
Aluminum	0.737	[139]
Steel	1.84 - 0.0004(T - 1823)	[140]

In the energy conservation equation, c_{vk}, T_k, $\underset{\sim}{q}_k$ are the heat capacity, temperature and heat flux of each phase at the interface boundary, which can be calculated from the previous section for the bulk material region. e_a is the interfacial energy, which can similarly be determined by the surface energy of each phase through the following equation [138]:

$$e_{12}(\mathrm{T}) = e_1(\mathrm{T}) + e_2(\mathrm{T}) - 2\Phi\sqrt{e_1(\mathrm{T})e_2(\mathrm{T})} \tag{4-21}$$

4.2.1.3 Boundary conditions

Boundary conditions are considered at three contact surfaces, i.e., workpiece/tool, workpiece/backing plate and the interface of the two materials. The friction between workpiece and tool will provide a heat flux as a thermal boundary condition and can be calculated based on the following equation:

$$d\dot{q}_{bf} = f_h v_T \mu_f p dA \tag{4-22}$$

where v_T is the magnitude of the tool velocity determined from the combined motion of plunge and rotation. p is the pressure component of the total stress tensor at the corresponding contact positions, which can be determined based on equation (4-4). μ_f is the frictional coefficient and is set at a constant value of 0.3. This is typical of what has been published in the literature [111, 141]. Besides, it also results in the best match between numerical calculated force and experimental measurement. The generated frictional heat will be partitioned between tool and workpiece and the partition coefficient f_h can be determined by [121]:

$$\begin{aligned} f_h = \alpha \frac{\left(k_{Al}\rho_{Al}c_{Al}\right)^{\frac{1}{2}}}{\left(k_T\rho_T c_T\right)^{\frac{1}{2}} + \left(k_{Al}\rho_{Al}c_{Al}\right)^{\frac{1}{2}}} \\ +(1-\alpha)\frac{\left(k_{Fe}\rho_{Fe}c_{Fe}\right)^{\frac{1}{2}}}{\left(k_T\rho_T c_T\right)^{\frac{1}{2}} + \left(k_{Fe}\rho_{Fe}c_{Fe}\right)^{\frac{1}{2}}} \end{aligned} \tag{4-23}$$

where α is the field variable for identification of specific material at different positions as described in the previous section. Subscript *T* stands for material properties for the FSW tool.

The thermal boundary condition at the workpiece bottom surface is basically the heat transfer into the backing plate. The heat conducted from workpiece into the backing plate is equal to the *z*-component of the heat flux in the workpiece at its bottom surface. This amount of heat will increase the internal energy of the backing plate, which can be approximated by multiplying its heat capacity with the temperature change. The relationships are given by the following equation, where subscript b represents properties of the backing plate:

$$
\begin{aligned}
q_z\left(z=0\right) &= k\left.\frac{\partial T}{\partial z}\right|_{z=0} \\
&= \left[\alpha h_{Al} + (1-\alpha)h_{Fe}\right]\left(T - T_b\right) \\
&= c_b m_b \left(T_b - T_{b0}\right)
\end{aligned}
\tag{4-24}
$$

Regarding the interface of the two materials, temperature equilibrium and non-slip conditions are assumed [133], as expressed by:

$$T_1 = T_2 \tag{4-25}$$

$$\underline{v}_{t1} = \underline{v}_{t2} \tag{4-26}$$

Finally, the thermal boundary condition at the remaining surface of the workpiece is considered from the aspect of heat transfer into the environment, which is given by the following equation. The field variable α is also included to account for the different transfer coefficients in aluminum and steel regions and T_a is the ambient temperature:

$$q_a = k\left|\nabla T\right|_{Boundary} = \left[\alpha h_{Al} + (1-\alpha)h_{Fe}\right]\left(T - T_a\right) \tag{4-27}$$

4.2.2 Numerical implementation in ABAQUS

An overview of the finite element model is shown in Figure 4-4, which is developed based on the ABAQUS/Explicit program. According to the temperature measurement results from preliminary experiments, temperature increase on the top surface of workpiece is negligible at points located 25mm away from the weldline. To reduce the computational scale, only the central part of the workpiece with the total dimensions of 50mm x 50mm x 1.4mm is modeled in the FEA analysis. The mesh is graded such that the element distribution is refined in the plunge area, especially at the Al-Fe interface, the region near the periphery of the pin and the bottom region of the workpiece. Besides, since the tool is shifted to aluminum, the mesh in the aluminum side is also generally finer than that in steel side. A total of 133518 elements are meshed on the workpiece

and the element type is C3D8RT. Average size of the elements in the center of the workpiece near the bottom surface is around 0.05x0.05x0.05 mm. Parameters of the Johnson-Cook constitutive model for Al 6061 and TRIP steel are listed in Table 4-3 and other physical properties are listed in Table 4-4. Dirichlet boundary conditions are applied at the lateral surfaces of the workpiece, where all the displacement degrees of freedom are fixed. These fixed boundaries are approximately located at the same clamping positions of the workpiece during experiments. Initial temperature of the workpiece is set at room temperature.

The tool is modeled as rigid body with the thermal degree of freedom. Geometry of the tool is the same as the tool used during the FSW experiments, as described in Chapter 3. Plunge speed of 10 mm/min is assigned on the tool and the plunge depth is set at 1.3mm, both of which are the same as the experimental configurations described in Chapter 3. Two tool offset conditions, 1.63mm and 1.03mm, are numerically investigated under the same tool rotational speed of 1200rpm.

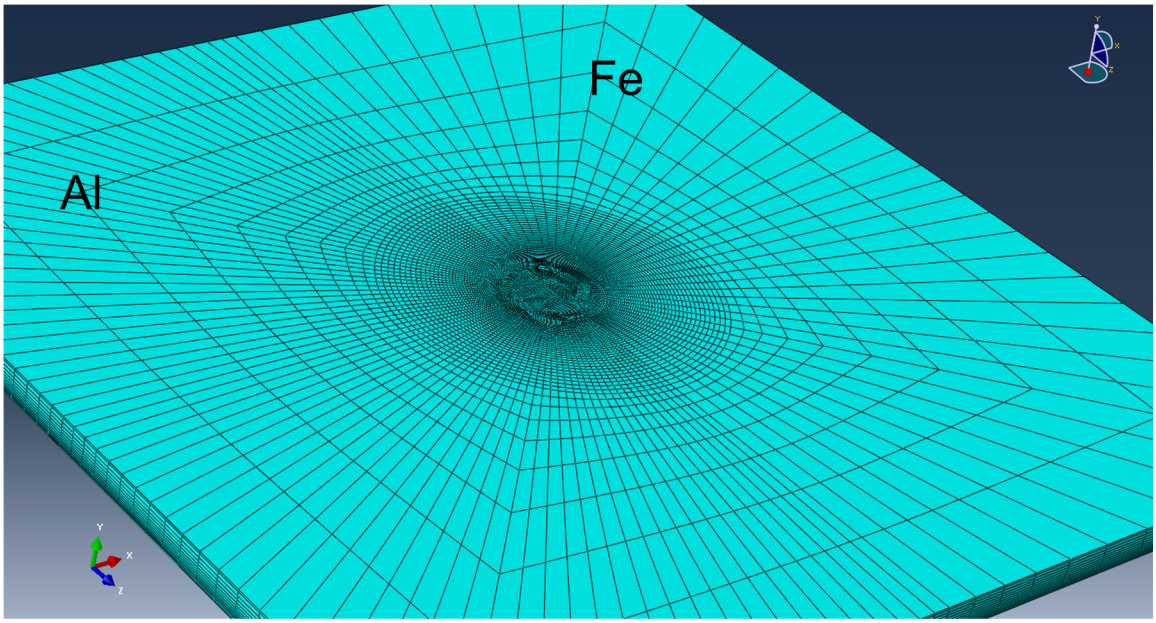

Figure 4-4 Overview of the mesh on the workpiece

Table 4-3 Material parameters in Johnson-Cook models for Al 6061 and TRIP 780 steel

Material	A	B	n	C	m	T_m (K)
Al 6061 [142]	245	121	0.23	0.002	1.34	855
TRIP 780 [143]	780	1429	0.79	0.014	0.76	1673

Table 4-4 Physical properties of Al 6061 and TRIP 780 steel

Material	Density (kg/m^3)	Thermal conductivity (W/m-K)	Specific heat (J/Kg-K)	Thermal expansion (μm/K)
Al 6061 [84]	2667	210	1100	28
TRIP 780 [120, 124]	7860	60	500	10

4.2.3 Results and discussion

Different values of friction coefficients at tool-workpiece interface are investigated in the initial numerical analysis. In the condition with tool offset of 1.03mm, the friction coefficient of 0.3 yields the best agreement between the experimental measurements and numerical calculations on the axial plunge force, as shown in Figure 4-5. The force increases in the beginning, reaches a short plateau and then increases again till the final plunge depth. The force reduces a little after the final peak, which is related to the dwell stage where the tool is held rotating at the same position without further moving into the workpiece. In the experimental measurements, the force finally drops down, which is due to the retraction of the tool and this stage is not included in the numerical analysis. However, discrepancies between the measured and calculated force curves exist in two regions. First is in the beginning of the plunge action, where the predicted force increases much faster than experimental observations. One possible reason is related to the transition from elastic deformation to plastic deformation. During experiments, the stiffness of the workpiece is actually the equivalent stiffness of the entire experimental system, including the machine itself and the fixtures below the workpiece. On the other hand, during simulation the elastic deformation can

only come from the workpiece material, which induces plastic deformation to occur at an earlier stage and increases the axial force faster.

Second, in the final stage, the numerical result over-estimates the axial force compared with experimental results. This deviation contains both numerical and experimental sources. From the numerical perspective, the material mechanical behaviors approximated by Johnson-Cook constitutive model predicts a much higher flow stress particularly at large plastic strains, where the actual material might already fail and the flow stress reduces significantly. From the experimental perspective, under the severe shear action of the tool, certain amount of materials was peeled off and formed chips around the tool. Falling out of these material chips from the plunge zone was observed during experiments, which reduced the axial force to plunge the tool further into the workpiece.

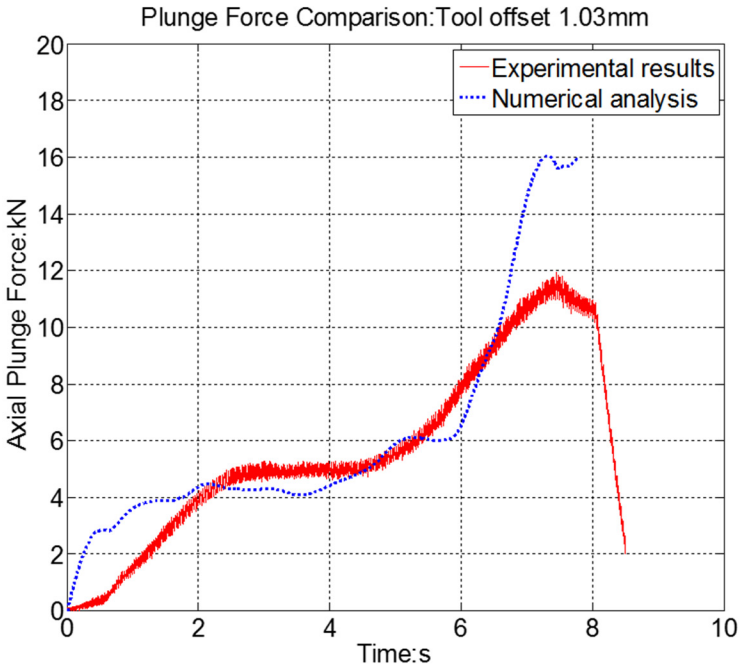

Figure 4-5 Comparison of axial plunge force between experimental and numerical results with tool offset of 1.03mm

Figure 4-6 compares the axial plunge force between the experimental and numerical results in a larger tool offset condition of 1.63mm. Overall, the simulated force curve also agrees well with experimental measurements, except in the beginning and final parts, which is similar to the smaller tool offset condition. The overestimated axial force was also reported by Mandal et al. in their studies [114]. Comparing these two conditions of different tool offsets, the numerical analysis reveals a higher axial force under smaller the tool offset condition, where the tool is less shifted to aluminum side and more amount of steel is deformed in the weld zone. This result is also consistent with the experimental observations.

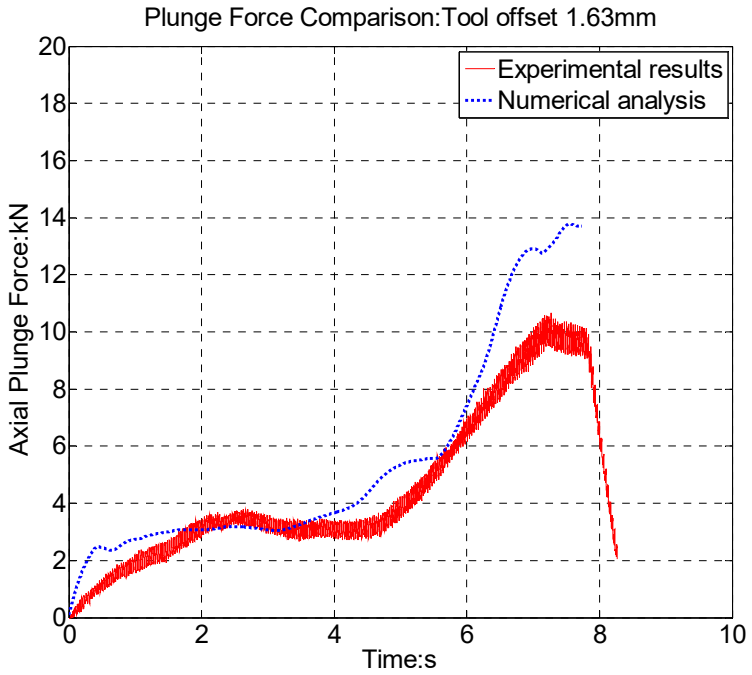

Figure 4-6 Comparison of axial plunge force between experimental and numerical results with tool offset of 1.63mm

Figure 4-7 shows the material distribution at different plunge depths with tool offset of 1.03mm. The cross section is placed in the center of the FSW tool and perpendicular to the abutting edge of the two materials. As the tool moves downward, steel material below the end surface of the pin is squeezed into aluminum side. In the meantime, certain amount of aluminum is stirred

over from the rotating action of the pin and pushed towards steel in the periphery of the pin. At the end of the plunge stage, a fraction of steel is embedded in the aluminum side in the bottom region of the workpiece, which shows resemblance to the macrostructure of the cross sections from a continuous weld, as shown in Chapter 3.

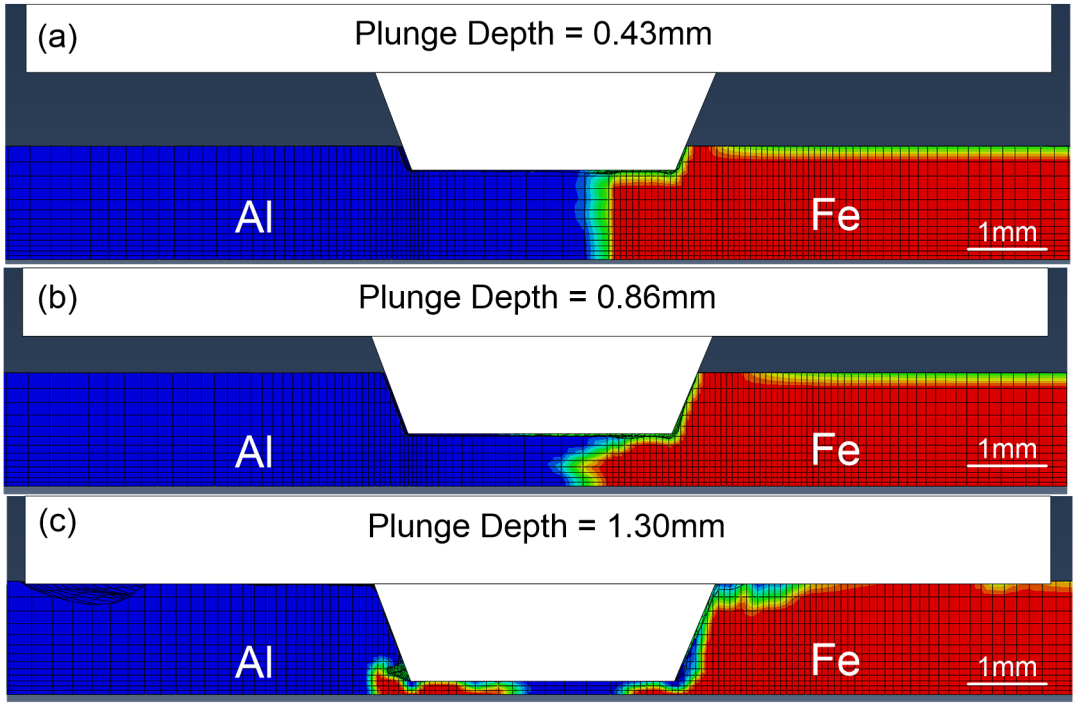

Figure 4-7 Material distribution at different plunge depths under tool offset of 1.03mm

Figure 4-8 shows the material distribution at different planes below the workpiece top surface. The *z* value is zero at weld top surface and more negative as the plane approaches weld bottom surface. In front of the pin, aluminum is stirred towards steel due to the rotation motion. At the back, steel is extruded into aluminum matrix.

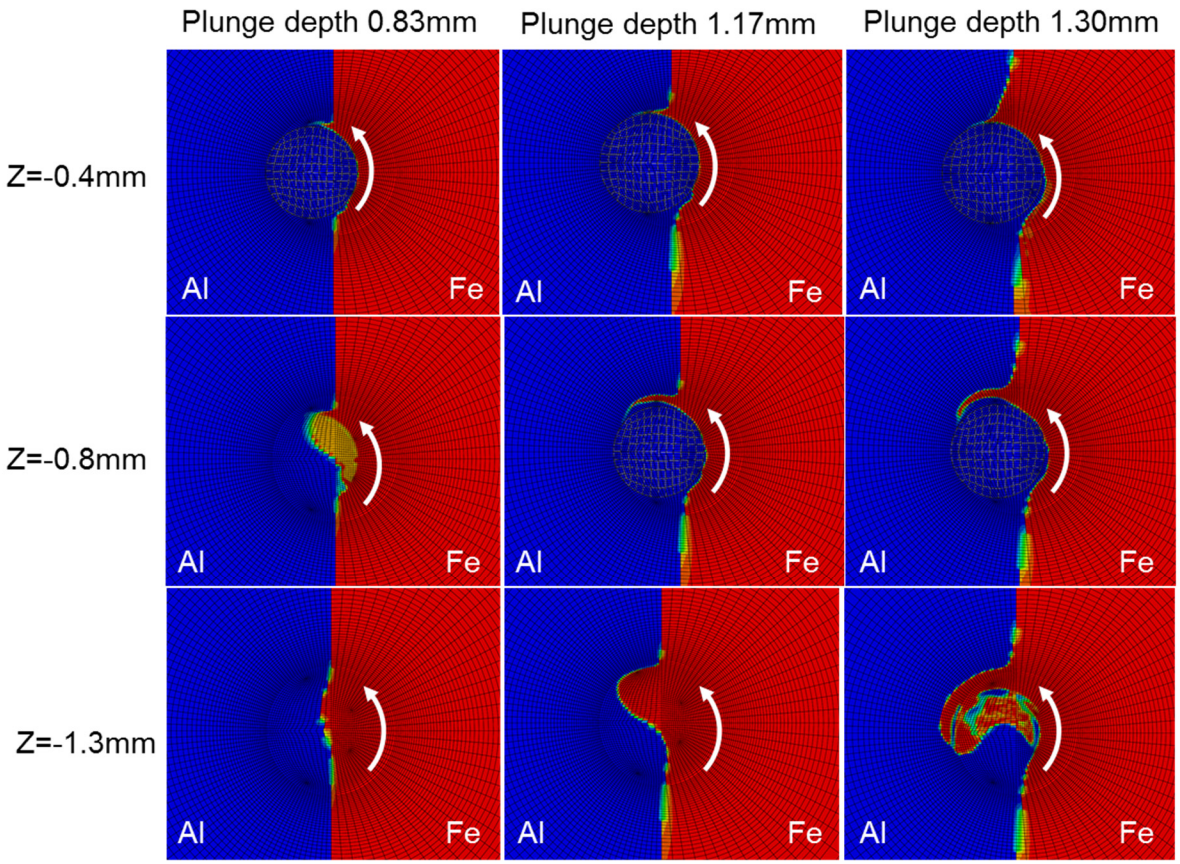

Figure 4-8 Material distribution at different planes below workpiece top surface (Tool offset: 1.03mm)

In the condition of a larger tool offset condition of 1.63mm, material distribution at the cross section perpendicular to weld top surface is shown in Figure 4-9. Similarly, as the tool moves downward, certain amount of aluminum is stirred over and pushed into steel side in the periphery of the pin. This results in a larger inclination angle of Al-Fe interface compared with the cone angle of the pin, which is similar to the experimental observations of weld cross section. On the other hand, since the fraction of steel in the stirring zone is relatively small, steel is only slightly squeezed towards the aluminum side near the bottom surface and cannot flow into the aluminum region. The corresponding material distribution at different planes below weld top surface is shown in Figure 4-10.

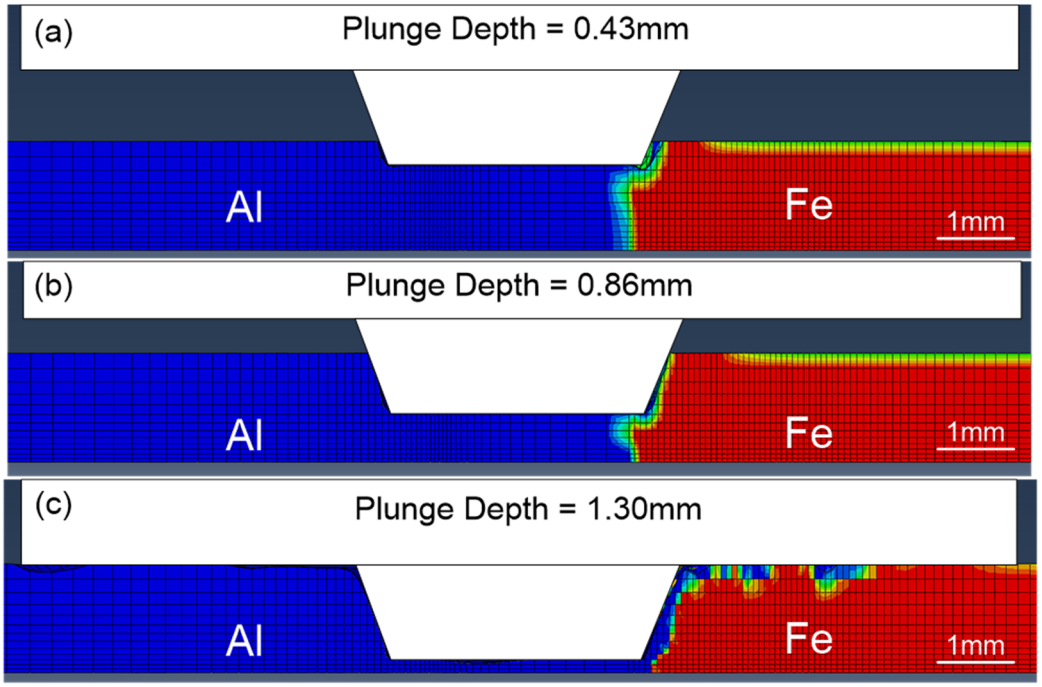

Figure 4-9 Material distribution at different plunge depths under tool offset of 1.63mm

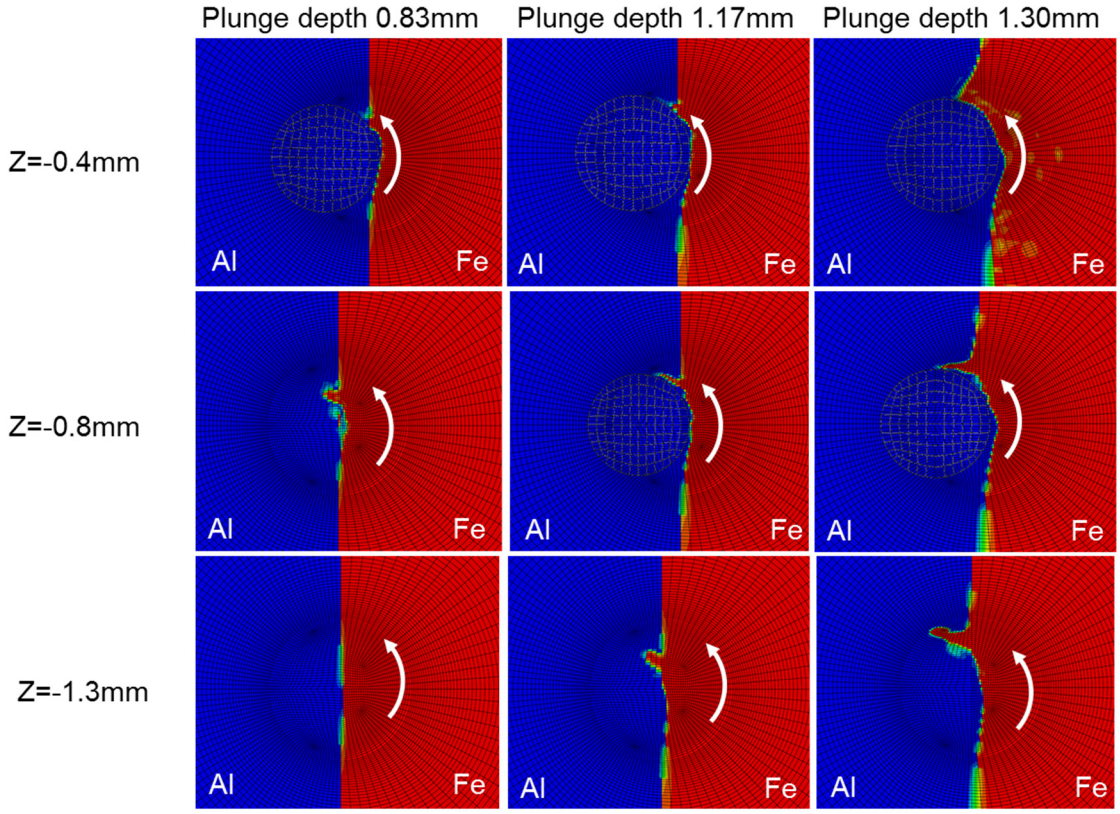

Figure 4-10 Material distribution at different planes below workpiece top surface (Tool offset: 1.03mm)

4.3 Welding stage study

4.3.1 Analytical formulations

4.3.1.1 Assumptions

The steady state welding stage is modeled in the Eulerian formulation, where materials flow into the computational domain with the prescribed welding speed while the tool stays at the same location with only the rotational motion. Solid state metals are treated as non-Newtonian fluids with high viscosities. Accordingly the flow field belongs to laminar regime and the viscosity is a function of temperature and strain rate. Aluminum and steel are treated as different phases. Based on the topology of phase distribution, multiple phase flow can be categorized into two general groups: separated flow and dispersed flow. In the former one, different phases are continuous and separated by a clearly-defined interface. The latter group corresponds to flow of discrete phases, such as bubbles, droplets and particles, in a continuous primary phase. According to experimental observations of weld cross section macrostructure in Chapter 3, both aluminum and steel are basically continuous. Only a small amount of steel or intermetallic compound particles are dispersed in the aluminum matrix. However, the quantity and sizes of these particles are small, which are neglected in the current model for simplification. The dissimilar FSW process is therefore modeled as a separated multiple phase flow problem.

Regarding the interfacial tension between the two phases, its significance can be evaluated based on the value of the Capillary number Ca, which is defined by:

$$Ca = \frac{\mu U}{\gamma_{st}} \tag{4-28}$$

where μ is the viscosity, γ_{st} is the surface tension and U is the free stream velocity, which can be approximated as the welding speed. For steel and aluminum near their melting temperature, γ_{st} is

generally in the order of 1 N/m [144-146]. The equivalent viscosity for aluminum and steel near the weld zone of FSW, which will be discussed in the following session, can be calculated to be in the order of 10^6 Pa·s. Accordingly, the Capillary number is much larger than 1, which indicates that the effect of interfacial tension is insignificant compared with that of the high viscous flow stress of materials [147]. The interfacial tension is therefore neglected in the welding stage model. Regarding intermetallic compound formed at Al-Fe interface, the thickness of this layer is only around 1 μm according to the experimental results in Chapter 3. Therefore, generation and corresponding influence of intermetallic compounds are also not considered to reduce computational complexity and improve numerical convergence.

4.3.1.2 Governing equations

The most critical parameter for mechanical properties of fluid is the viscosity. According to its definition, viscosity is given by the shear stress divided by the shear strain rate:

$$\mu = \frac{\tau}{\dot{\gamma}} \tag{4-29}$$

On the other hand, material constitutive laws are generally obtained from uniaxial tensile tests and the equation is given by effective normal stress and strain. In order to establish the relationship between shear stress and strain with the effective normal stress and strain, a pure shear stress state is considered. The corresponding principal stresses and principal strains are:

$$\sigma_1 = \tau\,, \sigma_2 = -\tau\,, \sigma_3 = 0 \tag{4-30}$$

$$\varepsilon_1 = \frac{\gamma}{2}\,, \varepsilon_2 = -\frac{\gamma}{2}\,, \varepsilon_3 = 0 \tag{4-31}$$

Accordingly, the von Mises effective normal stress can be determined based on the following equation:

$$\sigma_e = \sqrt{\frac{1}{2}\left[\left(\sigma_1 - \sigma_2\right)^2 + \left(\sigma_2 - \sigma_3\right)^2 + \left(\sigma_3 - \sigma_1\right)^2\right]} = \sqrt{3}\tau \tag{4-32}$$

$$\varepsilon_e = \sqrt{\frac{2}{9}\left[\left(\varepsilon_1 - \varepsilon_2\right)^2 + \left(\varepsilon_2 - \varepsilon_3\right)^2 + \left(\varepsilon_3 - \varepsilon_1\right)^2\right]} = \frac{1}{\sqrt{3}}\gamma \tag{4-33}$$

Therefore, the equivalent viscosity can then be given by the effective normal stress and effective normal strain rate with the following relationship:

$$\mu = \frac{\sigma_e}{3\dot{\varepsilon}_e} \tag{4-34}$$

The same relationship was also reported in [118, 121]. During friction stir welding, materials are subject to combined conditions of severe plastic deformation, high strain rate and temperature. The material constitutive model developed by Sheppard and Wright [148], which takes into consideration the dynamic recovery and recrystallization process, is employed in this study:

$$\sigma_e = \frac{1}{\beta}\ln\left\{\left(\frac{Z}{A}\right)^{(1/n)} + \left[\left(\frac{Z}{A}\right)^{(2/n)} + 1\right]^{1/2}\right\} \tag{4-35}$$

where Z is the Zener Hollomon Parameter, which depends on temperature and strain rate as the following equation:

$$Z = \dot{\varepsilon}_e \exp\left(\frac{Q_{def}}{RT}\right) \tag{4-36}$$

As described in the assumptions, the dissimilar FSW process belongs to separated multiple phase flow category and the two materials are not interpenetrating to each other. One of the prevalent methods for solving this type of problems is the volume of fluid (VOF). In this method, another spatially continuous variable α_k for volume fraction of phase k is introduced for describing phase distribution. Velocity $\underset{\sim}{v}$, temperature T and pressure p fields are shared among different phases. Material properties are averaged based on the volume fraction α_k in each unit

cell. Corresponding conservation equations of mass, momentum and energy can therefore be derived as [147]:

Mass: $$\underset{\sim}{\nabla}\cdot(\alpha_k\rho_k\underset{\sim}{v})=\sum_{k=1}^{2}\left(\dot{m}_{jk}-\dot{m}_{kj}\right) \tag{4-37}$$

Momentum: $$\underset{\sim}{\nabla}\cdot(\bar{\rho}\underset{\sim}{v}\,\underset{\sim}{v})=-\underset{\sim}{\nabla}p+\underset{\sim}{\nabla}\cdot\bar{\underset{\sim}{\Gamma}} \tag{4-38}$$

Energy: $$\underset{\sim}{\nabla}\cdot\left[\left(\Sigma\alpha_k\rho_k c_k\right)T\underset{\sim}{v}\right]=-\underset{\sim}{\nabla}\cdot\underset{\sim}{q}+\underset{\sim}{\nabla}\cdot\left[(\bar{\underset{\sim}{\Gamma}}-p\underline{I})\cdot\underset{\sim}{v}\right]+\dot{q}_b \tag{4-39}$$

where $\underset{\sim}{\nabla}$ is the vector differential operator and is given by:

$$\underset{\sim}{\nabla}=\frac{\partial}{\partial x}\underset{\sim}{i}+\frac{\partial}{\partial y}\underset{\sim}{j}+\frac{\partial}{\partial z}\underset{\sim}{k} \tag{4-40}$$

The mass conservation equation is basically for determining the volume fraction of different phases in each Eulerian element, which accordingly tracks the position of Al-Fe interface. Since there are only two phases involved, only the volume fraction of either aluminum or steel needs to be computed. The remaining one can then be determined based on the fact that the sum needs to be unity.

In the momentum governing equation, $\bar{\rho}$ is the material density averaged by volume fraction, as given by:

$$\bar{\rho}=\sum_{k=1}^{2}\alpha_k\rho_k \tag{4-41}$$

$\bar{\underset{\sim}{\Gamma}}$ is the shear stress tensor, which can be calculated by the velocity gradient and averaged viscosity:

$$\bar{\underset{\sim}{\Gamma}}=\bar{\mu}\left(\underset{\sim}{\nabla}\otimes\underset{\sim}{v}+\underset{\sim}{\nabla}\otimes\underset{\sim}{v}^{T}\right) \tag{4-42}$$

$$\bar{\mu}=\sum_{k=1}^{2}\alpha_k\mu_k \tag{4-43}$$

where viscosity of each phase can be determined based on equation (4-34) and symbol $\otimes$ represents the tensor product operation.

In the energy equation, heat flux $\overline{\underset{\sim}{q}}$ is given by temperature gradient and average thermal conductivity as the following:

$$\overline{\underset{\sim}{q}} = -\overline{K}\nabla T \text{, where } \overline{K}=\sum_{k=1}^{2}\alpha_k K_k \tag{4-44}$$

Regarding the body heat source, since there are no external energy supplies, such as resistance or laser heating, $\dot{q}_b$ is set to be zero. The viscous heating due to plastic deformation is already included in the energy equation (4-39).

4.3.1.3 Boundary conditions

To complete the model, appropriate boundary conditions need to be established. The most critical one is for the coupled thermal-mechanical interface between workpiece and tool. From mechanical aspect, FSW tool exerts a rotation motion onto the material and a partial sliding/sticking condition occurred at the contact area. To describe this interaction, there are generally two approaches. In the first approach, a constant rotating velocity is imposed onto the material, which can be either the tool rotating speed, i.e., non-slip condition, or a constant ratio of the tool rotating speed [118]. In the second approach, a frictional shear stress is applied in the same direction as the tangential velocity of the tool. Material velocity is then determined by the relative magnitude of applied frictional stress and material viscous flow stress [112]. In this study, first a constant rotating velocity boundary is investigated. Based on literature [112, 118], a non-slip condition would predict a much higher temperature. Considering the strong deformation resistance of steel, a high slipping rate between material and the tool is anticipated. Therefore, the material

velocity is tentatively assumed to be only 10% of that of the tool in the initial investigation of the constant rotating velocity boundary condition. After that, a shear stress boundary condition is applied. The empirical friction model developed by Maekawa et al. [149, 150] for describing tool-chip interfacial condition during machining process is employed, which is given by:

$$\tau_b = m\tau_e \left\{ 1 - \exp\left[-\left(\frac{\mu_f p}{m\tau_e} \right) \right]^n \right\}^{\frac{1}{n}} \tag{4-45}$$

where τ_e is the equivalent shear flow stress of the stirred material and can be calculated according to the equivalent material flow stress from equation (4-32). p is the local pressure. μ_f is the frictional coefficient. m is the friction factor and n is the sensitivity factor, both of which are material related constants.

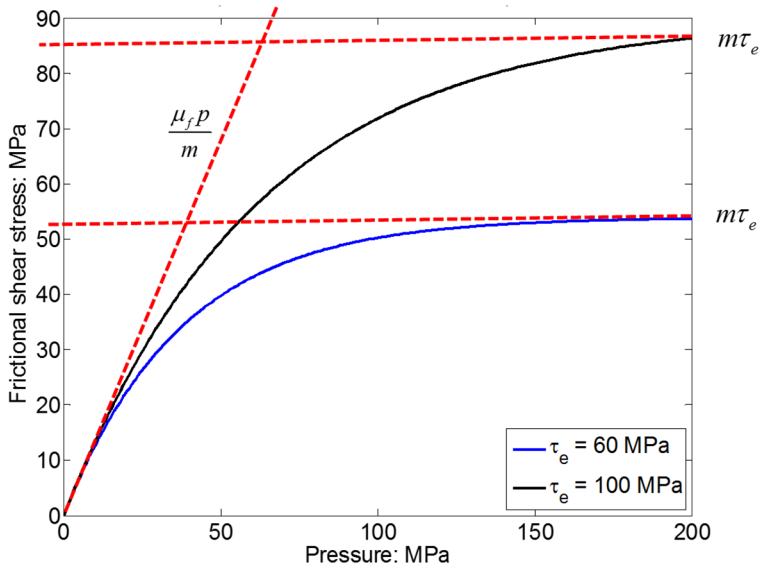

Figure 4-11 Relationship between frictional shear stress and pressure for TRIP steel

Figure 4-11 shows the relationship between frictional shear stress and pressure according to equation (4-45) for steel. If the pressure is relatively low compared with the material flow stress, the friction law basically follows the Coulomb's model and the frictional stress is linearly

proportional to the pressure. This represents the slipping condition. If the pressure is relatively high compared with the material flow stress, the frictional stress then approaches the material flow stress with a correction factor, which represents the sticking condition. This friction model therefore can capture both slipping and sticking conditions. The dominant condition depends on the relative magnitude of material flow stress and the applied pressure.

In the thermal aspect, the amount of heat input at the tool contacting area is a summation of frictional heat from aluminum and steel based on their relative volume fractions. The heat can be calculated as:

$$\overline{q}_{tool} = \left(f_h^{Al} \alpha_{Al} \tau_b^{Al} + f_h^{Fe} \alpha_{Fe} \tau_b^{Fe} \right) \left| \underset{\sim}{v} - \underset{\sim}{v}_{tool} \right| \tag{4-46}$$

where $\underset{\sim}{v}$ is the calculated material velocity and $\underset{\sim}{v}_{tool}$ is the assigned tool velocity based on the rotating speed and radius. f_h^{Al} and f_h^{Fe} are the heat partition coefficients between tool and workpiece for aluminum and steel respectively, which can be determined from the followings [121]:

$$f_h^{Al} = \frac{\left(k_{Al} \rho_{Al} c_{Al} \right)^{\frac{1}{2}}}{\left(k_T \rho_T c_T \right)^{\frac{1}{2}} + \left(k_{Al} \rho_{Al} c_{Al} \right)^{\frac{1}{2}}} \tag{4-47}$$

$$f_h^{Fe} = \frac{\left(k_{Fe} \rho_{Fe} c_{Fe} \right)^{\frac{1}{2}}}{\left(k_T \rho_T c_T \right)^{\frac{1}{2}} + \left(k_{Fe} \rho_{Fe} c_{Fe} \right)^{\frac{1}{2}}} \tag{4-48}$$

where subscript T represents physical properties of the FSW tool.

The thermal boundary condition between backing plate and workpiece is simplified as equation (4-49). The amount of heat loss through conduction is approximated as the product of heat transfer coefficient and the temperature difference between the workpiece bottom surface and the backing plate:

$$\overline{q}_b = \left[\alpha_{Al} h_{Al} + \alpha_{Fe} h_{Fe}\right]\left(T - T_b\right) \tag{4-49}$$

Heat dissipation from the top surface of the workpiece to the environment is also expressed with the same equation as (4-49), where the heat transfer coefficients take a smaller value. Side surfaces of the workpiece are set at constant room temperature considering the large heat dissipation from workpiece into the clamping fixtures during experiments.

4.3.2 Numerical implementations

The geometry of the FSW tool is represented as a hole in the computation domain of the workpiece, as shown in Figure 4-12. The 0.1mm plunge depth of tool shoulder is also included and tool geometry is the same as the experimental configuration in Chapter 3. Structured mesh is generated from the ICEM software to improve calculation accuracy and efficiency. Considering the complex interactions between tool and workpiece as well as interfacial conditions between the two materials, the mesh is greatly refined adjacent to the tool region and original interface of the two materials, as shown in Figure 4-13. The entire workpiece, which has a length of 110mm in the welding direction, width of 100mm and thickness of 1.4mm, contains a total number of 654480 elements.

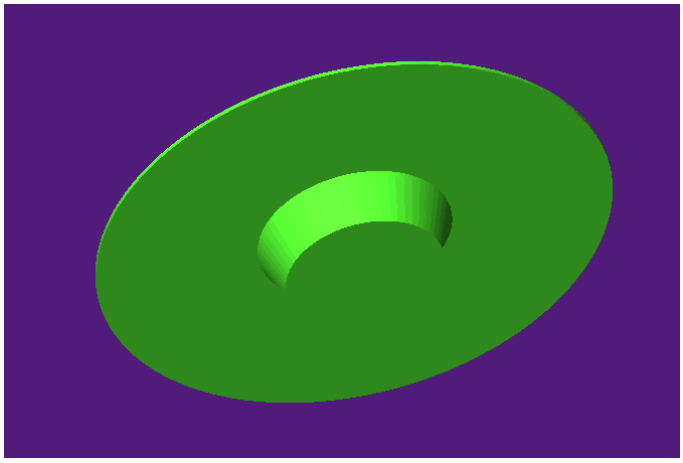

Figure 4-12 Workpiece computational domain where tool geometry and the shoulder plunge depth are carved out

Related equations in the analytical analysis in the previous session are written in user-defined functions (UDF) and implemented into the FLUENT software. The parameter of tool offset described in the experimental configuration in Chapter 3, is incorporated into the model through assigning distribution of the materials as they flow into the computation domain. Corresponding parameters in the material constitutive relationships of Al 6061 and TRIP steel are listed in Table 4-5. Besides, values of material constants for the friction model are given in Table 4-6.

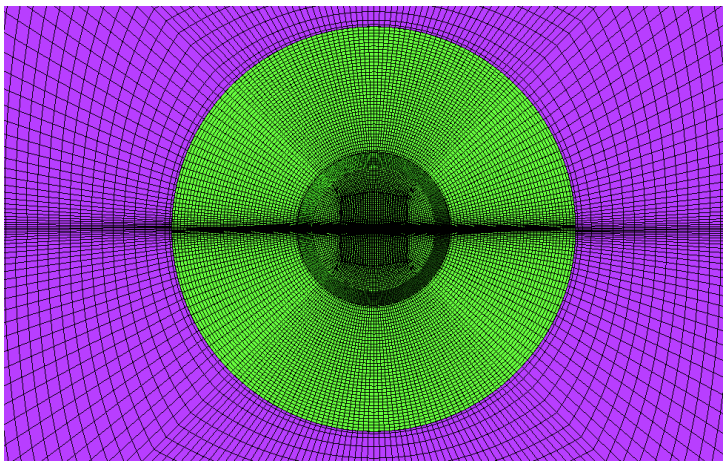

Figure 4-13 Structured mesh on the workpiece

Three welding conditions are investigated in the numerical analysis. The baseline condition consists of rotating speed of 1800 rpm, welding speed of 60mm/min and tool offset of 1.63mm. In the second case, the effect of tool position is studied and the tool offset is reduced to 1.03mm such that the tool is less shifted to aluminum. In the third condition, the welding speed increases to 120mm/min while other parameters remain the same as the base scenario. Numerical convergence is assumed when material and temperature fields cease to change with further iterations.

Table 4-5 Material constants of the constitutive model in equations (4-35) and (4-36)

Material	Q_{def}	**A**	**n**	β
Al 6061 [151]	196.835 kJ/mol	6.26×10^{15}	5.06	5.3×10^{-3}

TRIP steel [152]	387.840 kJ/mol	1.066×10^{14}	4.40	8.7×10^{-3}

Table 4-6 Material constants of the friction model in equation (4-45)

Material	μ_f	**m**	**n**
Al 6061 [112]	0.57	0.95	1.7
TRIP steel [153]	1.60	0.90	1

4.3.3 Results and discussion

4.3.3.1 Velocity boundary at tool-workpiece interface

Material distribution on the top surface of workpiece calculated with velocity boundary condition is shown in Figure 4-14. A swirling phenomenon of the two materials exists in the tool region. This simulation result is inevitable based on the assumption that steel and aluminum have the same rotating velocity at the tool-workpiece boundary. On the contrary, experimental results of material distribution in Chapter 3 show that steel is hardly stirred in the weld zone. The estimated temperature distribution is shown in Figure 4-15. Near the tool center, the temperature is around 1500 ºC, which approaches the melting temperature of steel and is much higher than the experimental measurement results in Chapter 3. This can again be explained from the assumed velocity boundary condition that steel is rotating at a constant speed. Steel has a high viscous flow stress, which generates a large amount of plastic deformation heat and results in an overestimated temperature profile. Based on this initial investigation, the velocity boundary condition shows to be inappropriate for modeling FSW of dissimilar materials, particularly when analysis of material distribution is desired. In the following studies, shear stress condition is applied at the tool-workpiece interface.

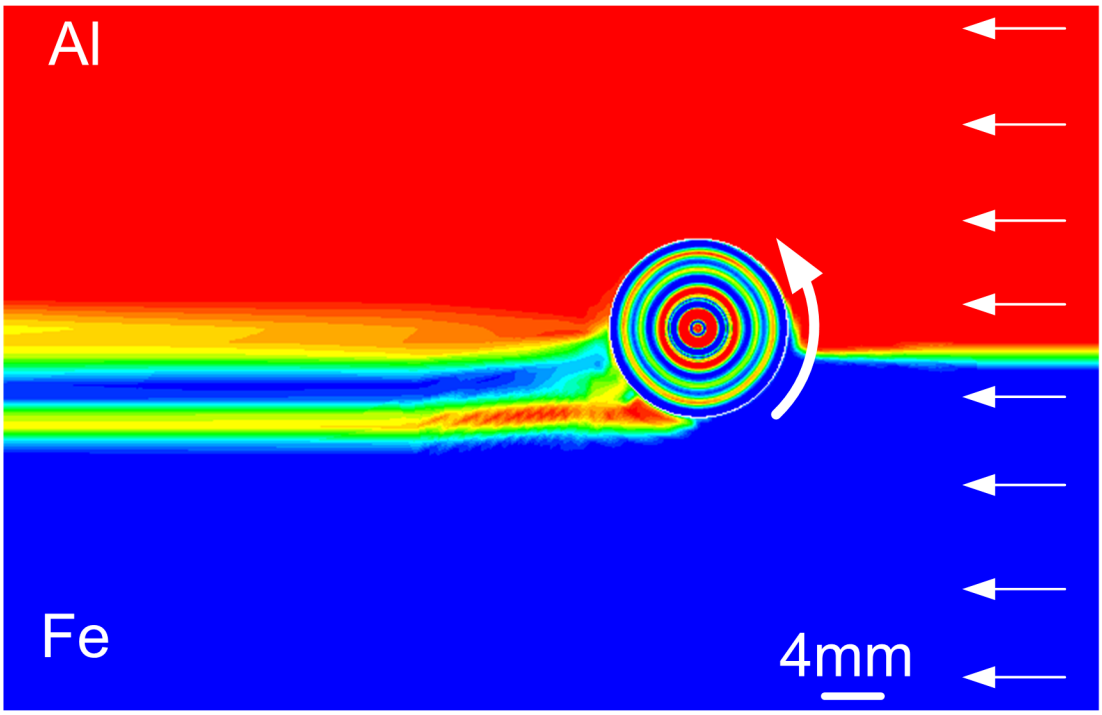

Figure 4-14 Material distribution on workpiece top surface calculated from velocity boundary condition (steel is colored in blue)

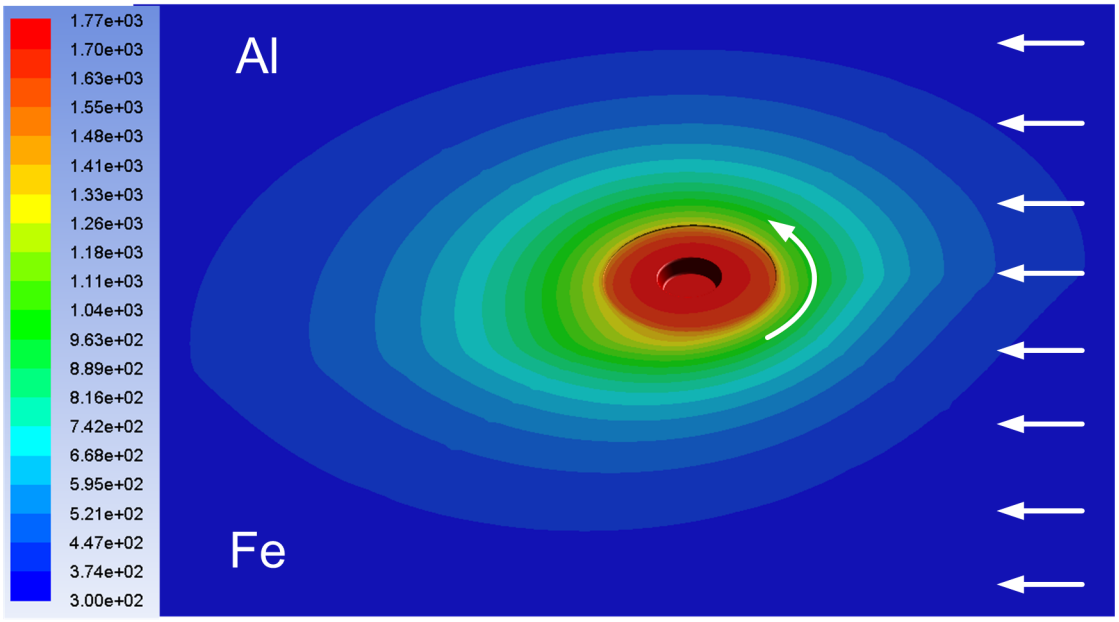

Figure 4-15 Temperature distribution on workpiece top surface calculated from velocity boundary condition (Unit: K)

4.3.3.2 Frictional shear stress boundary at tool-workpiece interface

4.3.3.2.1 Welding condition I: rotating speed 1800rpm, welding speed 60mm/min and tool offset of 1.63mm

In the welding condition with rotating speed of 1800rpm, welding speed of 60mm/min and tool offset of 1.63mm, the material distribution calculated from frictional shear stress boundary based on equation (4-45) is shown in Figure 4-16. On the weld cross section perpendicular to the weldline, the material field shows a good agreement with experimental macrostructure observations, as provided in Figure 3-16. A tilted Al-Fe interface exists in the advancing side. In addition, a chunk of steel strip is embedded in the bulk aluminum matrix in the retreating side.

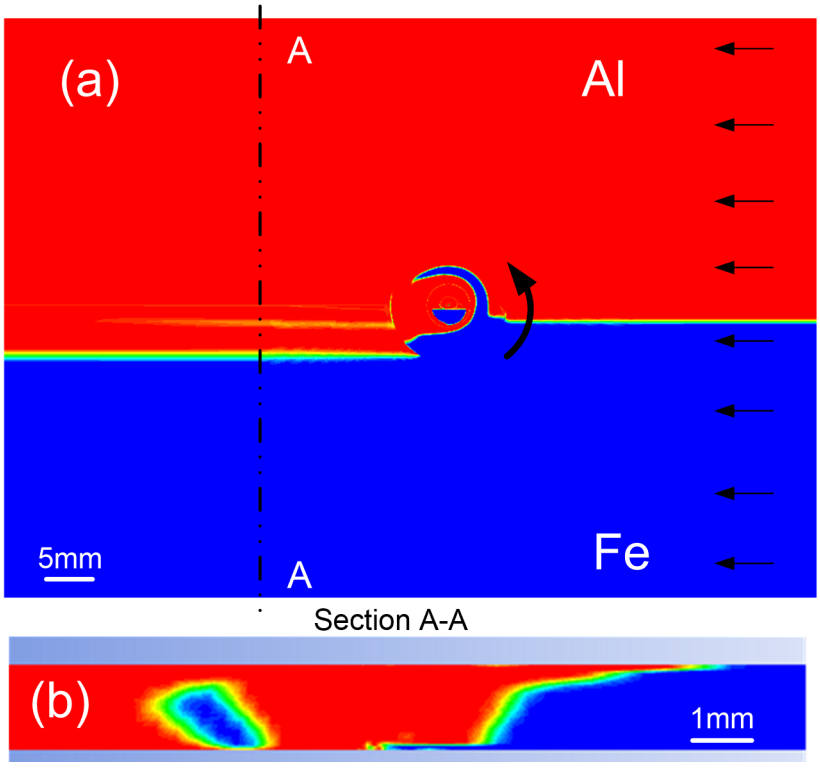

Figure 4-16 Material distribution on (a) Workpiece top surface; (b) A-A section perpendicular to weldline (1800rpm, 60mm/min and tool offset 1.63mm, steel is colored in blue)

In order to understand the mechanisms for the formation of this feature, the calculated material flow fields at different depths below the workpiece top surface are shown in Figure 4-17. The white circle indicates the diameter of the shoulder surface of the FSW tool. As steel materials enter into the deformation region, they split into two branches. In the advancing side away from the center, the steel simply extrudes around the pin. For the steel fraction adjacent to aluminum, it is stirred over and rotates with aluminum. However, as this branch of steel flows past the tool, the rotating motion can hardly be maintained and this branch of steel is not capable of merging back with the original branch. This results in the embedded steel structure when viewed at cross sections perpendicular to weldline. Besides, simulation results show that the volume fraction of the rotating steel branch is larger near the top surface and smaller near the bottom, which leads to an inverted triangular morphology of the embedded steel from cross sectional view. In this welding condition of a relatively large tool offset, the pin is basically surrounded by a thin layer of aluminum. Near workpiece bottom, the steel material can be pushed to directly touch the pin front surface in advancing side. The rectangular distribution of the arrows near the bottom surface is due to the mesh structure since the arrows are drawn at positions of each element. The flow field, which is represented by the directions of the arrows, still shows the curved features.

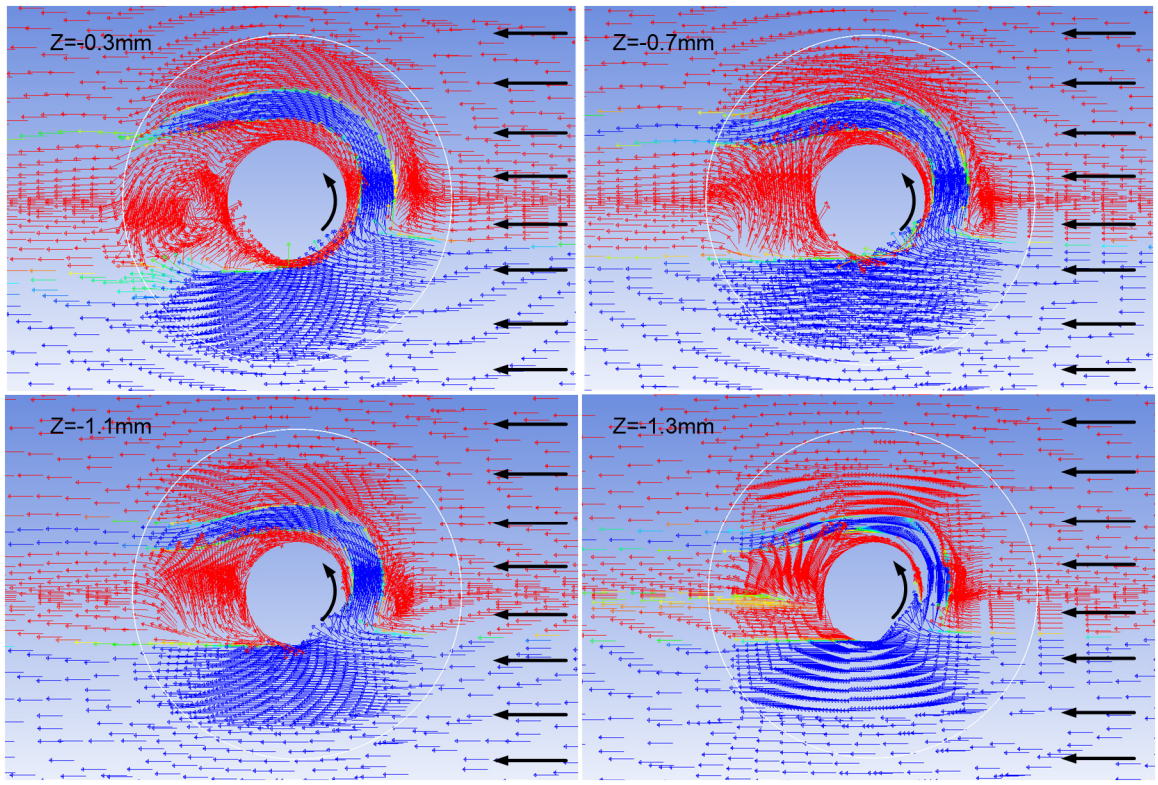

Figure 4-17 Velocity field at different depths colored by material distribution (1800rpm, 60mm/min and tool offset 1.63mm)

Figure 4-18 shows magnitude of material velocity distribution at the tool contact area. In the advancing side and bottom surface of the pin, materials basically flow at the welding speed instead of rotating with the tool. Furthermore, even in the rotating zone, the maximum velocity is only around 0.09m/s. On the other hand, under rotating speed of 1800rpm, tangential velocity on the tool varies linearly from 0 to 1.2m/s in the radial direction. This significantly smaller material velocity from numerical calculation indicates that slipping condition prevails the entire tool contact region, which is also consistent with numerical analysis results from Liechty and Webb [112].

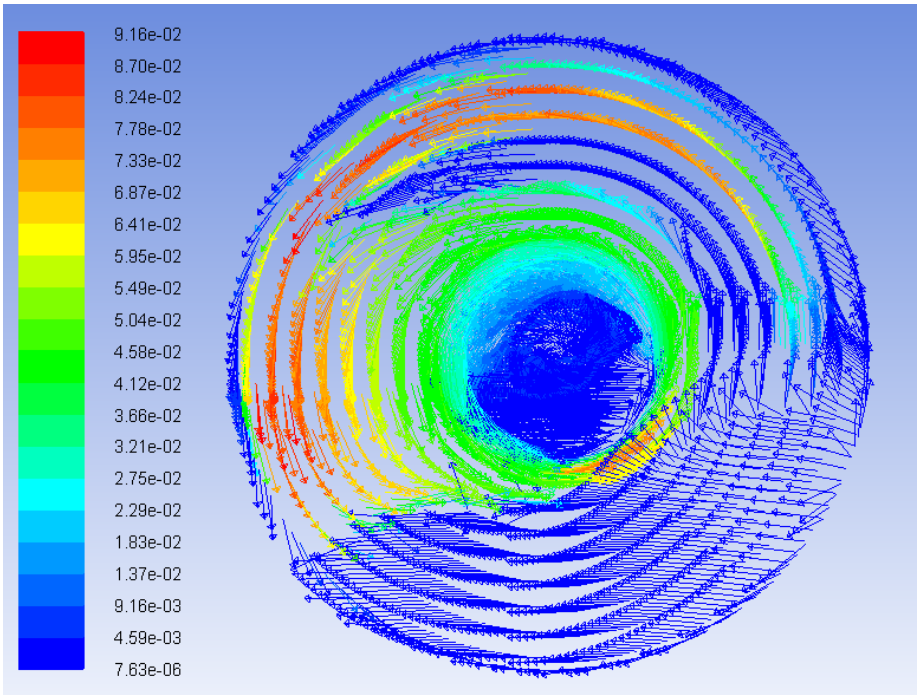

Figure 4-18 Material velocity field (Unit: m/s) at the tool contact region (1800rpm, 60mm/min and tool offset 1.63mm)

Temperature distributions on the workpiece top and bottom surfaces are shown in Figure 4-19. The temperature value calculated from the shear stress boundary is much more reasonable compared with that from the velocity boundary. A larger heat-affected-zone exists in aluminum side as a consequence of its higher thermal conductivity. In the center of pin bottom surface, the temperature is relatively low. This can be attributed to the diminishing velocity of both material and tool in this center area, which leads to a lower heat generation rate. Besides, the thickness of the workpiece is the smallest beneath pin bottom surface, which is only 0.1mm. This makes heat transfer at the backside of workpiece a more influential factor and further decreases the temperature.

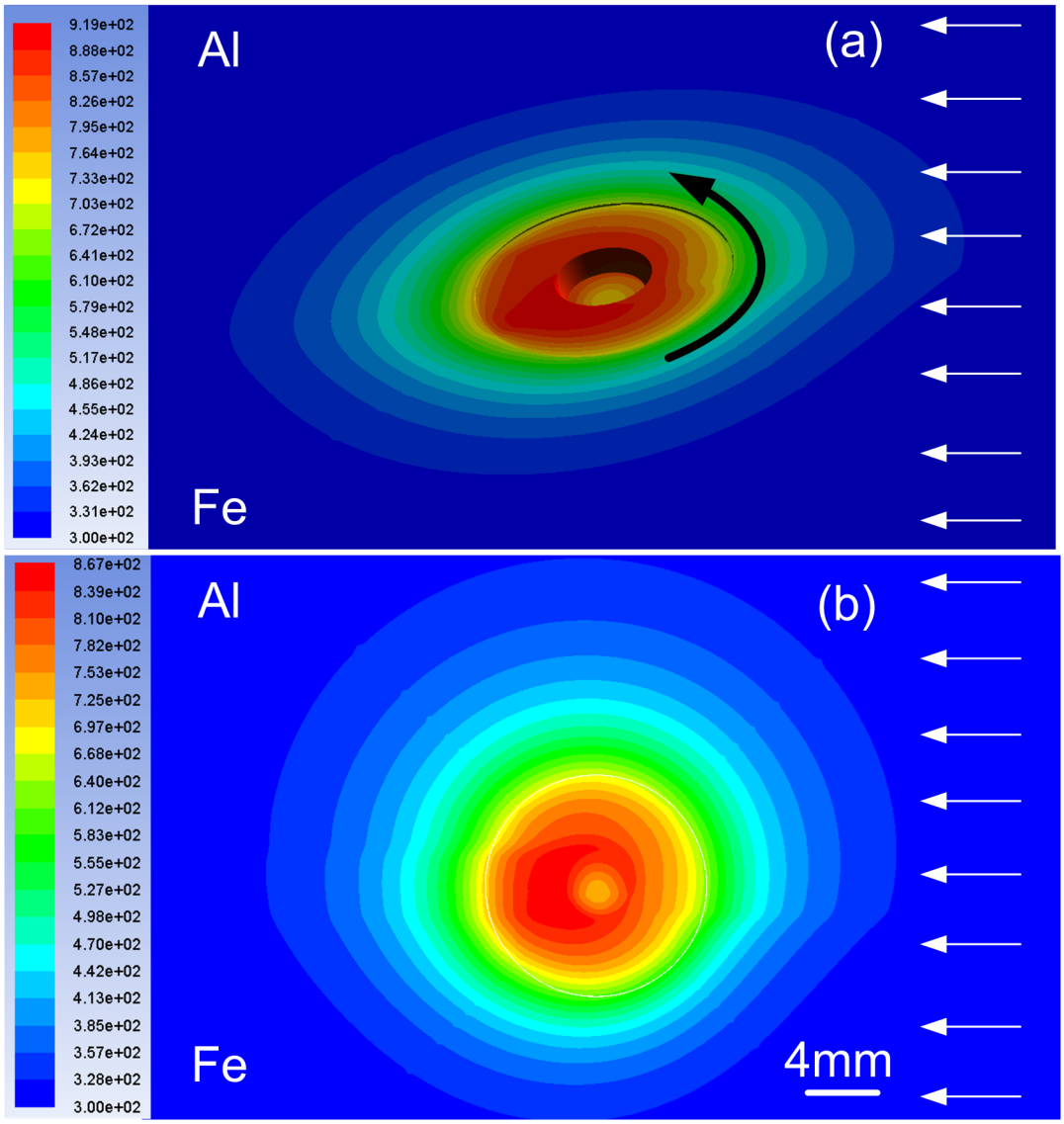

Figure 4-19 Temperature distribution (Unit: K): (a) Top surface; (b) Bottom surface (1800rpm, 60mm/min and tool offset 1.63mm)

Since a steady state welding stage is assumed, the thermal history at one point can be obtained by extracting the temperature profile along the line that is parallel to the welding direction and passes that point. Figure 4-20 (a) compares the calculated thermal history at 1mm position in aluminum side with the thermocouple measured results from Chapter 3, where four thermocouples are embedded in the backing plate and placed symmetrically at distances of 1 mm and 5 mm to the original interface of the two materials. Two peaks occur in the numerical calculated thermal history,

which is due to the localized low temperature region beneath the pin bottom surface as shown in Figure 4-19 (b). Similarly, experimental results also present the two-peak feature in the thermal history curve, which shows agreement with numerical analysis. On the other hand, the peak temperature value is slightly overestimated. The calculated thermal history at the 5mm position in steel side agrees well with the experimental measurement, as shown in Figure 4-20 (b). Since this location is away from pin center and avoids the local low temperature region, the temperature increases as the tool approaches and then decreases after the tool passes by, which is generally observed in most thermal history measurements. In addition, due to the relatively small thermal conductivity of steel, the peak temperature is much lower at this relatively distant location.

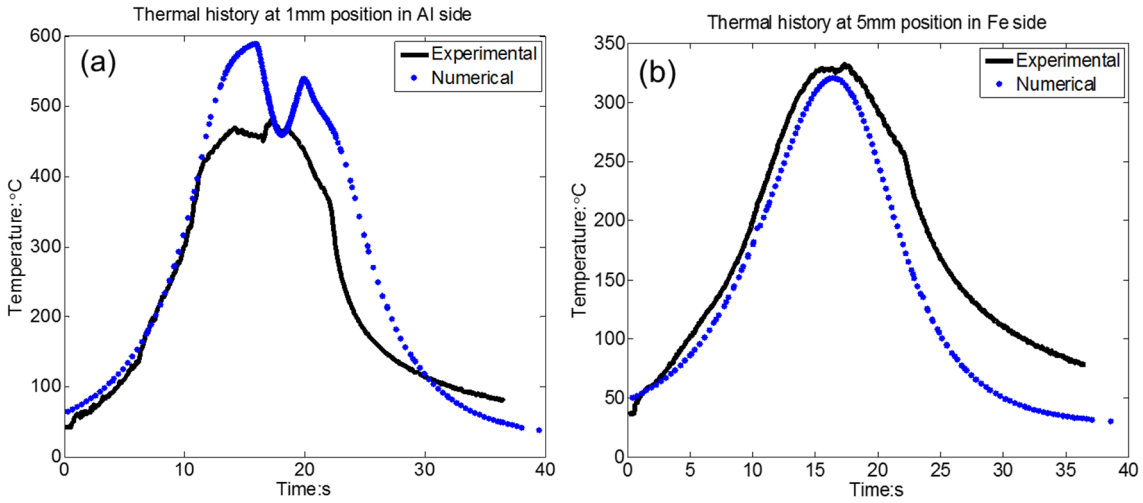

Figure 4-20 Validation of thermal history on the bottom surface: (a) 1mm position in aluminum side; (b) 5mm position in steel side

Figure 4-21 compares the maximum temperature recorded by the thermocouples during the entire welding process with the calculated temperature at the corresponding four locations. Overall the predicted temperature distribution is qualitatively in agreement with the experimental measurements. Regarding the two spots located symmetrically 1mm to the abutting edge, the maximum temperature in aluminum region is slightly larger than that in steel region. This can be

attributed to the offset of the tool into aluminum, which results in the heat source located closer to the 1mm position in aluminum side and accordingly a higher temperature. Regarding the two measurement spots located 5mm to the abutting edge, the higher temperature in aluminum region is primarily due to its larger thermal conductivity compared with steel. On the other hand, the temperature values obtained from numerical analysis are larger than experimental findings. In the numerical perspective, this deviation can be generated from the approximated material properties and simplified heat transfer boundary conditions. In the experimental perspective, the thermocouples are embedded in the backing plate, which leads to heat dissipation and the measured temperature is likely to be lower than the actual temperature on the workpiece bottom surface.

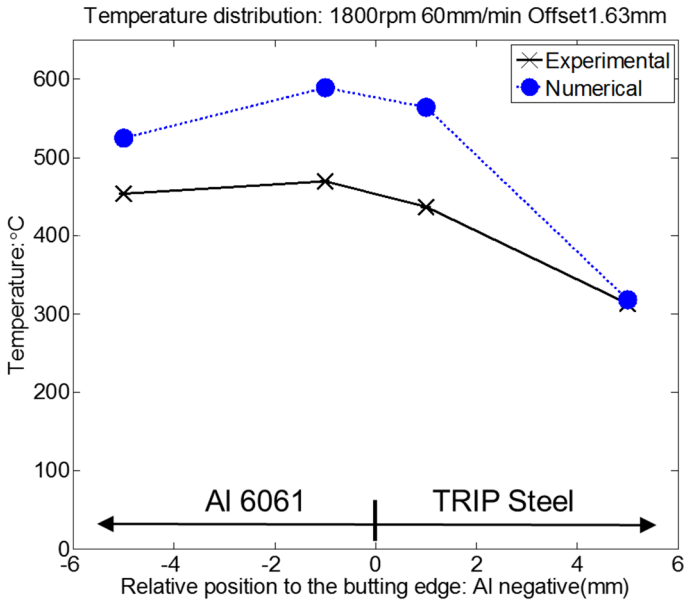

Figure 4-21 Validation of temperature distribution on bottom surface

4.3.3.2.2 Welding condition II: rotating speed 1800rpm, welding speed 60mm/min and tool offset of 1.03mm

In order to further verify the developed model, a smaller tool offset condition was studied. The calculated material distribution is shown in Figure 4-22. Since the FSW tool is less shifted

into aluminum side in the smaller tool offset condition, larger amount of steel is involved in the weld nugget from the view of the workpiece top surface. Similar to the condition of larger tool offset, an embedded steel strip in aluminum side exists in weld cross sections. The volume of this embedded steel strip is relatively larger than the larger tool offset condition. Material flow fields at different depths below the workpiece top surface are shown in Figure 4-23. Similarly, the inflow steel is separated into two branches as it enters into the stirring zone. The rotating branch cannot finish the full circle movement to merge back with the original inflow of the steel. This branch is therefore embedded in the aluminum side after the tool passes by. The width of this steel branch is larger on higher planes closer to top surface, which results in an inverted triangle geometry in the cross sectional view. In this smaller tool offset scenario, the pin is basically surrounded by steel. The rotating branch of steel can move towards original inflow branch to a larger distance, which allows aluminum to touch only a small portion of the pin rear boundary.

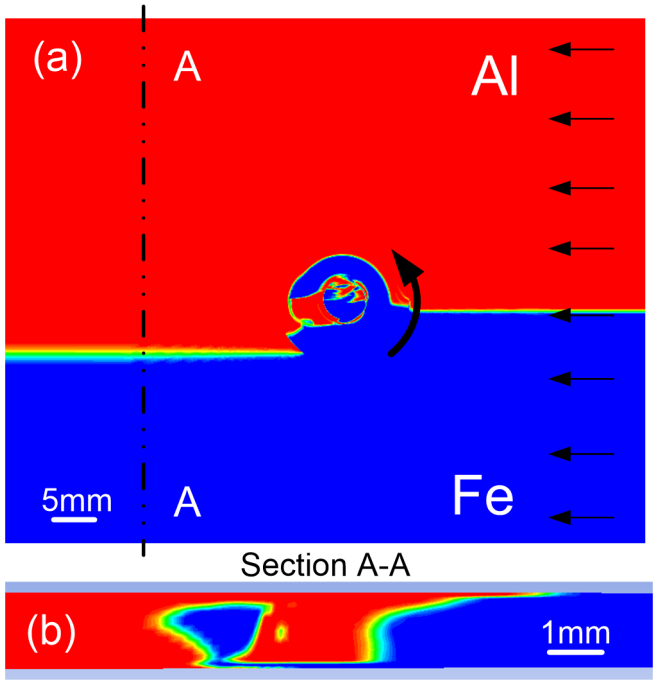

Figure 4-22 Material distribution in the condition of a smaller tool offset 1.03mm: (a) Workpiece top surface; (b) A-A section perpendicular to weldline

The magnitude of material velocity distribution at tool contact region under this smaller tool offset condition is shown in Figure 4-24. Similarly to the larger tool offset condition, materials in advancing side and at pin bottom surface are basically flowing past the tool at the welding speed. In retreating side, steel and aluminum are rotating at a much smaller speed compared with that of the tool. On the other hand, the overall material velocity is slightly smaller compared with that in the larger tool offset condition, which can be attributed to the involvement of larger amount of steel.

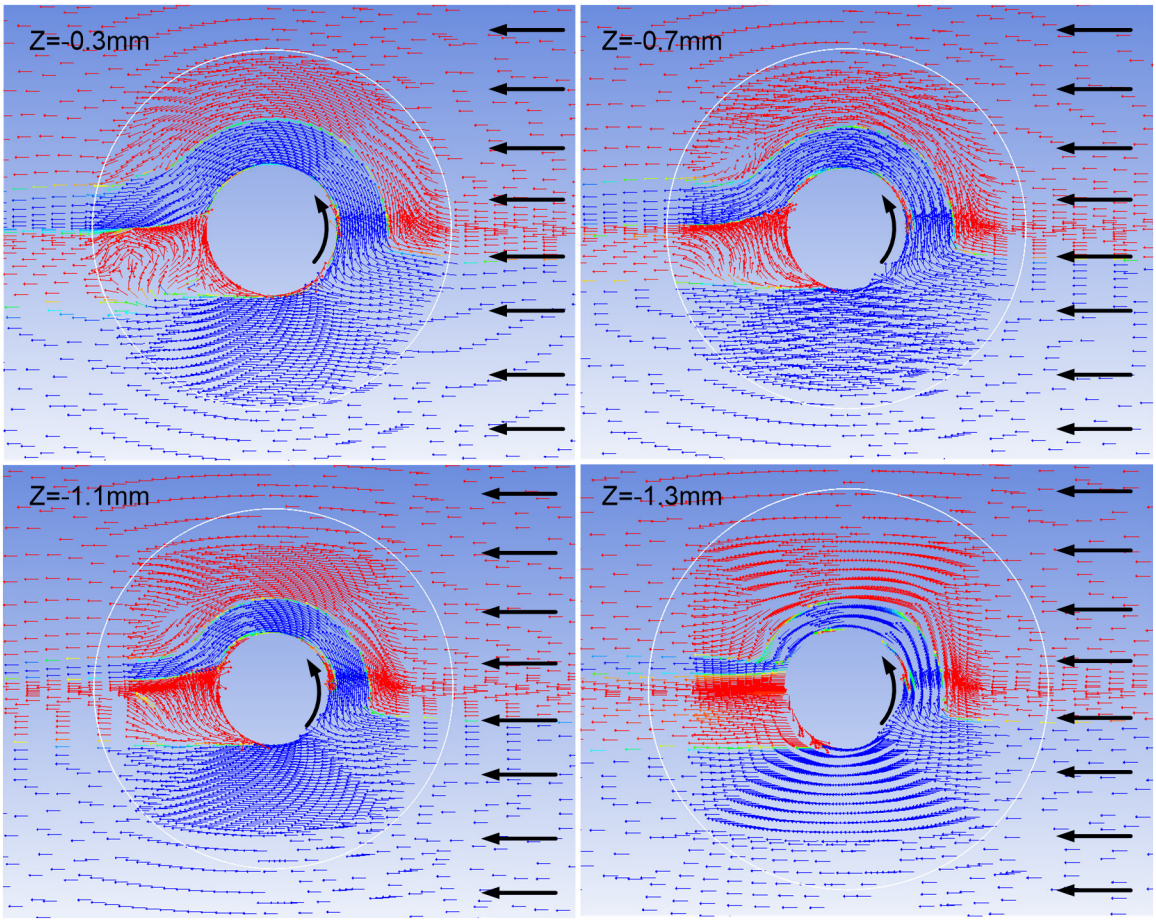

Figure 4-23 Velocity field at different depths colored by material distribution in the condition of a smaller tool offset 1.03mm

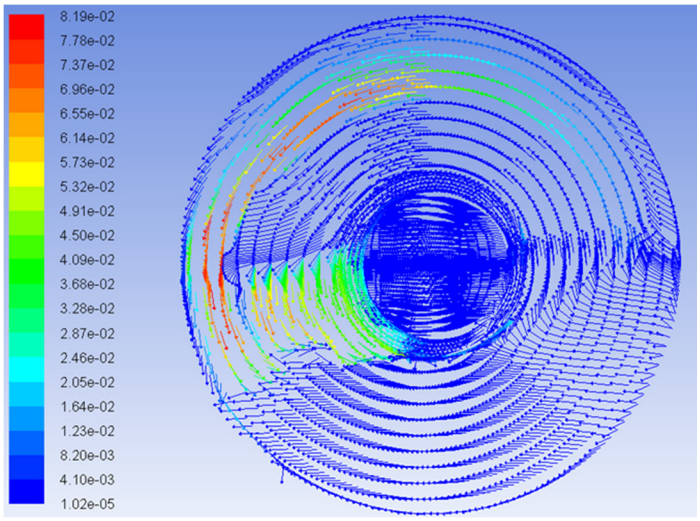

Figure 4-24 Material velocity field (Unit: m/s) at the tool contact region in condition of a smaller tool offset 1.03mm

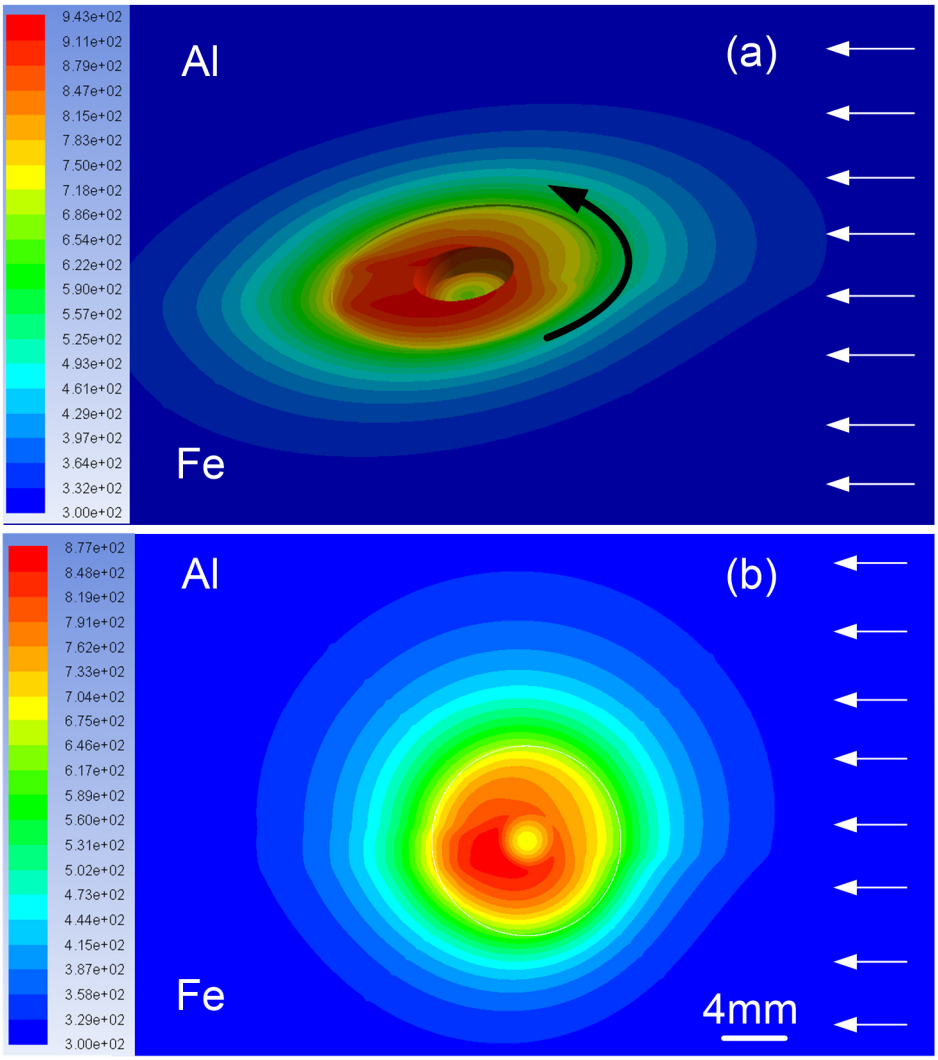

Figure 4-25 Temperature distribution (Unit: K) in the condition of a smaller tool offset 1.03mm: (a) Top surface; (b) Bottom surface

Temperature distribution on workpiece top and bottom surfaces are shown in Figure 4-25, which is also very similar to the profile in the larger tool offset condition both qualitatively and quantitatively. The high temperature region in aluminum side is larger than that in steel side. Compared with experimental results, the estimated temperature on bottom surface is again relatively higher, as shown in Figure 4-26.

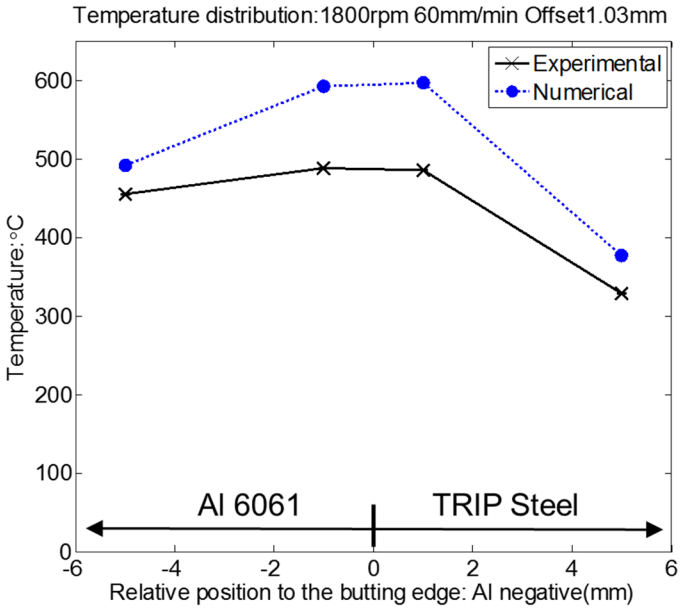

Figure 4-26 Temperature distribution validation on workpiece bottom surface in the condition of a smaller tool offset 1.03mm

4.3.3.2.3 Welding condition III: rotating speed 1800rpm, welding speed 120mm/min and tool offset of 1.63mm

The developed model is then further evaluated in the condition of a larger welding speed of 120mm/min. Figure 4-27 shows the calculated material distribution. Increasing welding speed enables the branch of steel in advancing side to rotate backward to a further degree, which leaves a larger amount of embedded steel from the cross sectional view. The plot of material flow behaviors at the tool contact boundary is provided in Figure 4-28. The flow field remains roughly unchanged compared with the condition of lower welding speed. Despite the increment of material

inflow speed, the maximum velocity magnitude from rotating motion increases by only around 0.004m/s.

Figure 4-29 compares experimental measurement and numerical result of the thermal history at 1mm position in aluminum side. Similarly, the relatively low temperature in center of pin region yields two humps in the thermal history curve, which matches well with the experimental findings. In addition, numerical analysis also shows that by increasing the welding speed from 60mm/min to 120mm/min, the peak temperature experienced at this position during the whole welding process remains basically unchanged. Larger welding speed, on the other hand, can directly reduce the length of thermal cycle. Same conclusions are also drawn from the experimental observations in Chapter 3.

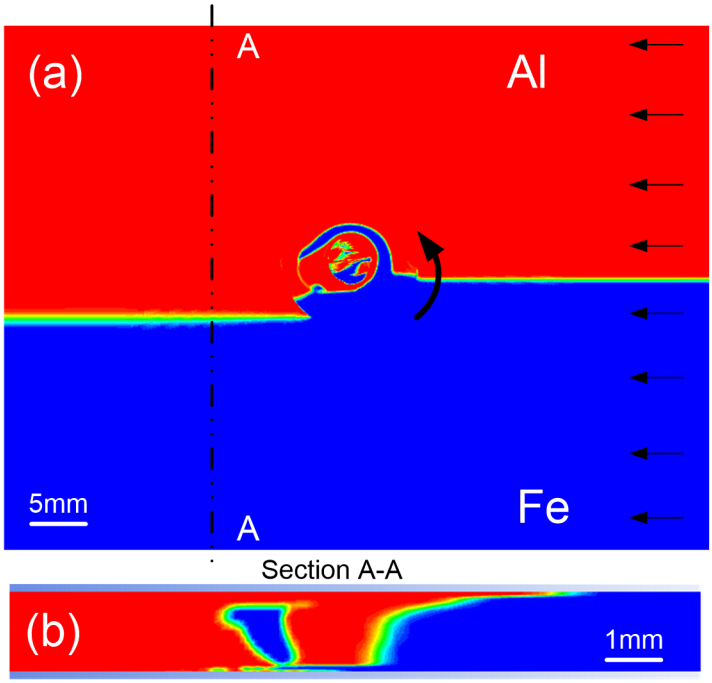

Figure 4-27 Material distribution in the condition of a larger welding speed 120mm/min: (a) Workpiece top surface; (b) A-A section perpendicular to weldline

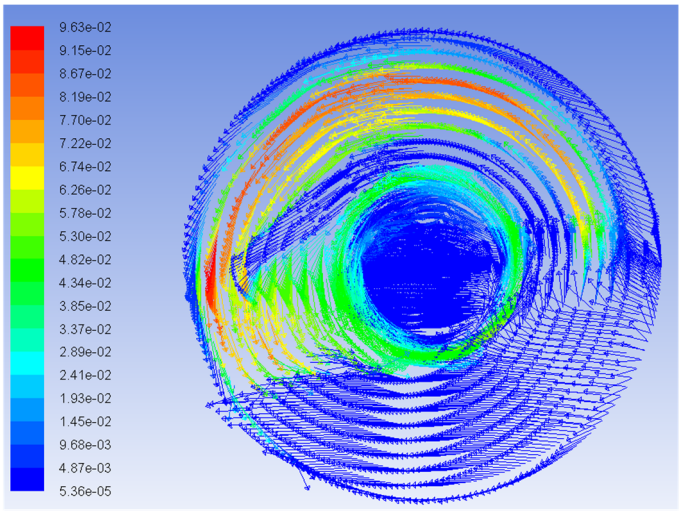

Figure 4-28 Material velocity field (Unit: m/s) at the tool contact region in the condition of a larger welding speed 120mm/min

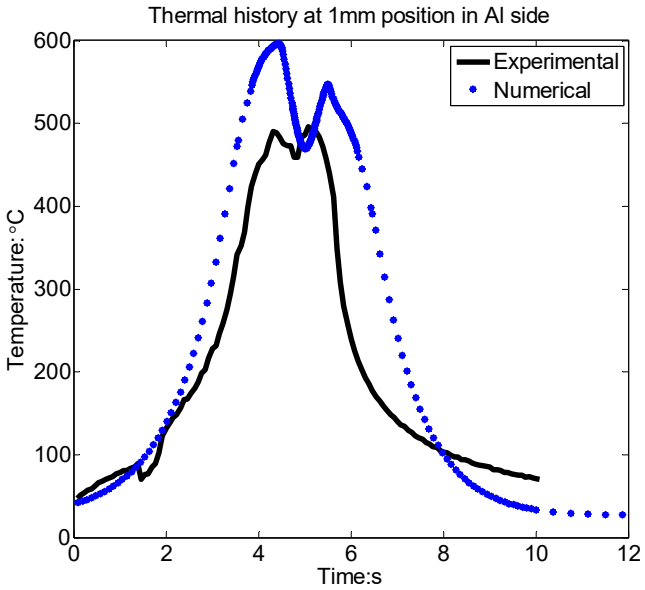

Figure 4-29 Validation of thermal history on the bottom surface at 1mm position in aluminum side in condition of a larger welding speed 120mm/min

4.4 Summaries and conclusions

In this chapter, coupled thermal mechanical models of FSW of dissimilar Al 6061 and TRIP steel were developed for plunge and stable welding stages respectively. For the plunge stage modeling, the field variable α was introduced to identify the regions of steel and aluminum and

define the generalized material properties. A separate set of governing equations were also developed at the two materials interface to account for discontinuities. The corresponding numerical analysis was performed in the FEA software ABAQUS. Overall the calculated axial force and material distribution correlated well with experimental results in the two plunge conditions with different tool offsets.

The stable welding stage was modeled based on Eulerian formulation. Multiple phase flow theories with volume of fluid method were used for deriving analytical formulations, which were further implemented into the FLUENT software for numerical analysis. At the tool-workpiece contact interface, a frictional shear stress boundary yielded a much more reasonable material distribution compared with the velocity boundary condition. The model can capture the macrostructure feature of embedded steel strip in aluminum side, which was experimentally observed in the weld cross sections. On the tool contact region, the calculated material velocity was significantly smaller than that of the tool, which indicated a prevailing slipping boundary condition. The predicted temperature profile and thermal history curves generally agreed well with experimental results under different weld conditions.

CHAPTER 5

ELECTRICALLY ASSISTED FRICTION STIR WELDING

5.1 Literature review

The solid state nature brings FSW with several advantages for welding dissimilar materials. However, the high welding force demanded for stirring plasticized material in solid state exacerbates tool wear issues and raises the requirement for both a high stiffness machine and corresponding strong fixture design. Furthermore, based on our previous studies on FSW of Al to steel, the processing window for achieving satisfying joints is narrow and joint quality is sensitive to welding parameters. The insufficiently plasticized steel intermixed with the nearly melted aluminum is likely to generate porosities and other welding defects. Solutions for improving FSW and reducing welding force generally fall into two categories. The first one is to develop FSW tools with complex geometries made from refractory materials, such as tungsten carbide, tungsten-rhenium, Si_3N_4 and polycrystalline cubic boron nitride (PCBN). Threads and flutes are designed on the pin and shoulder surface, which can promote plasticized material flow and reduce stirring force as shown by Mishra and Ma [10]. The second category is to explore benefits of hybrid FSW process where various types of auxiliary energy are introduced into the original process. Palm [154] patented a laser assisted FSW methods where a laser beam was exposed onto the workpiece

directly ahead of the rotating FSW tool. Similar studies were carried out by Sun and Fujii [155], where defect free joints were achieved under a faster welding speed twice as large as that for conventional process. Merklein and Giera [156] studied the laser assisted FSW for steel-aluminum tailored blanks and an enhanced weldability was accomplished from the results of both tensile and deep drawing tests. An arc enhanced FSW process was proposed by Cao and Kou [157], where the workpiece was preheated by an electric arc. Widened processing window was observed. Bang et al. [158] applied gas tungsten arc into FSW process for joining dissimilar Al6061 to STS 304 stainless steel. According to their results, transverse tensile strength could reach 93% of the base aluminum alloy and the ductility of the joints was increased with a ductile fracture mode. Park [84] developed an ultrasonic assisted FSW process and reported that ultrasonic vibration helped eliminate the wormhole defect at the weld root. Grant et al. [159] implemented an induction heating system in front of the FSW tool and obtained great amount of load reductions on the tool.

In addition to the above external energy sources, resistance heating associated with electrical current is another type of effective heat input for improving FSW process. Santos et al. [160] reported that electrical current could help increase material viscoplasticity in the weld root and eliminate potential root defect, which therefore increased welding reliability. Ferrando et al. [161] reported an approximately 90% of axial force reduction when electrical current was introduced into the stirring zone through the FSW tool. Luo et al. [162] designed and fabricated a new FSW tool to carry electrical current into the process. The tool was also equipped with cooling, gas shielding, insulation and measurement systems. They studied the electrically assisted FSW process for joining magnesium alloy AZ31B, aluminum alloy Al 7075 and other steel alloys including 2Cr13Mn9Ni4 and Q235B.

All these studies considered the benefits of electrical current from the perspective of resistance heating. Taking the electro-plastic effect into consideration, Pitschman et al. [163] investigated the feasibility of incorporating this phenomenon into FSW process for joining aluminum alloy Al 6061 and reported an improvement on welding speed as well as reduction of energy consumption. Similar study was also conducted by Potluri et al. [164], where an average reduction of 58% of feed force was observed. In both their studies, a hole was predrilled on the workpiece to facilitate the plunge stage and the electro-plastic effect was considered primarily during the welding stage. However, it is not generally available to prepare a hole on the workpiece and significant tool wear can occur during the plunge stage [12-14]. Besides, in most of the above electrically assisted processes, electrical current was introduced from the tool. This requires the tool to be made of electrically conductive materials and complex insulation system to be installed between the tool and FSW machine. Furthermore, the associated resistance heating and electro-plastic effect can also reduce the tool strength during stirring process and lead to potentially premature wear. Other experimental arrangements included stationary connections between electrodes and workpiece, such as the one described in [163]. The electrodes were clamped at two ends of the weld specimen, which would require narrow specimens to guarantee the high electrical current density.

In this study, a new electrode configuration is developed, which enables a passive involvement of the tool in the electrical circuit and sets little restrictions on workpiece dimensions. Based on this hybrid FSW testbed, first the electro-plastic effect is investigated for the plunge stage of Al 6061 and TRIP steel separately. Then the hybrid friction stir welding process is carried out to joining these dissimilar materials together. Mechanical welding force, temperature

distribution and microstructure under various process parameters are analyzed and compared between conventional and electrically assisted FSW conditions.

5.2 Experimental system development for the electrically assisted FSW process

5.2.1 Design of the electrically assisted FSW system

The CAD design of the entire electrically-assisted FSW system is shown in Figure 5-1 and the actual experimental system is shown in Figure 5-2. Instead of using the tool as one electrode, two copper brushes were added and pressed against the top surface of the workpiece, serving as the anode and cathode respectively. The copper brushes are mounted to the spindle holder through several brackets, the lengths and positions of which can be adjusted to place the electrodes to an optimized position for electrical current distribution. The copper brushes can translate along the weld line together with the FSW tool in close proximity. Considering the roughness of the workpiece top surface, the two electrodes are preloaded with compressive springs. This helps guarantee the electrical conductance as the electrodes slid on the workpiece and addresses the concerns of possible spark generation.

With this configuration, certain amount of electrical current is anticipated to still flow through the tool since the tool pin is submerged inside the workpiece during the welding process. However, the tool is only passively involved in the circuit and the electrical current would flow along the shortest path with the lowest resistance. The voltage of FSW tool under a current of 560A was measured to be around 3mV when the tool was pressed again the workpiece in the initial investigations. This electrical current field can therefore effectively reduce direct resistance heating of the tool. Furthermore, insulation issues of the tool can be avoided. Electrical insulation of the tool can be extremely difficult since the tool is rotating under a combined condition of high stress and temperature. There are few generally available insulation materials that can maintain a

good strength at high temperature. Moreover, since the tool is subjected to a large transverse force in the welding direction as it translates along the weldline, a slight offset between the tool rotating axis and the tool geometry axis can lead to fracture of the tool, especially for tools made of relatively brittle materials such as tungsten carbide. If an electrical insulation layer is to be inserted between the tool and tool holder, the tool runout needs to be strictly controlled.

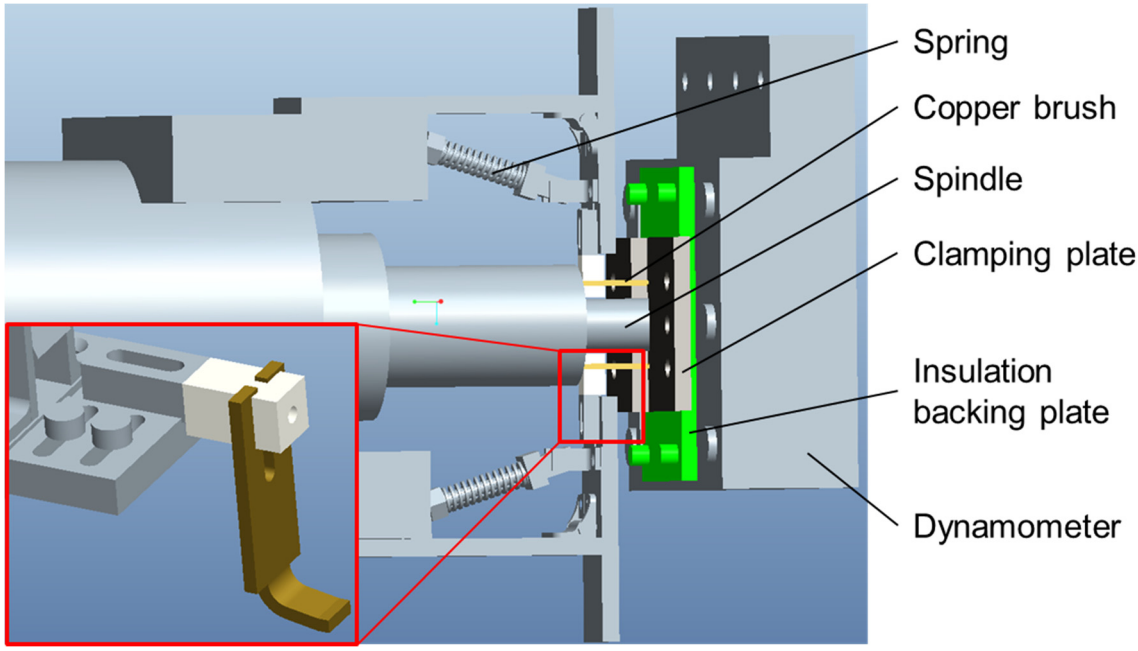

Figure 5-1 CAD design of the electrically assisted friction stir welding system

Electrodes are bolted to the leads of the welder, Lincoln Electric Power Wave 455, which again serves as the electrical power source. The magnitude of the current is monitored using an OMEGA HHM596C multimeter during the process. Insulation between the electrodes and its mounting brackets is achieved through mica washers. The bolts are also electrically insulated with plastic flanged sleeve bearings, so that both the pressing surface and thread surface are avoided from touching the electrodes. Same insulation methods are also applied for the bolts on the workpiece clamping fixture.

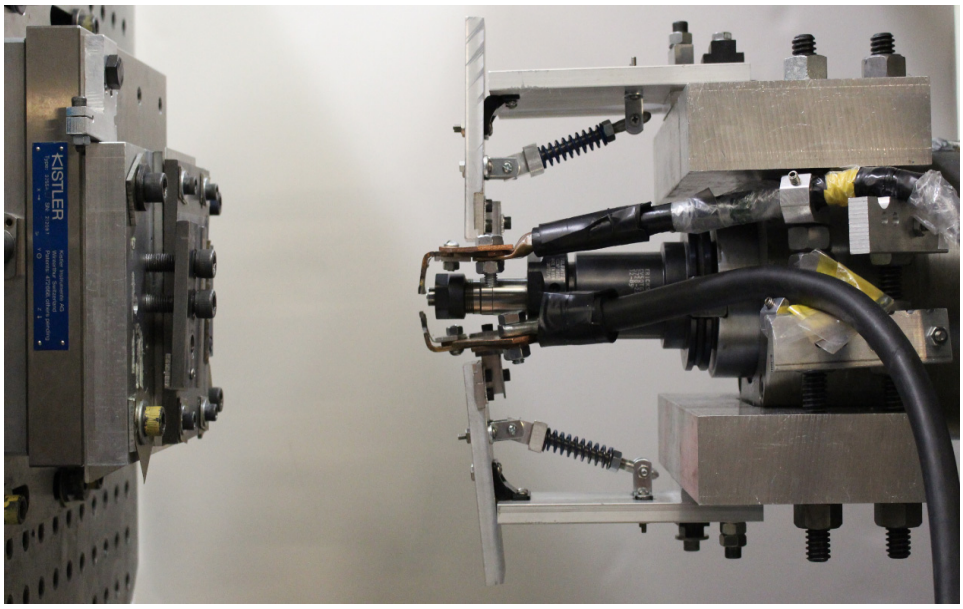

Figure 5-2 Experimental system for the electrically assist FSW

To maximize the current density, steel and aluminum workpieces need to be electrically isolated from the backing plate. In this study, thin layer of mica sheet is initially attempted as a suitable candidate for insulation materials, which also enables temperature measurement during the process. A detailed illustration of the experimental setup is provided in Figure 5-3. Below the thin mica sheet is a steel backing plate with three thermocouples embedded inside. The thermocouples are submerged 1mm below the top surface of steel and located beneath the original Al-Fe interface at the beginning, middle and ending positions of the weld, as shown in Figure 5-3 (b). Initial attempts with this experimental configuration showed that the insulation mica sheet was undesirably bonded to the workpiece bottom surface under the combined conditions of high temperature and pressure during FSW process. A small amount of mica fragments were stirred into the weld zone and distributed along the Al-Fe interface in the joint cross section, which generated visible cracks and substantially deteriorated the joint quality. To address this problem, ceramic block is employed as the alternative insulation material between workpiece and backing plate. However, due to its intrinsic brittle properties, the ceramic easily gets cracked during

experiments and needs to be changed after every four tests on average. Besides, it is difficult to drill holes and embed thermocouples in the ceramic block. Accordingly the temperature cannot be measured during the process. Based on all these considerations, mica sheets are used as the insulation material for the plunge stage study of aluminum and steel. During friction stir welding of aluminum to steel, mica sheets are only used for temperature measurement to evaluate the relative resistance heating effect of electrical current. Ceramics are used for all the subsequent welding force measurement and Al-Fe joint microstructure analysis.

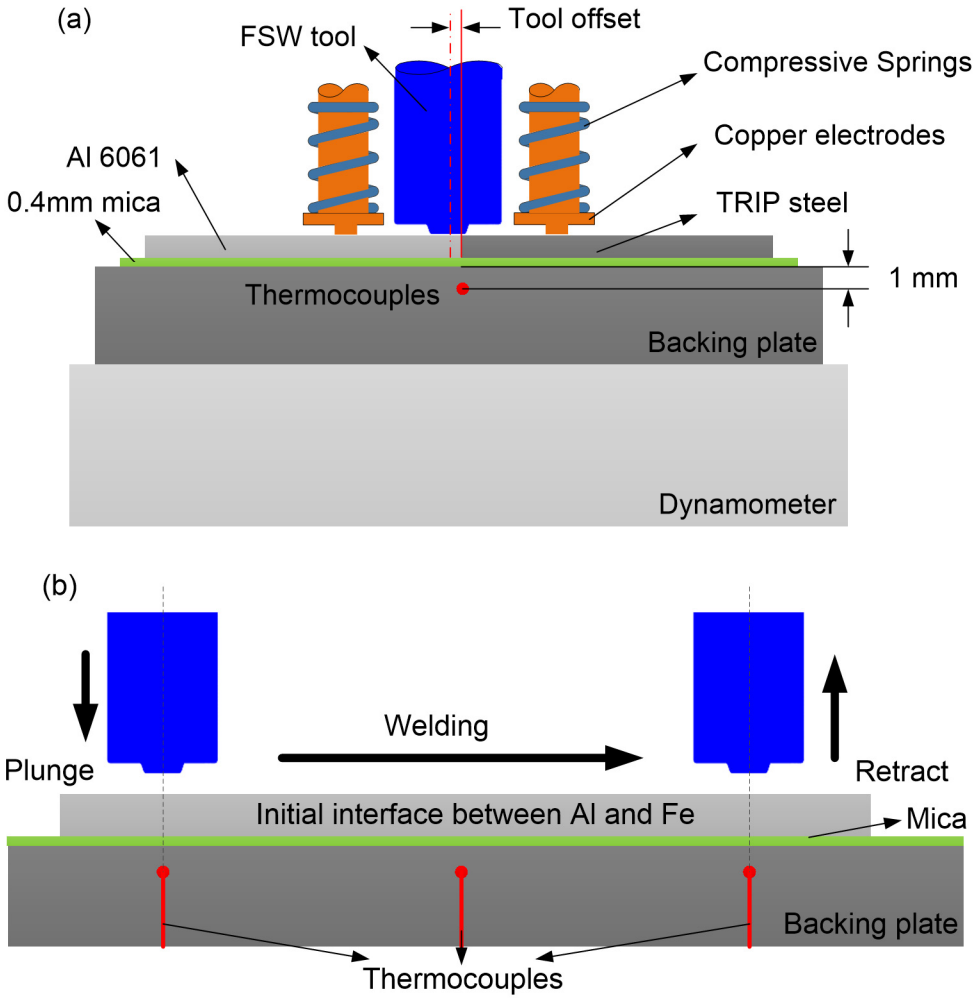

Figure 5-3 Detailed illustration of the experimental setup with mica sheet as the insulation: (a) Overview; (b) Thermocouples location

5.2.2 Analysis of electrical field distribution

Due to the unsmooth weld surface finish and possible splash generation, the copper brush could hardly slide and maintain reliable electrical contact if placed in the wake of the tool. Based on this prerequisite, three schemes of electrodes configuration are proposed and shown in Figure 5-4. In Figure 5-4 (a), both of the copper electrodes are positioned on the steel side and stay in the closest vicinity of each other. This can maximize current density distribution between the two electrodes. The underlying intention for this layout is that steel can be greatly softened while aluminum remains intact, therefore the two materials are mechanically more compatible during the stirring action. However, initial hybrid welding attempts based on this configuration showed that the welding force hardly reduced after applying electrical current. Since the majority of electrical current stays in the enclosed area of the two electrodes, which is outside the stirring zone and contains little plastic deformation, the insignificant force reduction is reasonable.

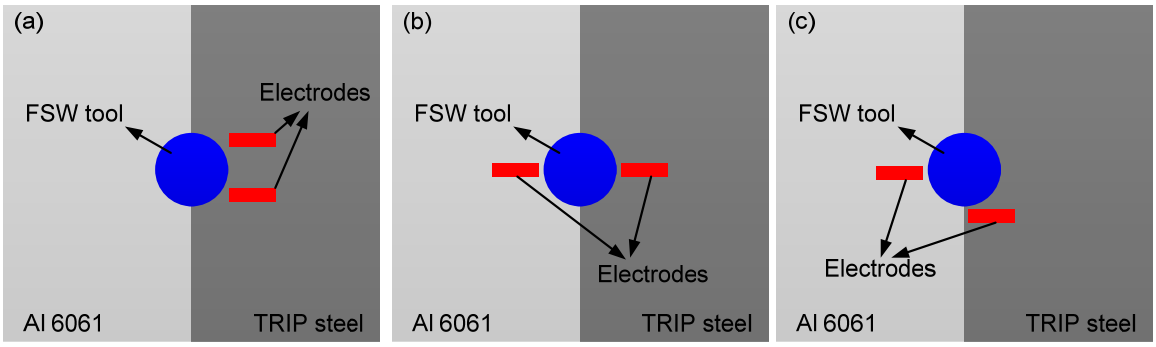

Figure 5-4 Schematic illustration of different electrodes configurations

To guarantee that electrical current flows through the stirring zone, one of the electrodes is rearranged to slide on the aluminum side, as shown in Figure 5-4 (b). Corresponding current density distribution and associated resistance heating are analyzed with the COMSOL software, which helps provide a guideline for optimizing electrodes positions. In the multiphysics model, perfect contact is assumed at the faying surface of the two materials as well as the interface

between copper electrodes and workpiece top surface. A total current of 560 Amp is applied to the electrode on aluminum side and the electrode on steel side is grounded, while other surfaces are electrically isolated. Thermal boundary conditions are set with a surface heat transfer coefficient of 10W/(m^2 K) at the top surface of workpiece and thermal insulation is assumed at the back surface based on the low thermal conductivities of either mica or ceramic sheet.

The calculated current density distribution on the workpiece is shown in Figure 5-5. High current density is concentrated in the vicinity of the electrodes. In the tool stirring zone, the current density varies approximately from 5A/mm^2 to 17A/mm^2. This range is relatively small for initiating electro-plastic effect, especially in the center region where the largest deformation occurs due to the stirring action of the tool pin. Despite the different electrical conductivities of aluminum and steel, the electrical field is overall symmetric with respect to the abutting edge. Differences of their electrical properties are more evidently in the aspect of Joule heating effect, as shown in the temperature distribution in Figure 5-6. The temperature profile is captured at the time spot of 10 seconds, which is approximately the length of plunge stage during experiments. The larger resistivity and smaller thermal conduction coefficient of steel results in an intensively local heating on the electrode and its surrounding area. In the tool acting zone in aluminum side, temperature varies approximately from 130 °C to 150 °C. Temperature in the tool acting zone on steel side lies in between 130°C and 250°C.

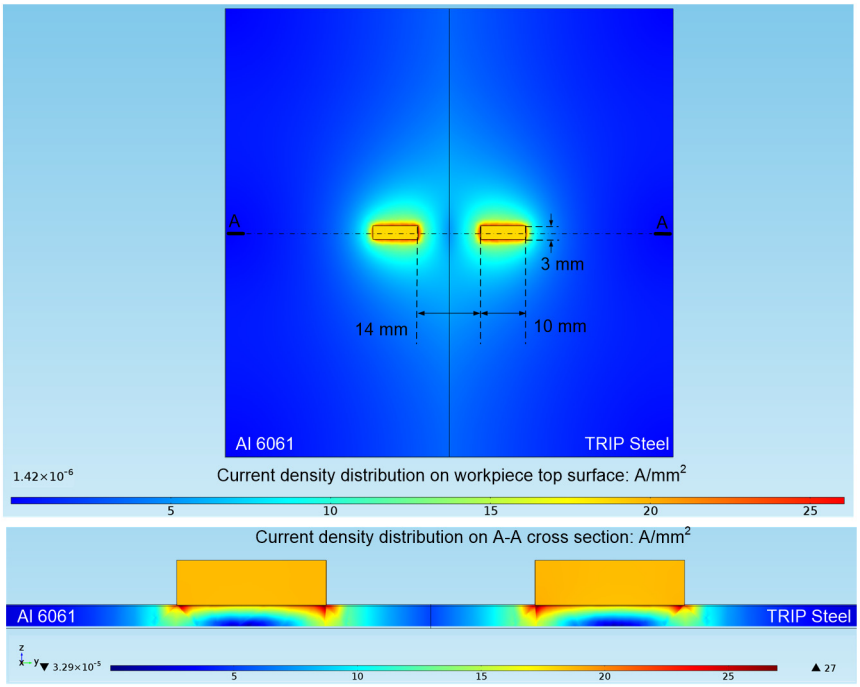

Figure 5-5 Current density distribution for the electrodes configuration of Figure 5-4 (b)

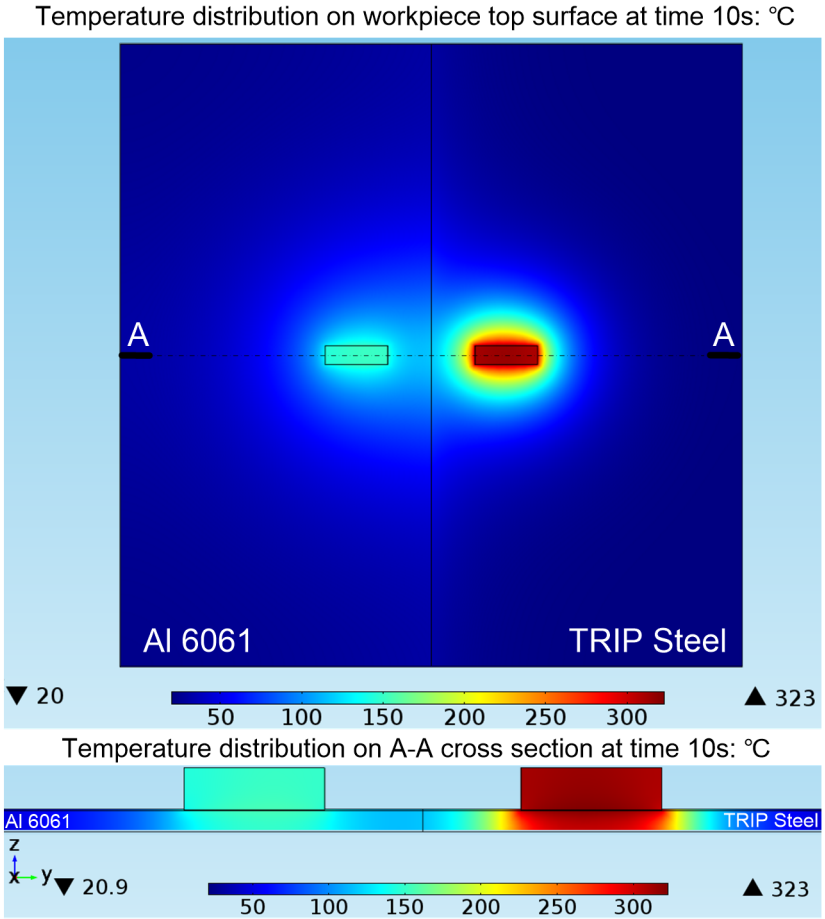

Figure 5-6 Temperature distribution at 10 seconds for the electrodes configuration in Figure 5-4 (b)

Considering the calculated result that the electrical current is more concentrated adjacent to electrodes, it is desired to place electrodes closer to the weldline to increase the current density in stirring zone. An improved configuration is therefore proposed and shown in Figure 5-4 (c), where the electrode on steel side is rearranged to the front of the tool so that it can still slide on the intact workpiece surface and at the same time stay as close to the weld line as possible. Corresponding locations of the electrodes and current density distribution results are shown in Figure 5-7, where A-A cross section coincides with the tool axis plane. Based on this configuration, the current density in the pin stirring zone of steel is overall increased while that in aluminum side remains roughly unchanged. Besides, the temperature result in Figure 5-8 shows that even though the electrode on steel side is still resistance heated to a relatively high value of over 300°C, temperature in the center stirring zone where the tool pin directly acts is greatly reduced. Furthermore, the actual temperature during experiments should be even lower considering the heat conducted away by the entire copper electrode. Based on these investigations, the electrodes layout in Figure 5-4 (c) is adopted as a relatively optimal configuration for the electrically assisted FSW of Al 6061 to TRIP steel in the following studies.

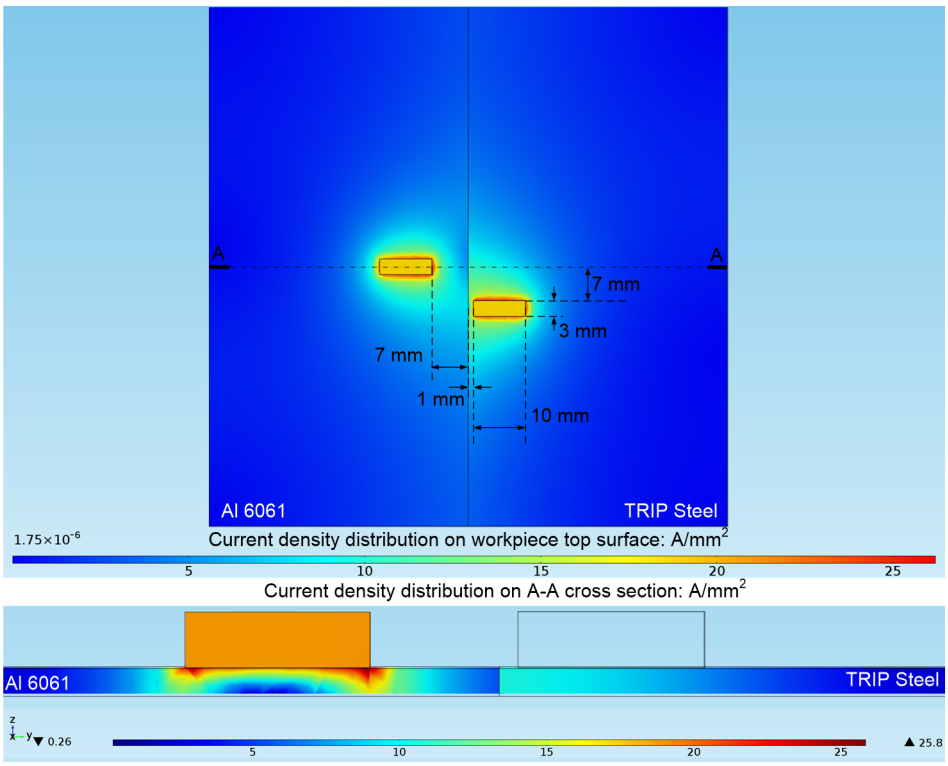

Figure 5-7 Current density distribution for the asymmetric electrodes configuration in Figure 5-4 (c)

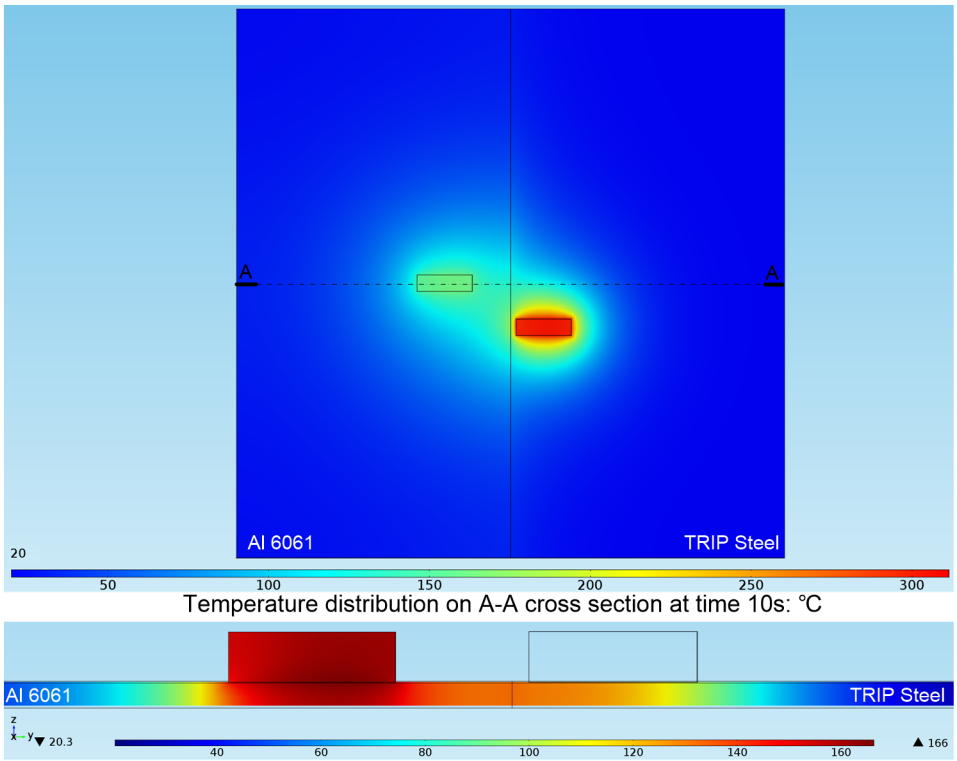

Figure 5-8 Temperature distribution at 10 seconds for the asymmetric electrodes configuration in Figure 5-4 (c)

5.3 Plunge stage study for Al 6061 and TRIP steel separately

5.3.1 Experimental specifications

In order to investigate the feasibility, potential benefits and appropriate current range for applying electricity to friction stir welding process, first the plunge stage was studied on Al 6061 and TRIP steel separately. In order to further reduce the complexity and uncertainty of current distribution at the abutting face of two welding plates, one entire workpiece was used. As described before, the insulation between workpiece and steel backing plate was provided by a thin mica sheet with the thickness of 0.4mm. The tool spindle speed was set at 1200 rpm and plunge speed was 10mm/min. In the condition of plunging into aluminum, the tool kept moving until its whole shoulder surface was immerged below the workpiece top surface. On the other hand, due to the harsh condition associated with stirring steel, the corresponding plunge depth was set to be 0.3mm less than that for aluminum and the tool retracted before the shoulder touches the top surface of steel. Each test condition was conducted three times for repeatability study.

Microstructure analysis was performed for steel specimens at transverse cross sections which pass through the center of the weld. The specimens were ground and polished according to standard metallographic preparation procedures and then further etched with 5% nital solution.

5.3.2 Welding force comparison

Figure 5-9 shows the typical axial plunge force during plunge stage of Al 6061. The x-axis is the tool stroke, which is defined as the distance between the bottom surface of the tool pin and the top surface of the workpiece. The axial force is reduced after application of electrical current, especially at the later stage of plunge process. The force reduction is not obvious in the beginning, which is probably due to the small volume of plastic deformation zone. Initial force increment is

primarily generated from deformation of the relatively soft mica sheet as well as the elastic displacement of the working table due to the structure stiffness of the machine itself. Since the electro-plastic softening is only effective for plastic deformation, the insufficient amount of plastically deformed material results in an insignificant force reduction.

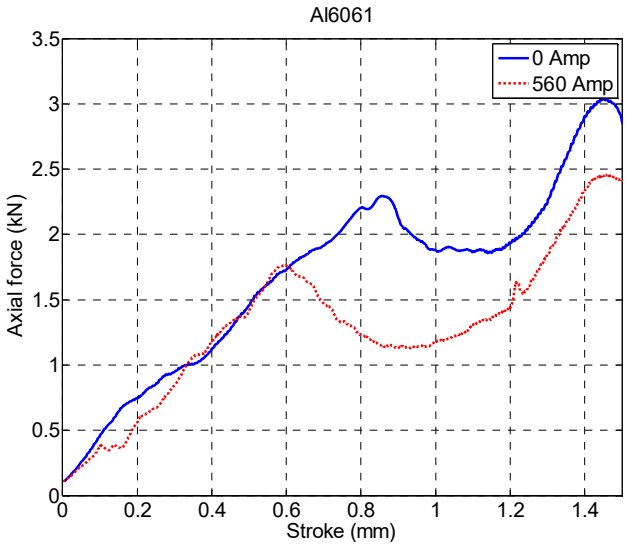

Figure 5-9 Comparison of axial force for Al6061 with and without current

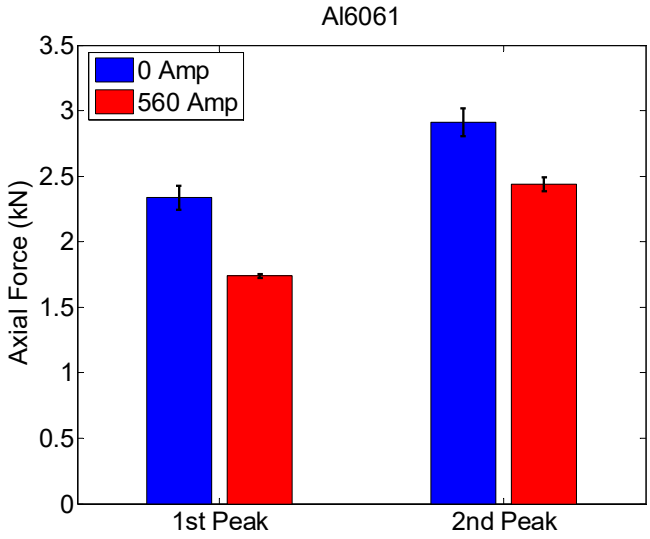

Figure 5-10 Repeatability of the force reduction result for Al6061

Similar to the force measurement results from Park [84], Figure 5-9 shows two peaks in the axial force curve during the plunge stage of same material. Figure 5-10 presents the repeatability

analysis result of these two peak values in the axial welding force. An average force reduction of 25.6% is obtained for the first peak and 16.2% for the second one after the application of electrical current and the results are with a good consistency.

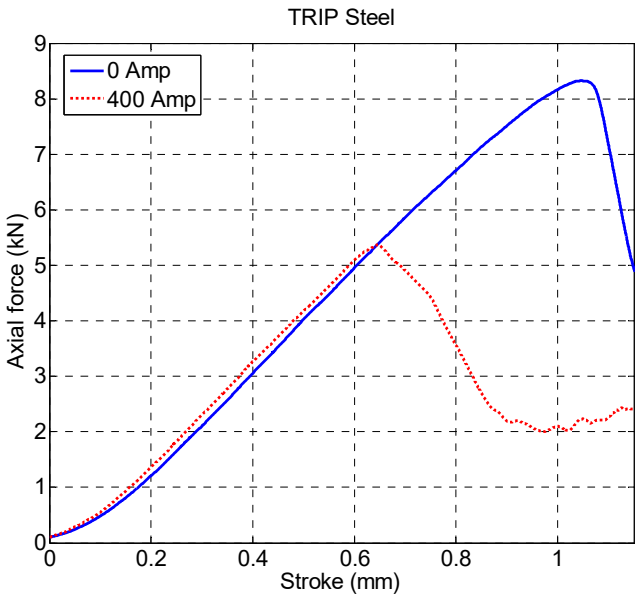

Figure 5-11 Comparison of axial force for TRIP 780 steel with and without current

Figure 5-11 shows the typical axial force curves for plunging into steel. In the case of steel, a 560A current is attempted initially. However, due to its higher electrical resistance, substantial Joule heating effect is observed. Consequently, only a total current of 400A is applied in the following experiments. Force reduction is generally observed except in the initial stage. Since the plunge depth for steel is smaller than that for Al6061 and the tool shoulder does not touch the top surface of steel, only one peak occurs in Figure 5-11, which corresponds to the first peak in Figure 5-9. Figure 5-12 shows the repeatability results on the value of this peak. An average force reduction of 37.5% can be obtained after application of electrical current.

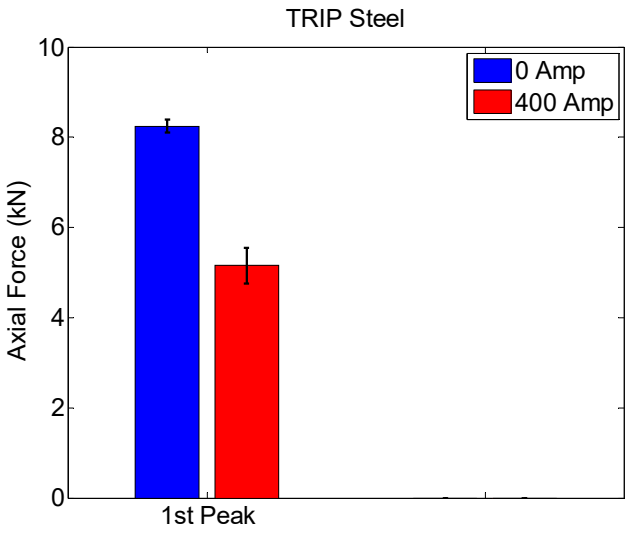

Figure 5-12 Repeatability of the force reduction result for TRIP 780 steel

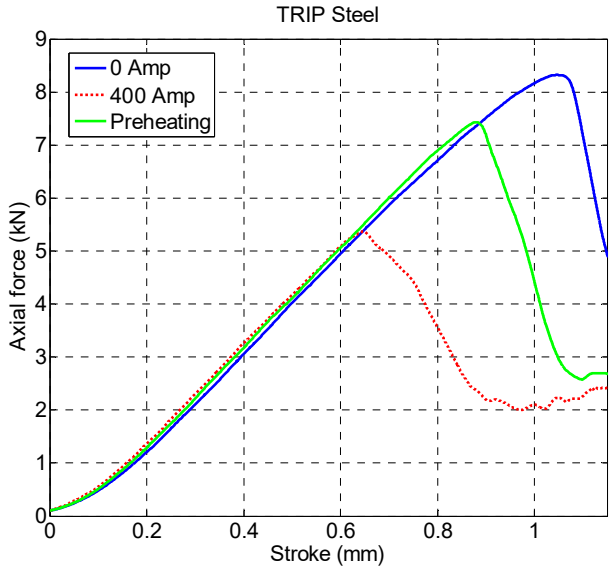

Figure 5-13 Comparison of axial force for TRIP 780 steel considering the thermal effect

5.3.3 Microstructure analysis

Since only the plunge stage is investigated in this study, a keyhole would be left on the specimen after extraction of the tool. The specimens are then sectioned at weld center along the thickness direction and observed under optical microscope. Figure 5-14 (a) shows an overview of half of the cross section of TRIP steel after electrically assisted plunging process. Based on the microstructure characteristics, the FSW weld section can be categorized into three zones [10]. The

region closest to the tool is the stirring zone (SZ), where fine grains exist due to the involved dynamic recrystallization process, which corresponds to Figure 5-14 (b). Next to the SZ is the thermal mechanically affected zone (TMAZ) where the materials experience a high temperature and large deformation, but the strain is insufficient to induce recrystallization, which generally results in relatively large and elongated grain structure. The TMAZ zone is not obvious in this plunge section of steel. Beyond the TMAZ is the heat affect zone (HAZ), where the materials only undergo thermal cycle and little amount of plastic deformation is involved, which corresponds to Figure 5-14 (d). Figure 5-14 (c) shows the transition region from stirring zone to heat affected zone.

Figure 5-15 shows the plunge section obtained from the non-electrically assisted condition. Similarly, Figure 5-15 (b) presents the stirring zone and Figure 5-15 (d) corresponds to the heat affected zone. Comparing Figure 5-15 (a) with Figure 5-14 (a), the size of the stirring zone is reduced after applying the electrical current. On the other hand, according to previous literature [165], the electrical current can help enhance dynamic recrystallization, which therefore should result in a larger stirring zone with refined grain size in the electrically assisted plunge condition. This difference is most likely due to the associated high temperature from Joule heating of steel, which facilitates the growth of the recrystallized grains and results in coarser structure.

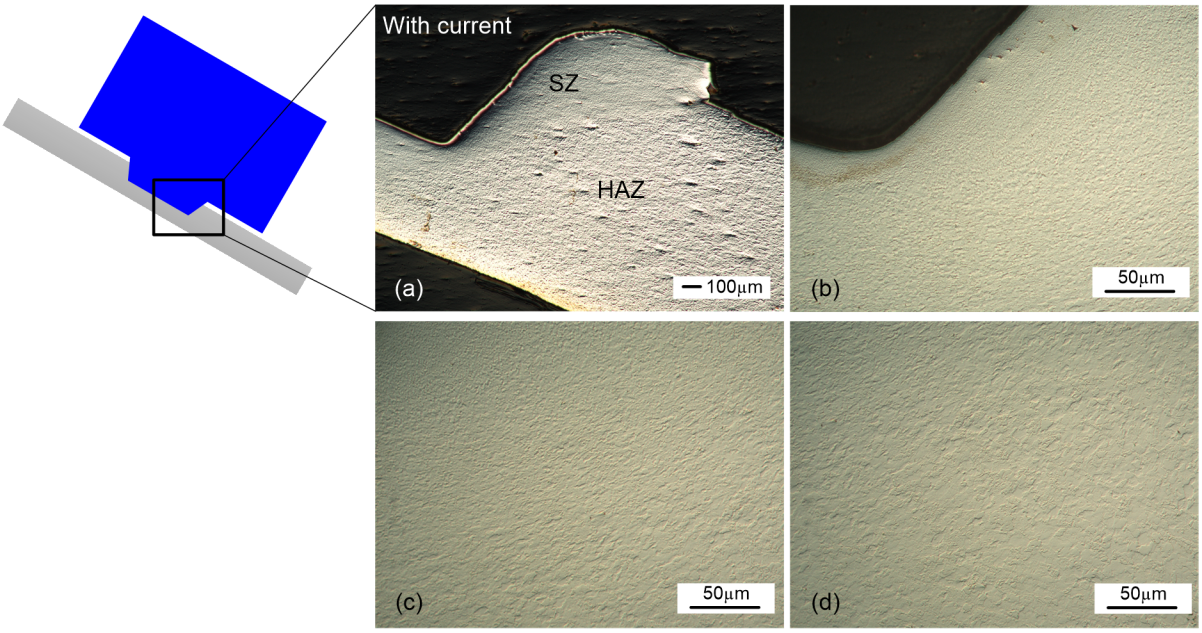

Figure 5-14 Plunge cross section under electrically assisted condition: (a) Overview; (b) SZ; (c) Transition between SZ and HAZ; (d) HAZ

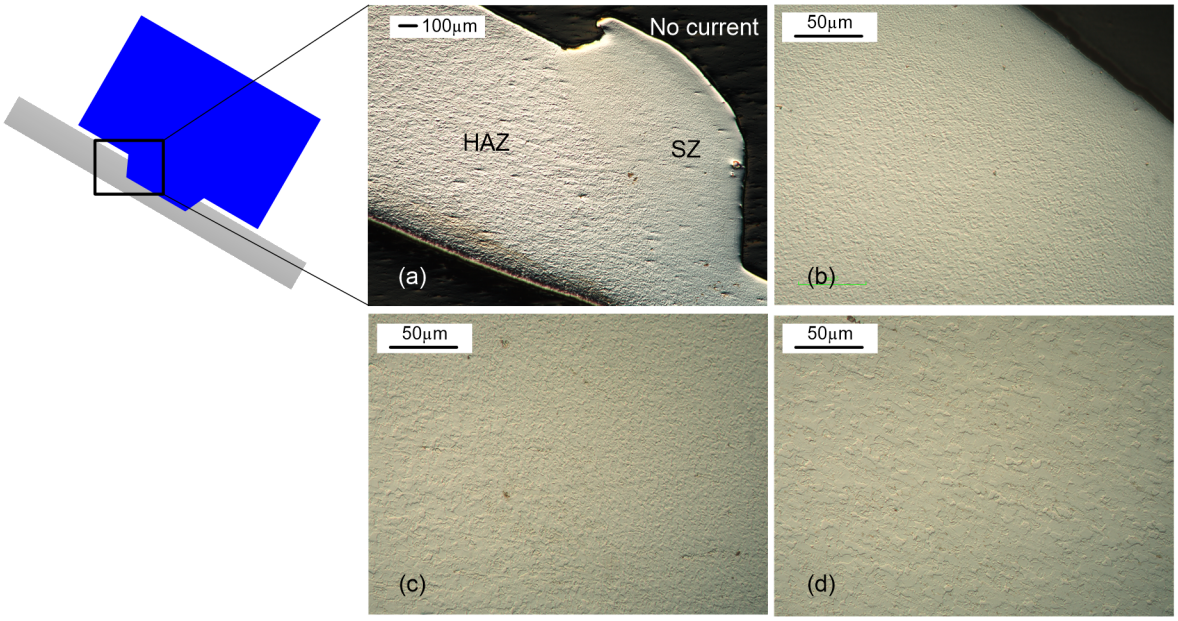

Figure 5-15 Cross section from traditional plunge process: (a) Overview; (b) SZ; (c) Transition between SZ and HAZ; (d) HAZ

5.4 Electrically assisted FSW for joining Al6061 to TRIP steel

5.4.1 Experimental specifications

Similar to the FSW configuration described in Chapter 3, steel is placed on the advancing side and the FSW tool is unsymmetrically shifted towards aluminum. The investigated welding conditions are listed in Table 5-1 and the welding speed was kept at 60mm/min in all the conditions. For temperature comparison between electrically assisted and conventional FSW processes, mica sheet is used as the insulation material. For mechanical welding force and subsequent Al-Fe interface microstructure analysis, ceramic block is used instead as the insulation material.

Table 5-1 Investigated welding conditions for comparison between hybrid and conventional friction stir welding processes

FSW condition	Rotational speed (R): rpm	Welding speed (v): mm/min	Tool offset (Offset) : mm	Input current: A
1	1200	60	1.03	0
				560
2	1200	60	1.63	0
				560
3	1800	60	1.03	0
				560
4	1800	60	1.63	0
				560

5.4.2 Welding temperature and force comparison

Figure 5-16 shows the thermal history results measured with the three thermocouples located below the weld seam, as described in Figure 5-3 (b). A good repeatability of temperature measurement can be achieved with this thermocouple configuration. However, insertion of mica sheet between workpiece and backing plate provides not only electrical but also thermal insulation. The highest temperature measured is less than 100°C, which is far below the actual temperature in weld zone. Notwithstanding that, these measurements can still help indicate the relative

significance of resistance heating. The thermocouple located below the plunge position, which is also the beginning position of the weld, has the highest temperature increasing gradient. This is the result of direct heating from friction and plastic deformation in plunge stage. The thermocouples located in the middle and end of weld experience a smaller temperature increasing gradient, since their initial temperature rise is due to thermal conduction as the tool approaches. The peak temperature at the plunge position is smaller than that in welding regions. This can be construed from the aspect that the total amount of heat generation in the beginning is smaller compared with that in the stable welding stage. This is especially true for electrically assisted conditions as the resistance heating will accumulate during the process until an equilibrium has reached. In the temperature profile measured by the thermocouple located at the end of the weld, a sharp apex can be observed, which is due to the retraction of tool and discontinuation of the current. The temperature then gradually drops off following natural cooling of the workpiece.

Figure 5-17 shows the electrical effects on the thermal history measured by the thermocouple located below the beginning position of the weld. In the first ten seconds, which is the period of the plunge stage, the effect of electrical current on the temperature profile is not obvious. After that, accumulated resistance heating results in an elevated temperature. Peak temperature in the non-electrically assisted conditions occurs at around 15s, which is the finishing time spot of the 5s dwell stage. In the electrically assisted conditions, the temperature continues to increase after the tool starts to translate along the weld seam. Besides, the temperature rise from electrical current is more substantial than that caused by varying rotational speed. At this beginning position of the weld, the amount of temperature increase due to electrical current is generally independent of tool rotating speed and offset.

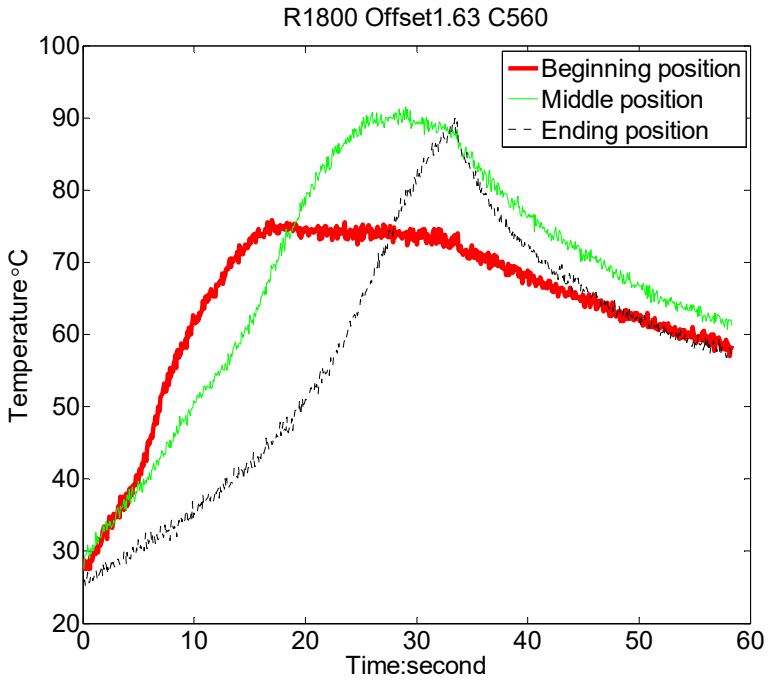

Figure 5-16 Thermal histories measured at the weld beginning, middle and ending position (1800 rpm; Tool offset: 1.63mm; 560 Amp)

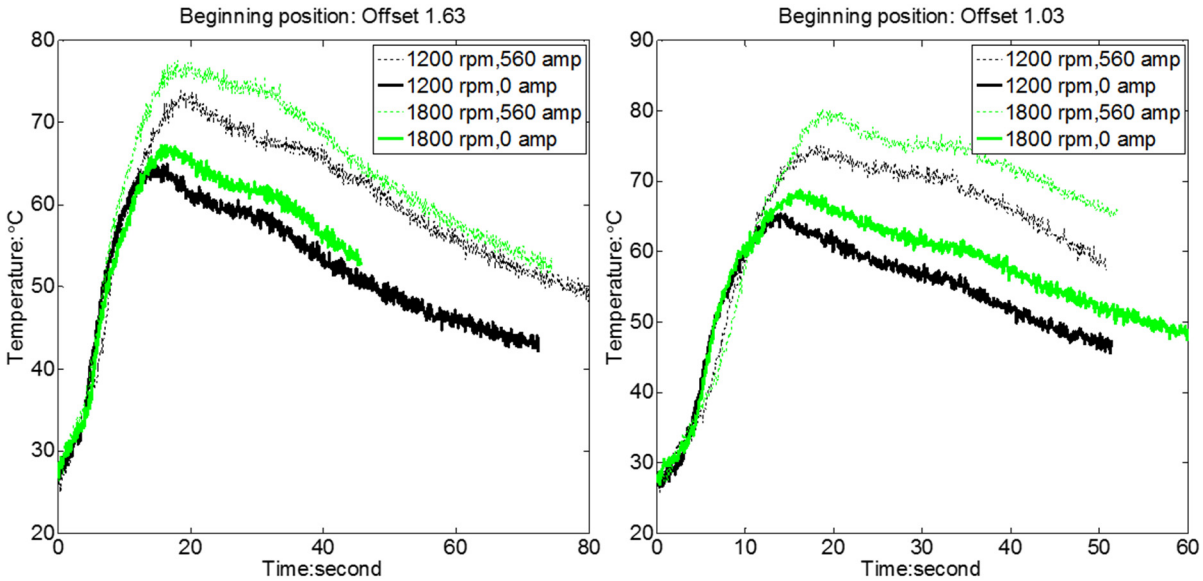

Figure 5-17 Comparison of the electrical effect on the thermal history of weld beginning point under different rotating speeds and tool offsets

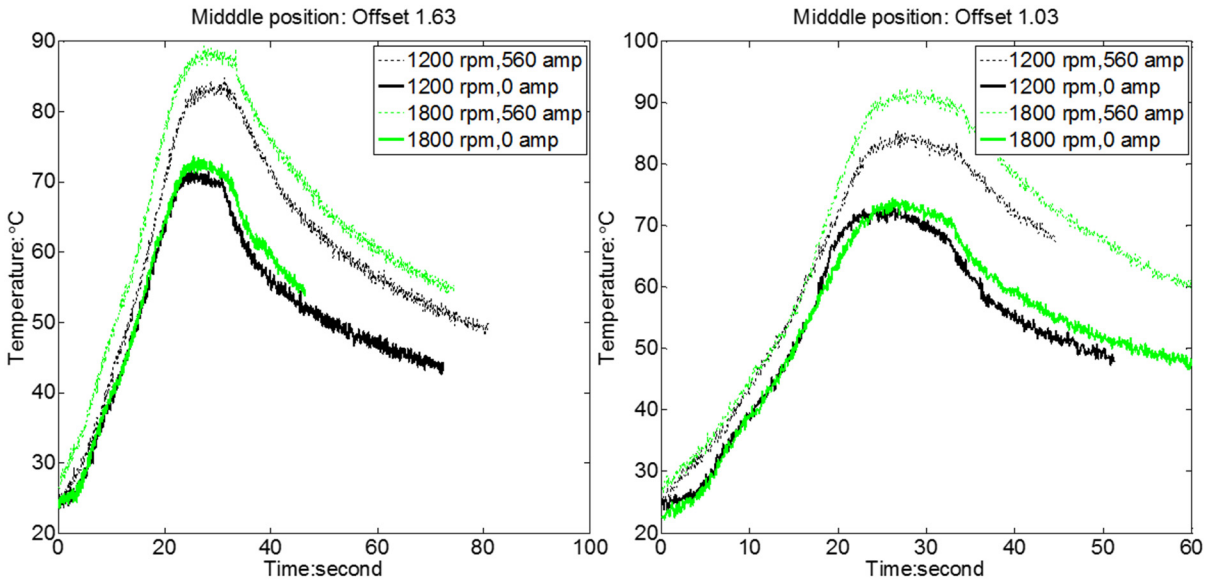

Figure 5-18 Comparison of the electrical effect on the thermal history of weld middle point under different rotating speeds and tool offsets

Figure 5-18 shows the electrical effects on the thermal history measured by the thermocouple located below the middle position of the weld. Similar to measurements at the beginning position of the weld, the electrical current raises the temperature and the temperature increase is higher due to the accumulation of resistance heating. With tool offset of 1.63mm, the maximum temperature increase from electrical current is around 16°C for the larger rotating speed of 1800rpm and 13°C for 1200rpm. With tool offset of 1.03mm, the maximum temperature increase is around 17°C for 1800rpm and 13°C for 1200rpm. The electrical current results in a higher temperature increase in the condition of a larger rotating speed. The energy of electrical current can be divided into two parts. One is for resistance heating and the rest is for direct material softening, i.e. the electro-plastic effect. Higher rotating speed corresponds to a larger strain rate, which according to Varma and Cornwell [35] weakens the electro-plastic effect. A larger portion of the electrical energy is therefore dissipated by resistance heating and results in a higher temperature rise. The effect of tool offset on the temperature increase is not obvious despite the fact that steel has a higher

electrical resistance and larger amount of steel is involved in the weld zone under a smaller tool offset condition. The fraction of electrical energy contributed to direct material softening is therefore possible to be increased from a smaller tool offset condition. The thermal history at the ending position of the weld, as shown in Figure 5-19, is overall the same as the result of weld middle point.

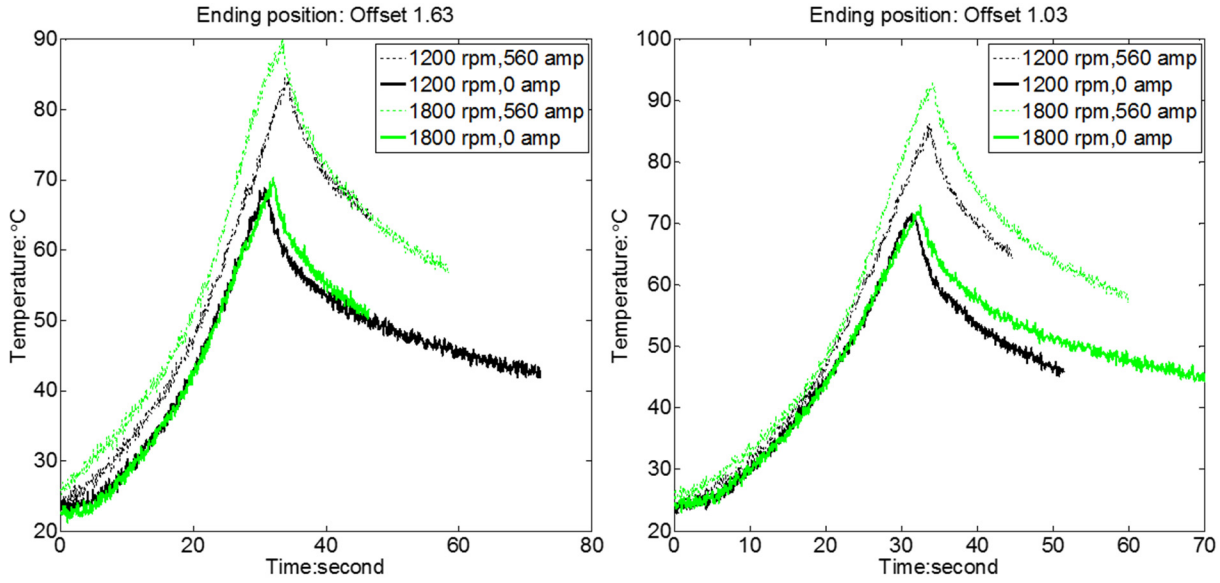

Figure 5-19 Comparison of the electrical effect on the thermal history of weld ending point under different rotating speeds and tool offsets

In the following studies, the mica sheet is replaced with ceramic block for welding force measurements and joint microstructure analysis. Figure 5-20 compares the axial welding force in conventional and electrically assisted FSW processes under various welding conditions. The axial force is consistently reduced, especially during the initial plunge stage. Greater amount of force reduction is obtained in the condition of a lower rotational speed. It indicates that larger fraction of the external electrical energy is attributed to direct material softening, which is consistent with the previous temperature measurements. In addition, the force reduction is more significant in a smaller tool offset condition. Based on the electrically assisted tensile test results for Al 6061 from

Andrawes et al. (2004) and for TRIP steel from Chapter 2, the electro-plastic softening is more effective for steel compared with aluminum under the same current density. Since more steel is deformed in the stirring zone in the condition of a smaller tool offset, it is reasonable to obtain a larger welding force reduction.

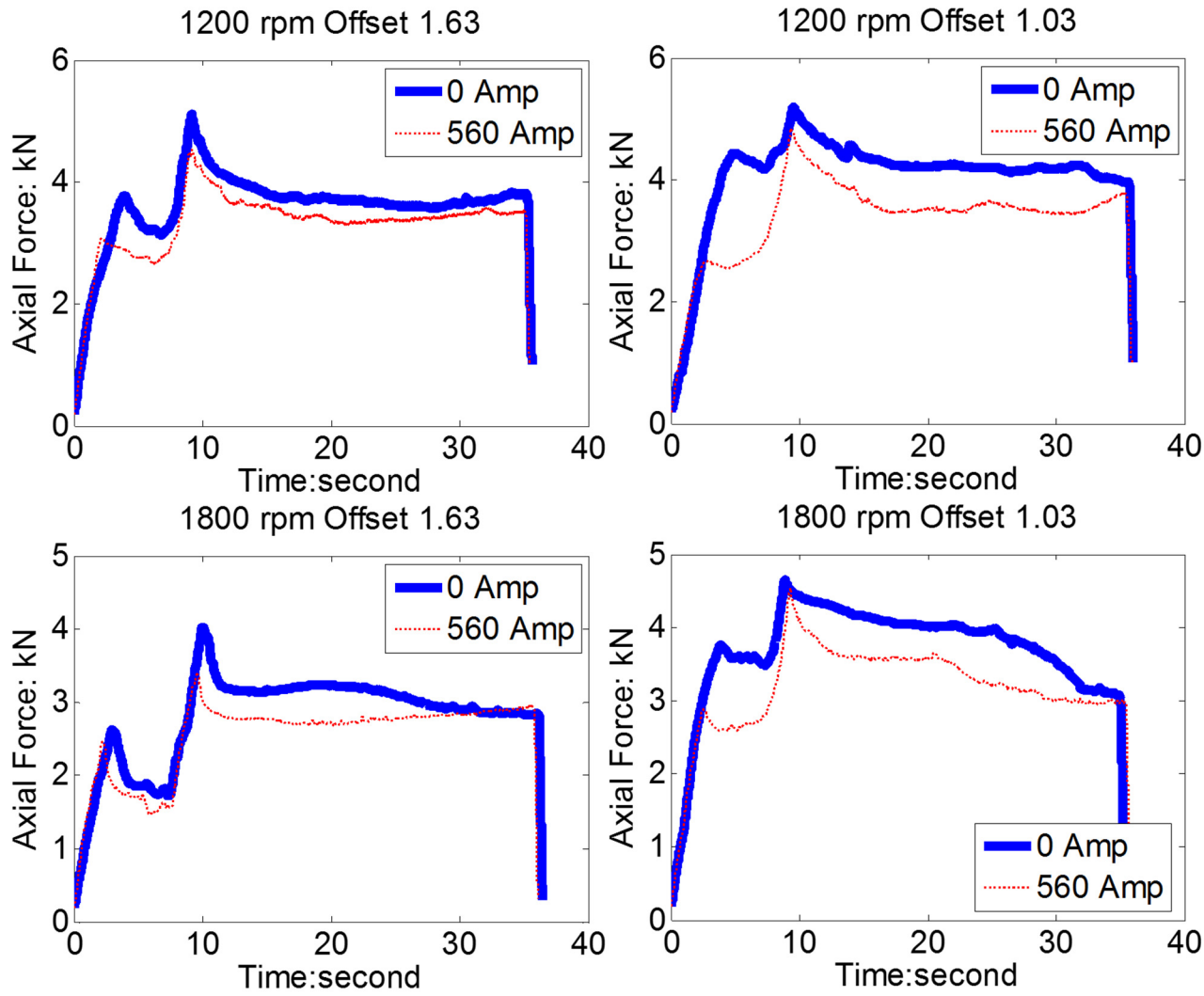

Figure 5-20 Axial force comparison under various processing conditions

5.4.3 Effect of the electrical current on the Al-Fe interface evolution

Considering the above welding force results, the axial force can be reduced in both plunge and welding stages, which is likely to affect the corresponding joint microstructure. Therefore for each welding condition, two metallurgical samples are prepared by sectioning the welds at the

plunge position and in the middle of the weld respectively. Figure 5-21 shows SEM images of the Al-Fe interface at the plunge section under a higher rotating speed of 1800 rpm. The top two figures correspond to a larger tool offset configuration and the right two correspond to electrically assisted conditions. When the tool is shifted more into aluminum, intermetallic compounds (IMC) is difficult to identify at some locations of the Al-Fe interface in conventional FSW process. This is possibly due to less amount of involved steel and lower pressure in the weld as well as the relatively lower temperature in the beginning of the weld. In comparison, continuous existence of IMC layer is observed after external current is applied.

In the smaller tool offset condition, a continuous IMC layer can be found for both conventional and hybrid processes, as shown in Figure 5-21 (c) and (d). In the electrically assisted condition, a thin slice of steel is connected to the base material and encompassed by an IMC layer. This feature is more pronounced at welding sections, as shown in Figure 5-22 (b) and (d). In contrast to a smooth IMC layer obtained from traditional FSW process, micro-interlock structures where steel and intermetallic compound are intermixed together are obtained after introducing electrical current. This micro-interlock feature is believed to be advantageous for joint strength, since crack propagation in the brittle IMC region can be effectively restrained by the surrounding steel, which has a much higher ductility. Similar structure were also observed by Xiong et al. [166] when they did friction stir lap joint between Al 1100 and 1Cr18Ni9Ti stainless steel using a tool with a cutting pin feature. Their joint shear strength was reported to be even higher than the base aluminum alloy, which was attributed to a thin IMC layer with mechanical bonding from micro-interlocks at the Al-Fe interface.

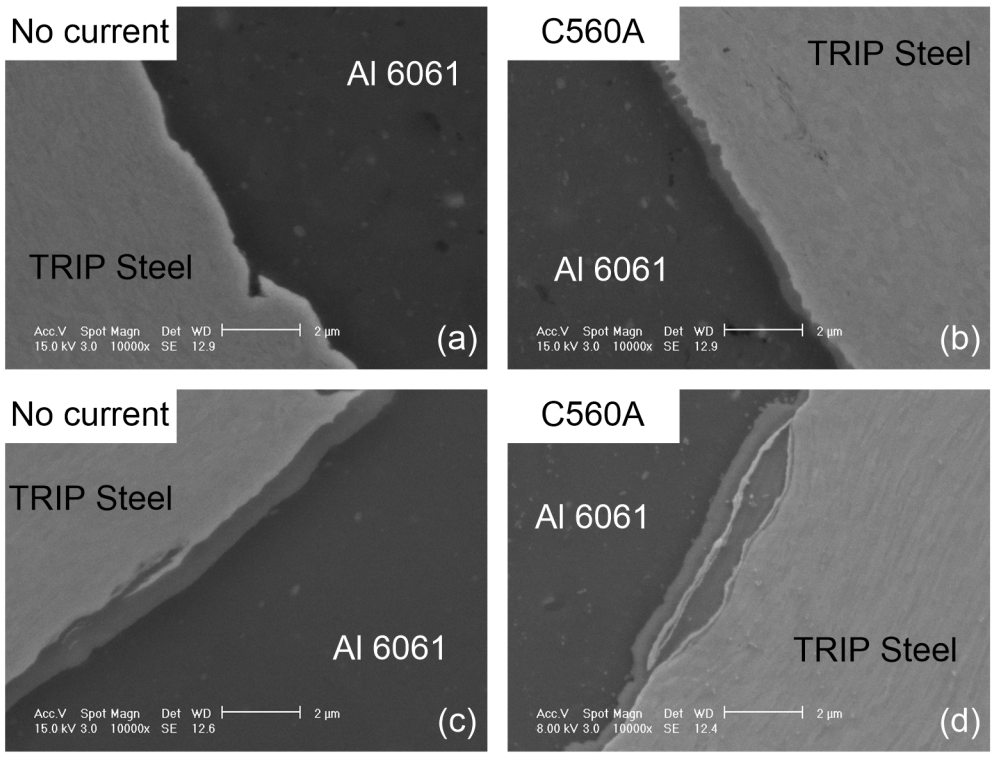

Figure 5-21 Al-Fe interface at plunge section (1800rpm): (a) Tool offset 1.63mm; (b) Tool offset 1.63mm with 560 Amp; (c) Tool offset 1.03mm; (d) Tool offset 1.03mm with 560 Amp

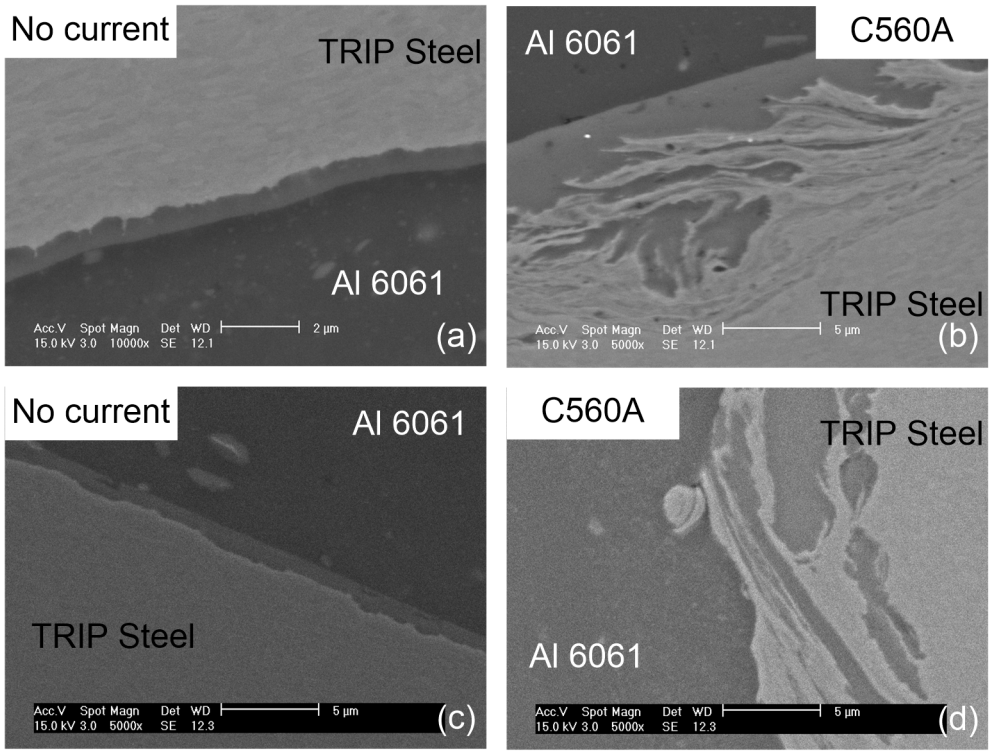

Figure 5-22 Al-Fe interface at weld section (1800 rpm): (a) Tool offset 1.63mm; (b) Tool offset 1.63mm with 560 Amp; (c) Tool offset 1.03mm; (d) Tool offset 1.03mm with 560 Amp

The effect of current on the size and morphology of the intermetallic compunds at Al-Fe interface for the plunge section can be considered from the electromigration effect. Formation and growth of the interfacial layer depends on two processes, which are interdiffusion of aluminum and iron atoms and reaction of these two elements. Diffusion of atoms can be enhanced with application of electrical current. Chen et al. [167] and Conrad et al. [41] expressed the flux of atoms driven by electrical current and chemical potential as the following:

$$J_i = \frac{-D_i N_i}{kT}\left(\mathrm{z}_i^* e\rho_e j + kT\frac{\partial \ln N_i}{\partial x}\right) \tag{5-1}$$

where the first term represents atomic flux induced by electrical current and the second term corresponds to atomic flux driven by composition gradient. D_i is the diffusion coefficient, N_i is the mole fraction of each element, T is the temperature, k is the Boltzman constant, z_i^* is the effective charge of atom, e is the charge per electron, ρ_e represents material electrical resistivity and j is the current density.

The significance of electric current effects on atom diffusion can be determined by comparing magnitudes of the two terms in the parentheses of equation (5-1) [168]. A simplified calculation is performed here assuming the composition of the interfacial layer is Fe_3Al. For Al atom, its concentration at Al/Fe_3Al interface and that at the Fe_3Al/Fe interface can be approximated based on the Al-Fe phase diagram, as shown in Figure 3-25. The temperature is estimated to be 0.8 of melting temperature of Aluminum and therefore the atomic concentrations of Al atom are 25% and 24% at the two boundaries. Within the intermetallic layer, which has a thickness of around 1 μm, the atomic concentration is assumed to vary linearly. Based on these assumptions, the Al atomic flux driven by composition gradient is roughly estimated to be $9.4\text{x}10^{-22}$/ μm. Similar procedure can be performed for Fe and the result is $2.97\text{x}10^{-22}$/ μm. Based on [169], the effective

charge of Al atom in solid solution is in the range of 12 to 30. The electrical resistivity of Fe_3Al is around 130×10^{-6} to 155×10^{-6} Ω-cm [170]. By substituting the current density j with 15A/mm^2 and averaged material properties into the first term in the parentheses of equation (5-1), the atomic flux of Al driven by electrical current is roughly 1.48×10^{-22}/ μm, which is around 16% of the flux driven by the composition gradient. For Fe, its effective charge is 2 [169] and the atomic flux driven by electrical current is roughly 1.50×10^{-23}/ μm, which is around 5% of that from composition gradient.

Besides the additional atom flux from electrical field, the associated higher temperature from electrical resistance heating can directly increase D_i and therefore the diffusion rate. Moreover, the external electrical energy can help reduce the activation energy for reaction, which will further enhance the formation and growth of the interlayer. Figure 5-23 and Figure 5-24 show the Al-Fe interface at plunge and welding sections under a lower rotating speed of 1200 rpm. Despite an overall thinner interfacial layer, the results are similar to that from higher rotating speed conditions.

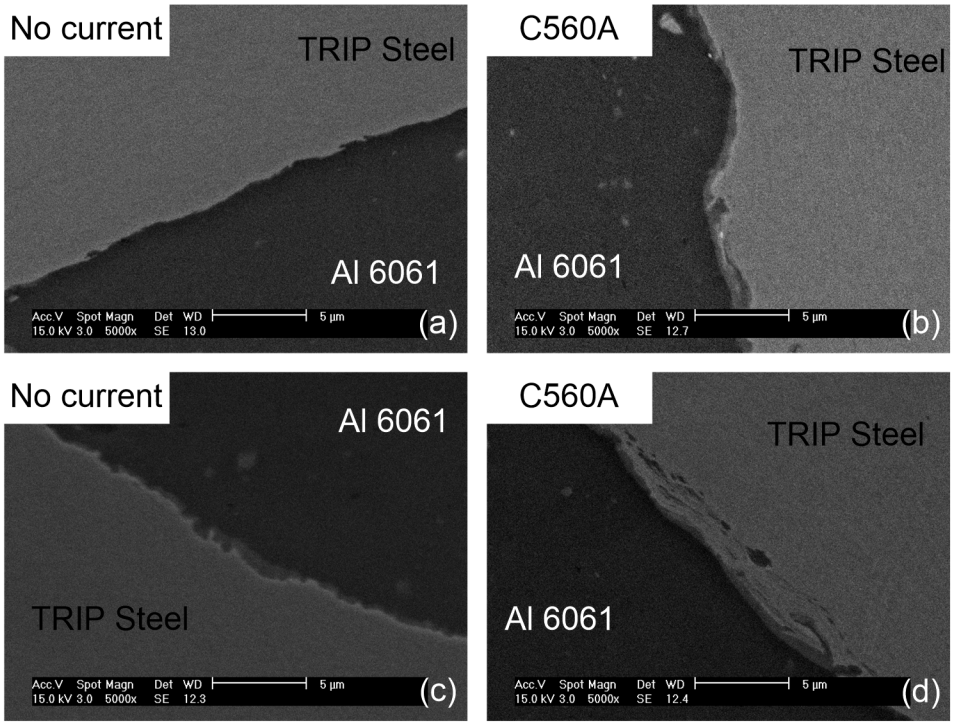

Figure 5-23 Al-Fe interface at plunge section (1200rpm): (a) Tool offset 1.63mm; (b) Tool offset 1.63mm with 560 Amp; (c) Tool offset 1.03mm; (d) Tool offset 1.03mm with 560 Amp

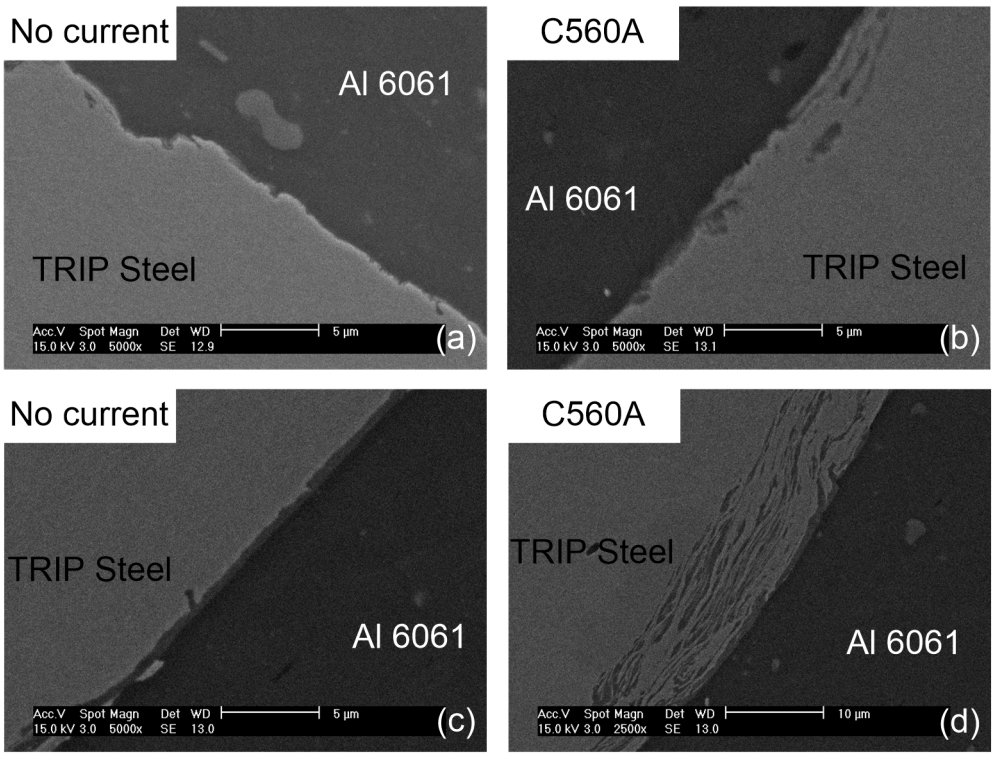

Figure 5-24 Al-Fe interface at weld section (1200 rpm): (a) Tool offset 1.63mm; (b) Tool offset 1.63mm with 560 Amp; (c) Tool offset 1.03mm; (d) Tool offset 1.03mm with 560 Amp

5.5 Summaries and conclusions

In this Chapter, an electrically assisted friction stir welding system was designed and developed. The FSW tool is only passively involved in the electrical circuit and the system can be applied to thin sheet metals of various sizes. Based on this experimental system, plunge stage of FSW was studied for both aluminum alloy Al 6061 and TRIP 780 steel respectively. An effective reduction of the axial welding force was obtained with a good repeatability. Associated Joule heating effect for steel was considered from an additional preheating test. Apart from the thermal softening, approximately 2/3 of the force reduction can be attributed to the direct softening from electro-plastic effect. The electrical current was then applied to the entire welding process for Al 6061 to TRIP steel. The axial welding force was consistently reduced under various weld conditions. Based on the temperature measurements, the force reduction came from synergic

effects of electro-plasticity and Joule heating. The first factor was more significant when the rotating speed was small or the tool was less shifted to aluminum. Regarding the Al-Fe interface of the welds, the electrical current showed to enhance the formation of the thin intermetallic layer and micro-interlock features.

CHAPTER 6

CONCLUSIONS AND FUTURE WORK

6.1 Conclusions

This research focuses on a hybrid friction stir welding process for joining Al 6061 to TRIP steel based on the electro-plastic effect. Works have been performed in four major areas, including the study of electro-plastic effect, experimental investigation on FSW of Al 6061 to TRIP steel, analytical and numerical modeling of dissimilar FSW process and study of electrically assisted FSW for joining Al 6061 to TRIP steel. Major achievements are summarized as follows:

(1) A hypothesis was proposed for explaining the mechanisms of electro-plastic effect: The high density electrical current can heat up local material strengthening sites due to their higher electrical resistivity, which promotes dislocations to bypass these obstacles without temperature increase of the bulk material.

(2) The electro-plastic effect was observed on one type of advanced high strength steel, TRIP 780/800 by varying the electrical current conditions during tensile tests. Based on XRD analysis, the electrical pulses showed to retard martensitic phase transformation that is associated with the plastic deformation of TRIP steel.

(3) Successful joints between Al 6061 alloy and TRIP steel were able to be achieved from friction stir welding process, where the steel needed to be placed in the advancing side. The highest joint strength reached 85% of the base aluminum alloy and the tensile specimen failed at the heat affected zone of aluminum. On the other hand, a stirred over steel strip embedded in the aluminum matrix was shown to be detrimental to joint quality. Small steel fragments encompassed by intermetallic layer and intermetallic particles were formed in the weld nugget due to the stirring action of the tool, which were shown to be acceptable for tensile strength but might be harmful for fatigue life.

(4) A thin intermetallic layer with the thickness of around 1 μm was formed at the Al-Fe interface in the advancing side. The composition and thickness of this layer closely depended on the weld conditions through the temperature field and welding force. Higher rotating speed elevated the overall temperature in the weld and reduced the required axial and lateral welding force. Shifting the tool more towards aluminum side also decreased the welding force. However, the maximum value of tool offset needed to be controlled for sufficient amount of steel in the weld nugget to achieve effective bonding between aluminum and steel. Varying welding speed from 30mm/min to 120mm/min under the rotating speeds of 1200rpm and 1800rpm had an insignificant effect on mechanical welding force or temperature distribution but directly changed the length of thermal history and accordingly the thickness of the intermetallic layer.

(5) A model for the transient plunge stage of the dissimilar material friction stir welding process can be obtained by: (a) Introducing the field variable α to identify the regions of steel and aluminum and define generalized material properties; (b) Developing a separate set of conservation equations at the two materials interface to account for the discontinuities.

Calculation of the model was performed in the ABAQUS software, which yielded reasonable agreement with experimental findings in the aspect of welding force and material distribution;

(6) A model for the stable welding stage of the dissimilar material friction stir welding process can be developed based on Eulerian formulation with multiple phase flow theories and volume of fluid method, where the pressure, velocity and temperature fields are shared and material properties are averaged based on the volume fraction of different materials. In addition, to predict reasonable temperature and material distributions, an appropriate shear stress boundary needs to be applied at the tool contact area instead of the velocity boundary condition. The developed model captured the macrostructure feature of the embedded steel strip in aluminum side, which was experimentally observed in the weld cross sections. The model also revealed that the slipping condition prevailed at the tool-workpiece interface.

(7) The developed electrically assisted friction stir welding system was shown to be capable of applying high density electrical current into the FSW process. The axial welding force was consistently reduced under various weld conditions, especially during the plunge stage. A preheating test showed that apart from thermal effect, approximately 2/3 of the force reduction in the plunge stage of TRIP steel was attributed to the electro-plastic softening. Based on temperature measurements during welding stage, the force reduction came from synergic effects of both electro-plasticity and Joule heating. The relative significance of each factor dependent on weld conditions. In addition to reducing the welding force, the electrical current enhanced formation of the thin IMC layer and micro-interlock structures at the Al-Fe interface of the joints.

6.2 Future work

Reliable and economical dissimilar material joining is always desirable since it enables a suitable combination of different materials based on each of their own advantageous properties. This work studies the mechanisms and principles of FSW of aluminum alloy to advanced high strength steel. Electrical current is further incorporated for process improvement. Some possible directions for future research are suggested as followings:

(1) Despite these indirect supports from literature, further experiment should be performed in microscopic scale for direct validation of the hypothesis that explains the underlying principles of electro-plastic effect. For example, an in-situ TEM tensile test which can directly observe motion of dislocations and other devices that can simultaneously measure the temperature distribution.

(2) Extend the hybrid friction stir welding to friction stir spot welding process. This newly developed process can be considered as a combination of resistance spot welding process with lower required electrical energy and friction stir spot welding process with smaller welding force and faster welding speed. Workpiece of different thickness can be spot welded. A schematic illustration of the hybrid friction stir spot welding process compared with traditional resistance spot welding is shown in Figure 6-1.

(3) Incorporate the electro-plastic effect into the material constitutive law for hybrid FSW modeling. A modified Johnson-Cook or Sheppard-Wright material model needs to be developed with current density as an additional input parameter. During hybrid FSW modeling, the electrical field is calculated first, which can be then applied as a predefined field for following simulation of the welding process. Alternatively, a multiphysical model which couples thermal, mechanical and electrical fields can be developed.

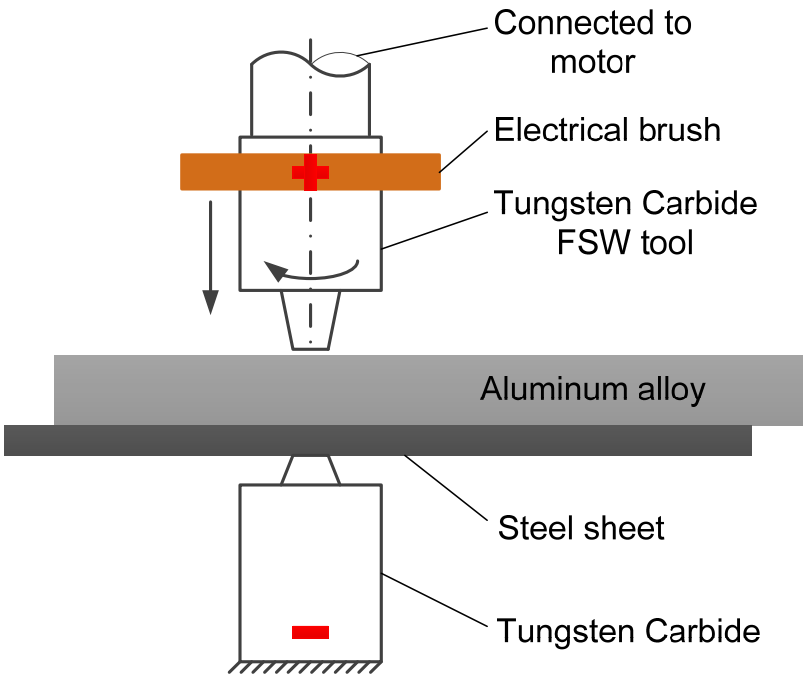

Figure 6-1 Schematic illustration of the hybrid friction stir resistance spot welding process

(4) Design and improve friction stir welding tool. In order to eliminate the stirred over steel strip as shown in the joint cross sections, the shape and dimensions of the current FSW tool can be further improved. On the tool shoulder surface, groove features and a concave shape can be applied to preserve the material from splashing out. On the tool pin, threads can be developed to help promote material flow in the vertical direction. The radius of pin and shoulder can be adjusted to modify the heat generation and the stirring shear force.

(5) Study interfacial structure for dissimilar material joint strength. As shown in chapter 3, an intermetallic compound (IMC) layer with appropriate thickness is likely to improve the joint strength. On the other hand, it is anticipated that too much IMC will directly jeopardize joint quality. Relationship between thickness and compositions of the IMC layer and the joint strength needs to be studied. If possible, these microstructure features can be related to macroscopic material parameters for joint strength and failure modes modeling, for example, the characteristic strength and toughness in cohesive models.

(6) Investigate the corrosive issue of Al-Fe joint. Corrosion has generally been identified for direct welds between aluminum and steel. In order for improvements, some protective layer, such as adhesives, can be applied before joining the two materials together. Behavior of the joint can then be evaluated in a corrosive environment.

BIBLIOGRAPHY

[1] Kuziak, R., Kawalla, R., and Waengler, S., 2008, "Advanced high strength steels for automotive industry," Archives of Civil and Mechanical Engineering, 8(2), pp. 103-17.
[2] Sakiyama, T., Murayama, G., Naito, Y., Saita, K., Oikawa, Y. M. H., and Nose, T., 2013, "Dissimilar Metal Joining Technologies for Steel Sheet and Aluminum Alloy Sheet in Auto Body," Nippon steel technical report.
[3] Kannatey-Asibu, E., 2009, Principles of laser materials processing, John Wiley & Sons Inc.
[4] Ogura, T., Saito, Y., Nishida, T., Nishida, H., Yoshida, T., Omichi, N., Fujimoto, M., and Hirose, A., 2012, "Partitioning evaluation of mechanical properties and the interfacial microstructure in a friction stir welded aluminum alloy/stainless steel lap joint," Scripta Materialia.
[5] Das, H., Basak, S., Das, G., and Pal, T. K., 2013, "Influence of energy induced from processing parameters on the mechanical properties of friction stir welded lap joint of aluminum to coated steel sheet," The International Journal of Advanced Manufacturing Technology, 64(9-12), pp. 1653-61.
[6] Movahedi, M., Kokabi, A. H., Seyed Reihani, S. M., Cheng, W. J., and Wang, C. J., 2013, "Effect of annealing treatment on joint strength of aluminum/steel friction stir lap weld," Materials & Design, 44(0), pp. 487-92.
[7] Movahedi, M., Kokabi, A., Reihani, S., and Najafi, H., 2012, "Effect of tool travel and rotation speeds on weld zone defects and joint strength of aluminium steel lap joints made by friction stir welding," Science and Technology of Welding & Joining, 17(2), pp. 162-67.
[8] Uematsu, Y., Kakiuchi, T., Tozaki, Y., and Kojin, H., 2012, "Comparative study of fatigue behaviour in dissimilar Al alloy/steel and Mg alloy/steel friction stir spot welds fabricated by scroll grooved tool without probe," Science and Technology of Welding & Joining, 17(5), pp. 348-56.
[9] Thomas, W., 1991, "Friction stir butt welding," International Patent Application No. PCT/GB92/0220.
[10] Mishra, R. S., and Ma, Z. Y., 2005, "Friction stir welding and processing," Materials Science and Engineering: R: Reports, 50(1-2), pp. 1-78.
[11] Flores, O. V., Kennedy, C., Murr, L., Brown, D., Pappu, S., Nowak, B. M., and McClure, J., 1998, "Microstructural issues in a friction-stir-welded aluminum alloy," Scripta Materialia, 38(5), pp. 703-08.
[12] Lienert, T., Stellwag Jr, W., Grimmett, B., and Warke, R., 2003, "Friction stir welding studies on mild steel," Welding journal, 82(1), pp. 1-9.
[13] Thomas, W., Threadgill, P., and Nicholas, E., 1999, "Feasibility of friction stir welding steel," Science and Technology of Welding & Joining, 4(6), pp. 365-72.
[14] Mandal, S., and Williamson, K., 2006, "A thermomechanical hot channel approach for friction stir welding," Journal of materials processing technology, 174(1), pp. 190-94.
[15] Uzun, H., Dalle Donne, C., Argagnotto, A., Ghidini, T., and Gambaro, C., 2005, "Friction stir welding of dissimilar Al 6013-T4 To X5CrNi18-10 stainless steel," Materials & Design, 26(1), pp. 41-46.
[16] Ghosh, M., Kar, A., Kumar, K., and Kailas, S., 2012, "Structural characterisation of reaction zone for friction stir welded aluminium-stainless steel joint," Materials Technology: Advanced Performance Materials, 27(2), pp. 169-72.

[17] Tanaka, K., Kumagai, M., and Yoshida, H., 2006, "Dissimilar joining of aluminum alloy and steel sheets by friction stir spot welding," Journal - Japan institute of light metals, 56(6), p. 317.
[18] Tanaka, T., Morishige, T., and Hirata, T., 2009, "Comprehensive analysis of joint strength for dissimilar friction stir welds of mild steel to aluminum alloys," Scripta Materialia, 61(7), pp. 756-59.
[19] Lee, W.-B., Schmuecker, M., Mercardo, U. A., Biallas, G., and Jung, S.-B., 2006, "Interfacial reaction in steel–aluminum joints made by friction stir welding," Scripta Materialia, 55(4), pp. 355-58.
[20] Dehghani, M., Amadeh, A., and Akbari Mousavi, S., 2013, "Investigations on the Effects of Friction Stir Welding Parameters on Intermetallic and Defect Formation in Joining Aluminum Alloy to Mild Steel," Materials & Design.
[21] Chen, C. M., and Kovacevic, R., 2004, "Joining of Al 6061 alloy to AISI 1018 steel by combined effects of fusion and solid state welding," International Journal of Machine Tools and Manufacture, 44(11), pp. 1205-14.
[22] Kovacevic, R., and Jiang, W. H., 2004, "Feasibility study of friction stir welding of 6061-T6 aluminium alloy with AISI 1018 steel," Proceedings of the Institution of Mechanical Engineers, Part B: Journal of Engineering Manufacture, 218(10), pp. 1323-31.
[23] Chen, T., 2009, "Process parameters study on FSW joint of dissimilar metals for aluminum–steel," Journal of Materials Science, 44(10), pp. 2573-80.
[24] Ross, C. D., Kronenberger, T. J., and Roth, J. T., 2009, "Effect of dc on the Formability of Ti--6Al--4V," Journal of Engineering Materials and Technology, 131(3), pp. 031004-11.
[25] Zhang, D., To, S., Zhu, Y., Wang, H., and Tang, G., 2012, "Dynamic Electropulsing Induced Phase Transformations and Their Effects on Single Point Diamond Turning of AZ91 Alloy," Journal of Surface Engineered Materials and Advanced Technology, 2(1), pp. 16-21.
[26] Yang, D., and Conrad, H., 2001, "Exploratory study into the effects of an electric field and of high current density electropulsing on the plastic deformation of TiAl," Intermetallics, 9(10), pp. 943-47.
[27] Andrawes, J. S., Heigel, J. C., Roth, J. T., and Warley, R. L., "Effects of DC Current on the Stress-Strain Curve and Hardness of 6061 T6511 Aluminum," Proc. ASME Conference Proceedings, ASME, pp. 169-78.
[28] Ross, C. D., Irvin, D. B., and Roth, J. T., 2007, "Manufacturing aspects relating to the effects of direct current on the tensile properties of metals," Journal of Engineering Materials and Technology, 129, p. 342.
[29] Dzialo, C., Siopis, M., Kinsey, B., and Weinmann, K., 2010, "Effect of current density and zinc content during electrical-assisted forming of copper alloys," CIRP Annals-Manufacturing Technology, 59(1), pp. 299-302.
[30] Mai, J., Peng, L., Lin, Z., and Lai, X., 2011, "Experimental study of electrical resistivity and flow stress of stainless steel 316L in electroplastic deformation," Materials Science and Engineering: A, 528(10–11), pp. 3539-44.
[31] Okazaki, K., Kagawa, M., and Conrad, H., 1979, "Additional results on the electroplastic effect in metals," Scripta Metallurgica, 13, pp. 277-80.
[32] Sprecher, A., Mannan, S., and Conrad, H., 1986, "Overview no. 49:: On the mechanisms for the electroplastic effect in metals," Acta Metallurgica, 34(7), pp. 1145-62.
[33] Cao, W., Sprecher, A., and Conrad, H., 1989, "Effect of strain rate on the electroplastic effect in Nb," Scr. Metall.;(United States), 23(1).
[34] Okazaki, K., Kagawa, M., and Conrad, H., 1979, "Effects of strain rate, temperature and interstitial content on the electroplastic effect in titanium," Scripta Metallurgica, 13, pp. 473-77.
[35] Varma, S., and Cornwell, L., 1979, "The electroplastic effect in aluminum," Scripta Metallurgica, 13(8), pp. 733-38.
[36] Okazaki, K., Kagawa, M., and Conrad, H., 1978, "A study of the electroplastic effect in metals," Scr. Metall., 12(11), pp. 1063-68.
[37] Xu, Q., Guan, L., Jiang, Y., Tang, G., and Wang, S., 2010, "Improved plasticity of Mg-Al-Zn alloy by electropulsing tension," Materials Letters, 64(9), pp. 1085-87.
[38] Zhu, Y., To, S., and Liu, X., 2011, "Use of EBSD to study electropulsing induced reverse phase transformations in a Zn–Al alloy (ZA22)," Journal of Microscopy, 242(1), pp. 62-69.

[39] To, S., Zhu, Y., Lee, W., Liu, X., Jiang, Y., and Tang, G., 2009, "Effects of current density on electropulsing-induced phase transformations in a Zn–Al based alloy," Applied Physics A: Materials Science & Processing, 96(4), pp. 939-44.
[40] Jiang, Y., Tang, G., Shek, C., Zhu, Y., and Xu, Z., 2009, "On the thermodynamics and kinetics of electropulsing induced dissolution of β-$Mg_{17}Al_{12}$ phase in an aged Mg–9Al–1Zn alloy," Acta Materialia, 57(16), pp. 4797-808.
[41] Conrad, H., 2000, "Effects of electric current on solid state phase transformations in metals," Materials Science and Engineering: A, 287(2), pp. 227-37.
[42] Troitskii, O., and Likhtman, V., 1963, "The anisotropy of the action of electron and radiation on the deformation of zinc single crystal in the brittle state," Kokl. Akad. Nauk, 148, pp. 332-34.
[43] Andrawes, J. S., Heigel, J. C., Roth, J. T., and Warley, R. L., "Effects of DC Current on the Stress-Strain Curve and Hardness of 6061 T6511 Aluminum," ASME.
[44] Mai, J., Peng, L., Lin, Z., and Lai, X., 2011, "Experimental study of electrical resistivity and flow stress of stainless steel 316L in electroplastic deformation," Materials Science and Engineering: A.
[45] Salandro, W. A., Jones, J. J., McNeal, T. A., Roth, J. T., Hong, S. T., and Smith, M. T., 2010, "Formability of Al 5xxx Sheet Metals Using Pulsed Current for Various Heat Treatments," Journal of manufacturing science and engineering, 132, p. 051016.
[46] Conrad, H., 1989, "A Study Into the Mechanism (s) for the Electroplastic Effect in Metals and Its Application to Metalworking, Processing and Fatigue," DTIC Document.
[47] Kuang, J., Du, X., Li, X., Yang, Y., Luo, A. A., and Tang, G., 2016, "Athermal influence of pulsed electric current on the twinning behavior of Mg–3Al–1Zn alloy during rolling," Scripta Materialia, 114, pp. 151-55.
[48] Conrad, H., Guo, Z., and Sprecher, A., 1989, "Effect of an electric field on the recovery and recrystallization of al and Cu," Scripta Metallurgica, 23(6), pp. 821-24.
[49] Xu, Z., Tang, G., Tian, S., Ding, F., and Tian, H., 2007, "Research of electroplastic rolling of AZ31 Mg alloy strip," Journal of Materials Processing Technology, 182(1), pp. 128-33.
[50] Zhen, S., Zu, H., and Yong, X., 1988, "Effect of Electric Current on the Recrystallization Behaviour of Cold Worked alpha-Ti," Scripta Metallurgica, 22(2), pp. 187-90.
[51] Lu, X.-P., Cao, W.-D., Sprecher, A., and Conrad, H., 1992, "Influence of an external electric field on the microstructure of superplastically deformed 7475 Al," Journal of Materials Science, 27(8), pp. 2243-50.
[52] Bunget, C., Salandro, W., Mears, L., and Roth, J. T., 2010, "Energy-based modeling of an electrically-assisted forging process," Trans. North Am. Manuf. Res. Inst. SME, 38, pp. 647-54.
[53] Salandro, W. A., Bunget, C., and Mears, L., 2011, "Electroplastic Modeling of Bending Stainless Steel Sheet Metal Using Energy Methods," Journal of manufacturing science and engineering, 133, p. 041008.
[54] Salandro, W. A., Bunget, C. J., and Mears, L., 2012, "A thermal-based approach for determining electroplastic characteristics," Proceedings of the Institution of Mechanical Engineers, Part B: Journal of Engineering Manufacture.
[55] Troitskii, O., 1969, "Electromechanical effect in metals," ZhETF Pis ma Redaktsiiu, 10, p. 18.
[56] Yao, K. F., Wang, J., Zheng, M., Yu, P., and Zhang, H., 2001, "A research on electroplastic effects in wire-drawing process of an austenitic stainless steel," Scripta Materialia, 45(5), pp. 533-40.
[57] Salandro, W. A., Jones, J. J., McNeal, T. A., Roth, J. T., Hong, S. T., and Smith, M. T., "Effect of electrical pulsing on various heat treatments of 5XXX series aluminum alloys," Proc. Int. Manuf. Sci. & Engr. Conf, p. 10.
[58] Perkins, T. A., Kronenberger, T. J., and Roth, J. T., 2007, "Metallic forging using electrical flow as an alternative to warm/hot working," Journal of manufacturing science and engineering, 129, p. 84.
[59] Siopis, M. S., and Kinsey, B. L., 2010, "Experimental Investigation of Grain and Specimen Size Effects During Electrical-Assisted Forming," Journal of manufacturing science and engineering, 132, p. 021004.
[60] Fan, R., Magargee, J., Hu, P., and Cao, J., 2013, "Influence of grain size and grain boundaries on the thermal and mechanical behavior of 70/30 brass under electrically-assisted deformation," Materials Science and Engineering: A, 574, pp. 218-25.

[61] Kir'yanchev, N. E., Troitskii, O. A., and Klevtsur, S. A., 1983, "Electroplastic deformation of metals (review)," Strength of Materials, 15(5), pp. 709-15.
[62] Prüger, S., Seupel, A., and Kuna, M., 2014, "A thermomechanically coupled material model for TRIP-steel," International Journal of Plasticity, 55, pp. 182-97.
[63] Iwamoto, T., 2004, "Multiscale computational simulation of deformation behavior of TRIP steel with growth of martensitic particles in unit cell by asymptotic homogenization method," International Journal of Plasticity, 20(4–5), pp. 841-69.
[64] Kang, S. H., and Im, Y. T., 2007, "Thermo-elasto-plastic finite element analysis of quenching process of carbon steel," Journal of Materials Processing Technology, 192–193, pp. 381-90.
[65] Zaefferer, S., Ohlert, J., and Bleck, W., 2004, "A study of microstructure, transformation mechanisms and correlation between microstructure and mechanical properties of a low alloyed TRIP steel," Acta Materialia, 52(9), pp. 2765-78.
[66] Jacques, P., Furnémont, Q., Mertens, A., and Delannay, F., 2001, "On the sources of work hardening in multiphase steels assisted by transformation-induced plasticity," Philosophical Magazine A, 81(7), pp. 1789-812.
[67] Olson, G., and Cohen, M., 1975, "Kinetics of strain-induced martensitic nucleation," Metallurgical and Materials Transactions A, 6(4), pp. 791-95.
[68] Richman, R., and Bolling, G., 1971, "Stress, deformation, and martensitic transformation," Metallurgical and Materials Transactions B, 2(9), pp. 2451-62.
[69] Fahr, D., 1971, "Stress- and strain-induced formation of martensite and its effects on strength and ductility of metastable austenitic stainless steels," Metallurgical Transactions, 2(7), pp. 1883-92.
[70] Curtze, S., Kuokkala, V. T., Hokka, M., and Peura, P., 2009, "Deformation behavior of TRIP and DP steels in tension at different temperatures over a wide range of strain rates," Materials Science and Engineering: A, 507(1), pp. 124-31.
[71] Lee, C. Y., Choi, D. H., Yeon, Y. M., and Jung, S. B., 2009, "Dissimilar friction stir spot welding of low carbon steel and Al-Mg alloy by formation of IMCs," Science and Technology of Welding & Joining, 14(3), pp. 216-20.
[72] Yılmaz, M., Çöl, M., and Acet, M., 2002, "Interface properties of aluminum/steel friction-welded components," Materials Characterization, 49(5), pp. 421-29.
[73] Bozzi, S., Helbert-Etter, A., Baudin, T., Criqui, B., and Kerbiguet, J., 2010, "Intermetallic compounds in Al 6016/IF-steel friction stir spot welds," Materials Science and Engineering: A, 527(16), pp. 4505-09.
[74] Kimapong, K., and Watanabe, T., 2005, "Effect of welding process parameters on mechanical property of FSW lap joint between aluminum alloy and steel," Materials transactions, 46(10), pp. 2211-17.
[75] Chen, Y., Komazaki, T., Tsumura, T., and Nakata, K., 2008, "Role of zinc coat in friction stir lap welding Al and zinc coated steel," Materials Science and Technology, 24(1), pp. 33-39.
[76] Chen, Y. C., Komazaki, T., Kim, Y. G., Tsumura, T., and Nakata, K., 2008, "Interface microstructure study of friction stir lap joint of AC4C cast aluminum alloy and zinc-coated steel," Materials Chemistry and Physics, 111(2–3), pp. 375-80.
[77] Watanabe, T., Takayama, H., and Yanagisawa, A., 2006, "Joining of aluminum alloy to steel by friction stir welding," Journal of Materials Processing Technology, 178(1-3), pp. 342-49.
[78] Jafarzadegan, M., Feng, A., Abdollah-zadeh, A., Saeid, T., Shen, J., and Assadi, H., 2012, "Microstructural characterization in dissimilar friction stir welding between 304 stainless steel and st37 steel," Materials Characterization.
[79] Barnes, S., Bhatti, A., Steuwer, A., Johnson, R., Altenkirch, J., and Withers, P., 2012, "Friction Stir Welding in HSLA-65 Steel: Part I. Influence of Weld Speed and Tool Material on Microstructural Development," Metallurgical and Materials Transactions A, 43(7), pp. 2342-55.
[80] Ohashi, R., Fujimoto, M., Mironov, S., Sato, Y., and Kokawa, H., 2009, "Effect of contamination on microstructure in friction stir spot welded DP590 steel," Science and Technology of Welding & Joining, 14(3), pp. 221-27.

[81] Park, S. H. C., Sato, Y. S., Kokawa, H., Okamoto, K., Hirano, S., and Inagaki, M., 2009, "Boride formation induced by PCBN tool wear in friction-stir-welded stainless steels," Metallurgical and Materials Transactions A, 40(3), pp. 625-36.
[82] Trimble, D., Monaghan, J., and O'Donnell, G., 2012, "Force generation during friction stir welding of AA2024-T3," CIRP Annals-Manufacturing Technology, 61(1), pp. 9-12.
[83] Soundararajan, V., Zekovic, S., and Kovacevic, R., 2005, "Thermo-mechanical model with adaptive boundary conditions for friction stir welding of Al 6061," International Journal of Machine Tools and Manufacture, 45(14), pp. 1577-87.
[84] Park, K., 2009, Development and Analysis of Ultrasonic Assisted Friction Stir Welding Process, University of Michigan, PhD dissertation.
[85] Leitão, C., Louro, R., and Rodrigues, D., 2012, "Using torque sensitivity analysis in accessing Friction Stir Welding/Processing conditions," Journal of Materials Processing Technology, 212(10), pp. 2051-57.
[86] Guerra, M., Schmidt, C., McClure, J. C., Murr, L. E., and Nunes, A. C., 2002, "Flow patterns during friction stir welding," Materials Characterization, 49(2), pp. 95-101.
[87] Colligan, K., 1999, "Material flow behavior during friction welding of aluminum," Welding journal, 75(7), pp. 229s-37s.
[88] Reynolds, A. P., 2000, "Visualisation of material flow in autogenous friction stir welds," Science and Technology of Welding & Joining, 5(2), pp. 120-24.
[89] Coelho, R. S., Kostka, A., dos Santos, J., and Pyzalla, A. R., 2008, "EBSD Technique Visualization of Material Flow in Aluminum to Steel Friction Stir Dissimilar Welding," Advanced Engineering Materials, 10(12), pp. 1127-33.
[90] Reynolds, A. P., 2008, "Flow visualization and simulation in FSW," Scripta Materialia, 58(5), pp. 338-42.
[91] Bouché, K., Barbier, F., and Coulet, A., 1998, "Intermetallic compound layer growth between solid iron and molten aluminium," Materials Science and Engineering: A, 249(1–2), pp. 167-75.
[92] Rathod, M. J., 2004, "Joining of aluminum alloy 5052 and low-carbon steel by laser roll welding," Welding journal, 83(1), p. 16.
[93] Kobayashi, S., and Yakou, T., 2002, "Control of intermetallic compound layers at interface between steel and aluminum by diffusion-treatment," Materials Science and Engineering: A, 338(1), pp. 44-53.
[94] Bouayad, A., Gerometta, C., Belkebir, A., and Ambari, A., 2003, "Kinetic interactions between solid iron and molten aluminium," Materials Science and Engineering: A, 363(1–2), pp. 53-61.
[95] Yeremenko, V., Natanzon, Y. V., and Dybkov, V. I., 1981, "The effect of dissolution on the growth of the Fe2Al5 interlayer in the solid iron-liquid aluminium system," Journal of Materials Science, 16(7), pp. 1748-56.
[96] Shahverdi, H. R., Ghomashchi, M. R., Shabestari, S., and Hejazi, J., 2002, "Microstructural analysis of interfacial reaction between molten aluminium and solid iron," Journal of Materials Processing Technology, 124(3), pp. 345-52.
[97] Sundman, B., Ohnuma, I., Dupin, N., Kattner, U. R., and Fries, S. G., 2009, "An assessment of the entire Al–Fe system including D03 ordering," Acta Materialia, 57(10), pp. 2896-908.
[98] Rathod, M., and Kutsuna, M., 2004, "Joining of aluminum alloy 5052 and low-carbon steel by laser roll welding," WELDING JOURNAL-NEW YORK-, 83(1), p. 16.
[99] Tylecote, R. F., 1968, The solid phase welding of metals, Edward Arnold.
[100] Khandkar, M. Z. H., Khan, J. A., and Reynolds, A. P., 2003, "Prediction of temperature distribution and thermal history during friction stir welding: input torque based model," Science and Technology of Welding and Joining, 8(3), pp. 165-74.
[101] Chao, Y. J., and Qi, X., 1998, "Thermal and thermo-mechanical modeling of friction stir welding of aluminum alloy 6061-T6," Journal of materials processing manufacturing science, 7(2), pp. 215-33.
[102] Chao, Y. J., Qi, X., and Tang, W., 2003, "Heat transfer in friction stir welding-experimental and numerical studies," Transactions ASME Journal of Manufacturing Science and Engineering, 125(1), pp. 138-45.

[103] Zhu, X., and Chao, Y., 2004, "Numerical simulation of transient temperature and residual stresses in friction stir welding of 304L stainless steel," Journal of Materials Processing Technology, 146(2), pp. 263-72.
[104] Hamilton, C., Dymek, S., and Blicharski, M., 2008, "A model of material flow during friction stir welding," Materials Characterization, 59(9), pp. 1206-14.
[105] Khandkar, M., Khan, J. A., and Reynolds, A. P., 2003, "Prediction of temperature distribution and thermal history during friction stir welding: input torque based model," Science and Technology of Welding & Joining, 8(3), pp. 165-74.
[106] De Vuyst, T., D'Alvise, L., Simar, A., De Meester, B., and Pierret, S., 2005, "Finite Element Modelling of Friction Stir Welding of Aluminium Alloy Plates-Inverse Analysis using a Genetic Algorithm," Welding in the World, 49(3-4), pp. 47-55.
[107] Simar, A., Lecomte-Beckers, J., Pardoen, T., and De Meester, B., 2006, "Effect of boundary conditions and heat source distribution on temperature distribution in friction stir welding," Science and Technology of Welding and Joining, 11(2), pp. 170-77.
[108] Song, M., and Kovacevic, R., 2003, "Thermal modeling of friction stir welding in a moving coordinate system and its validation," International Journal of Machine Tools and Manufacture, 43(6), pp. 605-15.
[109] Zhang, H., Zhang, Z., and Chen, J., 2005, "The finite element simulation of the friction stir welding process," Materials Science and Engineering: A, 403(1), pp. 340-48.
[110] Kuykendall, K., Nelson, T., and Sorensen, C., 2013, "On the selection of constitutive laws used in modeling friction stir welding," International Journal of Machine Tools and Manufacture, 74, pp. 74-85.
[111] Assidi, M., Fourment, L., Guerdoux, S., and Nelson, T., 2010, "Friction model for friction stir welding process simulation: Calibrations from welding experiments," International Journal of Machine Tools and Manufacture, 50(2), pp. 143-55.
[112] Liechty, B., and Webb, B., 2008, "Modeling the frictional boundary condition in friction stir welding," International Journal of Machine Tools and Manufacture, 48(12), pp. 1474-85.
[113] Yu, M., Li, W., Li, J., and Chao, Y., 2012, "Modelling of entire friction stir welding process by explicit finite element method," Materials Science and Technology, 28(7), pp. 812-17.
[114] Mandal, S., Rice, J., and Elmustafa, A., 2008, "Experimental and numerical investigation of the plunge stage in friction stir welding," Journal of Materials Processing Technology, 203(1), pp. 411-19.
[115] Schmidt, H., and Hattel, J., 2005, "A local model for the thermomechanical conditions in friction stir welding," Modelling and Simulation in Materials Science and Engineering, 13, p. 77.
[116] Hossfeld, M., and Roos, E., 2013, "A new approach to modelling friction stir welding using the CEL method," Advanced Manufacturing Engineering and Technologies NEWTECH 2013 Stockholm, Sweden 27-30 October 2013, p. 179.
[117] Guerdoux, S., and Fourment, L., 2009, "A 3D numerical simulation of different phases of friction stir welding," Modelling and Simulation in Materials Science and Engineering, 17(7), p. 075001.
[118] Ulysse, P., 2002, "Three-dimensional modeling of the friction stir-welding process," International Journal of Machine Tools and Manufacture, 42(14), pp. 1549-57.
[119] Colegrove, P., and Shercliff, H., 2004, "Development of Trivex friction stir welding tool Part 2 : three-dimensional flow modelling," Science and Technology of Welding and Joining, 9(4), pp. 352-61.
[120] Nandan, R., Roy, G., Lienert, T., and Debroy, T., 2007, "Three-dimensional heat and material flow during friction stir welding of mild steel," Acta Materialia, 55(3), pp. 883-95.
[121] Nandan, R., Debroy, T., and Bhadeshia, H., 2008, "Recent advances in friction-stir welding – Process, weldment structure and properties," Progress in Materials Science, 53(6), pp. 980-1023.
[122] Arora, A., Nandan, R., Reynolds, A., and DebRoy, T., 2009, "Torque, power requirement and stir zone geometry in friction stir welding through modeling and experiments," Scripta Materialia, 60(1), pp. 13-16.
[123] Nandan, R., Roy, G., and Debroy, T., 2006, "Numerical simulation of three-dimensional heat transfer and plastic flow during friction stir welding," Metallurgical and Materials Transactions A, 37(4), pp. 1247-59.

[124] Nandan, R., Roy, G., Lienert, T., and DebRoy, T., 2006, "Numerical modelling of 3D plastic flow and heat transfer during friction stir welding of stainless steel," Science and Technology of Welding & Joining, 11(5), pp. 526-37.
[125] Chen, G., Shi, Q., and Feng, Z., 2015, "On the Material Behavior at Tool/Workpiece Interface During Friction Stir Welding: A CFD Based Numerical Study," Friction Stir Welding and Processing VIII, pp. 251-58.
[126] Chen, G. Q., Shi, Q. Y., Fujiya, Y., and Horie, T., 2014, "Simulation of Metal Flow During Friction Stir Welding Based on the Model of Interactive Force Between Tool and Material," Journal of Materials Engineering and Performance, 23(4), pp. 1321-28.
[127] Wang, H., Colegrove, P. A., and dos Santos, J. F., 2013, "Numerical investigation of the tool contact condition during friction stir welding of aerospace aluminium alloy," Computational Materials Science, 71, pp. 101-08.
[128] Buffa, G., Hua, J., Shivpuri, R., and Fratini, L., 2006, "A continuum based fem model for friction stir welding—model development," Materials Science and Engineering: A, 419(1), pp. 389-96.
[129] Al-Badour, F., Merah, N., Shuaib, A., and Bazoune, A., 2014, "Thermo-mechanical finite element model of friction stir welding of dissimilar alloys," The International Journal of Advanced Manufacturing Technology, 72(5-8), pp. 607-17.
[130] Li, K., Aidun, D., and Marzocca, P., 2009, Time-varying Functionally Graded Material thermal modeling of friction stir welding joint of dissimilar metals, ASM International, pp. 731-35.
[131] Torres, E., "CFD Modelling of Dissimilar Aluminum-Steel Friction Stir Welds," Proc. 9th International Conference on Trends in Welding Research, Asm.
[132] Ishii, M., 1975, "Thermo-fluid dynamic theory of two-phase flow," NASA STI/Recon Technical Report A, 75, p. 29657.
[133] Ishii, M., Hibiki, T., and SpringerLink, 2006, Thermo-fluid dynamics of two-phase flow, Springer Science+Business Media, New York, N.Y.
[134] Stone, H., 1990, "A simple derivation of the time‐dependent convective‐diffusion equation for surfactant transport along a deforming interface," Physics of Fluids A: Fluid Dynamics (1989-1993), 2(1), pp. 111-12.
[135] Aris, R., 1990, Vectors, tensors and the basic equations of fluid mechanics, Courier Dover Publications.
[136] Scriven, L. E., 1960, "Dynamics of a fluid interface Equation of motion for Newtonian surface fluids," Chemical Engineering Science, 12(2), pp. 98-108.
[137] Liu, X., Lan, S., and Ni, J., 2014, "Analysis of process parameters effects on friction stir welding of dissimilar aluminum alloy to advanced high strength steel," Materials & Design, 59, pp. 50-62.
[138] Girifalco, L., and Good, R., 1957, "A theory for the estimation of surface and interfacial energies. I. Derivation and application to interfacial tension," The Journal of Physical Chemistry, 61(7), pp. 904-09.
[139] Bainbridge, I., and Taylor, J., 2013, "The Surface Tension of Pure Aluminum and Aluminum Alloys," Metallurgical and Materials Transactions A, 44(8), pp. 3901-09.
[140] Su, Y., Li, Z., and Mills, K. C., 2005, "Equation to estimate the surface tensions of stainless steels," Journal of Materials Science, 40(9-10), pp. 2201-05.
[141] Frigaard, Ø., Grong, Ø., and Midling, O., 2001, "A process model for friction stir welding of age hardening aluminum alloys," Metallurgical and Materials Transactions A, 32(5), pp. 1189-200.
[142] Adibi-Sedeh, A. H., Madhavan, V., and Bahr, B., 2003, "Extension of Oxley's analysis of machining to use different material models," Journal of manufacturing science and engineering, 125, p. 656.
[143] Van Slycken, J., Verleysen, P., Degrieck, J., Samek, L., and De Cooman, B., 2006, "High-strain-rate behavior of low-alloy multiphase aluminum-and silicon-based transformation-induced plasticity steels," Metallurgical and Materials Transactions A, 37(5), pp. 1527-39.
[144] Li, Z., Mukai, K., Zeze, M., and Mills, K., 2005, "Determination of the surface tension of liquid stainless steel," Journal of Materials Science, 40(9-10), pp. 2191-95.
[145] Sarou-Kanian, V., Millot, F., and Rifflet, J. C., 2003, "Surface Tension and Density of Oxygen-Free Liquid Aluminum at High Temperature," International Journal of Thermophysics, 24(1), pp. 277-86.

[146] Anson, J., Drew, R., and Gruzleski, J., 1999, "The surface tension of molten aluminum and Al-Si-Mg alloy under vacuum and hydrogen atmospheres," Metallurgical and Materials Transactions B, 30(6), pp. 1027-32.
[147] Reference manual, FLUENT 15.0.
[148] Sheppard, T., and Wright, D., 1979, "Determination of flow stress: Part 1 constitutive equation for aluminium alloys at elevated temperatures," Metals Technology, 6(1), pp. 215-23.
[149] Dirikolu, M., Childs, T., and Maekawa, K., 2001, "Finite element simulation of chip flow in metal machining," International journal of mechanical sciences, 43(11), pp. 2699-713.
[150] Childs, T., 2000, Metal machining: theory and applications (Chapter 2.1), Butterworth-Heinemann.
[151] Khamei, A., and Dehghani, K., 2015, "Effects of strain rate and temperature on hot tensile deformation of severe plastic deformed 6061 aluminum alloy," Materials Science and Engineering: A, 627, pp. 1-9.
[152] Li, D., Feng, Y., Yin, Z., Shangguan, F., Wang, K., Liu, Q., and Hu, F., 2012, "Hot deformation behavior of an austenitic Fe–20Mn–3Si–3Al transformation induced plasticity steel," Materials & Design, 34, pp. 713-18.
[153] Maekawa, K., Kubo, A., and Childs, T., "A friction model for free-machining steels and its applicability to machinability analysis," Proc. Key Engineering Materials, Trans Tech Publ, pp. 79-90.
[154] Palm, F., 2004, Laser supported friction stir welding method, Google Patents.
[155] Sun, Y., and Fujii, H., 2010, "Recent Patented Hybrid Techniques for Friction Stir Welding of Metallic Materials," Recent Patents on Mechanical Engineering, 3(3), pp. 206-10.
[156] Merklein, M., and Giera, A., 2008, "Laser assisted Friction Stir Welding of drawable steel-aluminium tailored hybrids," International Journal of Material Forming, 1(1), pp. 1299-302.
[157] Cao, G., and Kou, S., 2006, Arc-enhanced friction stir welding, Google Patents.
[158] Bang, H., Bang, H., Jeon, G., Oh, I., and Ro, C., 2012, "Gas tungsten arc welding assisted hybrid friction stir welding of dissimilar materials Al6061-T6 aluminum alloy and STS304 stainless steel," Materials & Design, 37, pp. 48-55.
[159] Grant, G., Khaleel, M., Eberhardt, J., Arbegast, B., Stone, G., Howard, S., and Allen, C., 2005, "Friction stir joining and processing of advanced materials including MMCs," High Strength Weight Reduction Materials, pp. 112-21.
[160] Santos, T. G., Miranda, R., and Vilaça, P., 2014, "Friction Stir Welding assisted by electrical Joule effect," Journal of Materials Processing Technology.
[161] Ferrando, W. A., 2008, "The concept of Electrically Assisted Friction Stir Welding (EAFSW) and application to the processing of various metals," DTIC Document.
[162] Luo, J., Chen, W., and Fu, G., 2014, "Hybrid-heat effects on electrical-current aided friction stir welding of steel, and Al and Mg alloys," Journal of Materials Processing Technology.
[163] Pitschman, M., Dolecki, J. W., Johns, G. W., Zhou, J., and Roth, J. T., "Application of Electric Current in Friction Stir Welding," ASME.
[164] Potluri, H., Jones, J. J., and Mears, L., "Comparison of Electrically-Assisted and Conventional Friction Stir Welding Processes by Feed Force and Torque," Proc. ASME 2013 International Manufacturing Science and Engineering Conference collocated with the 41st North American Manufacturing Research Conference, American Society of Mechanical Engineers, pp. V001T01A55-V01T01A55.
[165] Conrad, H., Guo, Z., and Sprecher, A., 1989, "Effect of an electric field on the recovery and recrystallization of al and Cu," Scr. Metall., 23(6), pp. 821-24.
[166] Xiong, J. T., Li, J. L., Qian, J. W., Zhang, F. S., and Huang, W. D., 2012, "High strength lap joint of aluminium and stainless steels fabricated by friction stir welding with cutting pin," Science and Technology of Welding and Joining, 17(3), pp. 196-201.
[167] Chen, S. W., Chen, C. M., and Liu, W. C., 1998, "Electric current effects upon the Sn/Cu and Sn/Ni interfacial reactions," Journal of Electronic Materials, 27(11), pp. 1193-99.
[168] Chen, S.-W., Chen, C.-M., and Liu, W.-C., 1998, "Electric current effects upon the Sn/Cu and Sn/Ni interfacial reactions," Journal of Electronic Materials, 27(11), pp. 1193-99.
[169] Nowick, A. S., 2012, Diffusion in solids: recent developments, Elsevier.

[170] Marcinkowski, M. J., and Smoluchowski, R., 1965, "Electrical resistivity of iron-aluminum superlattices near Fe3Al," Journal of Physics and Chemistry of Solids, 26(1), pp. 185-89.